Masterthesis with the topic

Dynamics of localized states in the complex cubic-quintic Ginzburg-Landau equation

Jana Wrembel (E-Mail: j_wrem01@wwu.de)

First evaluation: Priv.-Doz. Dr. Svetlana Gurevich
Second evaluation: Prof. Dr. Julien Javaloyes

June 2, 2022

Eigenständigkeitserklärung

Hiermit versichere ich, dass die vorliegende Arbeit über _____ _____ selbstständig von mir und ohne fremde Hilfe verfasst worden ist, dass keine anderen Quellen und Hilfsmittel als die angegebenen benutzt worden sind und dass die Stellen der Arbeit, die anderen Werken – auch elektronischen Medien – dem Wortlaut oder Sinn nach entnommen wurden, auf jeden Fall unter Angabe der Quelle als Entlehnung kenntlich gemacht worden sind. Mir ist bekannt, dass es sich bei einem Plagiat um eine Täuschung handelt, die gemäß der Prüfungsordnung sanktioniert werden kann.

Ich erkläre mich mit einem Abgleich der Arbeit mit anderen Texten zwecks Auffindung von Übereinstimmungen sowie mit einer zu diesem Zweck vorzunehmenden Speicherung der Arbeit in einer Datenbank einverstanden.

Ich versichere, dass ich die vorliegende Arbeit oder Teile daraus nicht anderweitig als Prüfungsarbeit eingereicht habe.

_____
(Datum, Unterschrift)

Contents

1 Introduction

The concept of a dissipative soliton has several areas of application within physics like in nonlinear optics [1], [2] or in plasma physics [3] but also in other fields for example biology and medicine [4]. The term soliton describes localized solutions of differential equations that maintain their shape and velocity after colliding with each other by balancing nonlinearity with dispersion effects [5]. In addition to that, dissipative solitons also balance the energy gain and loss so that they build a stationary fixed point [6].

Dissipative solitons also occur in the context of passive mode-locked lasers, which are used for the generation of self-shaped ultrashort laser pulses [7]. This is the main topic of this work. The master equation for its description is the complex cubic-quintic Ginzburg-Landau equation. Using this equation and a direct split-step Fourier approach it was possible to determine several different stable localized soliton solutions. The plain pulse is the easiest solution but there exist more complicated ones like the composite pulse which consists of a plain pulse and two fronts and an expanded structure that fills the whole domain length with a constant height [8]. There are moving, creeping, and snaking solitons that move through the domain (see [8],[7] and [9]), pulsating solitons have got a pulsating width (see [7]) and exploding solitons where their pulse structure gets destroyed and rebuild with time (see [7] and [10]). They have a lot of remarkable features like asymmetric explosions [11] or control by higher-order terms [12], [13] and also experimental evidence [14]. Another interesting topic is the soliton resonance phenomenon. Here, at a given parameter value the soliton energy rises exponentially while building a resonance, see for example [15], [16] or [17]. This is important because it enables the building of high-energy solitons [18].

One goal for this work is to summarize and further illuminate the connection between those various kinds of localized soliton solutions. This is done via bifurcation diagram analysis. In a bifurcation diagram, these different solution types are depicted as branches from bifurcation points. Those branches can be connected, as it is shown later on, for example for the pulsating soliton solution as it originates from an Andronov-Hopf bifurcation on the plain pulse branch. The analysis of these connections between different branches via bifurcation diagrams is a useful tool for the understanding of localized solutions of the complex cubic-quintic Ginzburg-Landau equation. The second main topic within this work is the soliton resonance phenomenon. Here again, a bifurcation diagram analysis is used to discuss and to get a new perspective on previously published results within the topic of soliton resonance.

The bifurcation diagram is made with the help of numerical continuation. This method can be used to find and follow solution branches and detect bifurcations. It is applied using pde2path, which is a Matlab package for bifurcation and continuation analysis of elliptic partial differential equations, see [19]. Mathematically speaking, it uses the finite element method to reiterate upon a given initial solution. This initial solution is approximated using direct numerical methods using a pseudo-spectral approach and the Runge-Kutta method. The continuation method can also be used to understand the impact of parameter changes different from the primary continuation parameter and attempt determine the region of existence of different solution types, using a technique called fold continuation. Here a saddle-node bifurcation point can be followed along in

phase space.
Using these methods it was possible to find a bifurcation diagram at which branches for the plain, composite, moving, creeping, and pulsating soliton as well as the continuous wave solution occur and are connected in some way. Also, the soliton resonance phenomenon was replicated and discussed using bifurcation diagrams.
First, the theory behind this work necessary for understanding will be explained. This includes the basic concepts of nonlinear physics. There the description of physics using ordinary or partial differential equations as well as the appearance of stationary solutions and the impact of their stability are highlighted. An explanation of what bifurcations are and which types can occur is given afterwards. The next section addresses dissipative solitons and their history of origin, the Ginzburg-Landau model, and its application onto passively mode-locked lasers. In addition, localized solutions of the complex cubic-quintic Ginzburg-Landau equation like pulsating or composite solitons and the soliton resonance phenomenon are depicted. Next, the methods required for the numerical investigation of the overall system, such as the numerical continuation, are explained. Here, the mathematical concepts of the direct and the continuation approach are discussed and it is shown how they are implemented for the model under study. Then the results of this work will be presented and explained starting with the dynamics of localized solutions and ending with a discussion of soliton resonance. Finally, the results are summarized and an outlook on further aspects is given.

2 Concepts of nonlinear physics

This section describes the basic concepts of nonlinear physics to give a general introduction to the methods used.

2.1 Ordinary and partial differential equations

A differential equation is an equation that describes a field, mathematically a function of variables, in which derivative of the field with respect to certain variables occur. An ordinary differential equation has the characteristic that derivatives occur just with respect to one variable. A known example is the one-dimensional Newtons equation of motion

$$F = m \cdot \ddot{x} \tag{1}$$

where F is the applied force, m the mass of the object under consideration, and $\ddot{x}$ the resulting acceleration [20]. If the force F is not dependent on time, the ordinary differential equation is called additionally autonomous. An example for this is the gravitational force $F_g = m \cdot g$ with acceleration due to gravity of $g \approx 9.81 \frac{\mathrm{m}}{\mathrm{s}^2}$ [20]. By solving the resulting differential equation

$$m \cdot g = m \cdot \ddot{r}, \tag{2}$$

the movement of an object can be determined when knowing the initial conditions. In general, a n-dimensional autonomous ordinary differential equation is given by

$$\frac{d\vec{x}}{d\vec{t}} = \vec{F}(\vec{x}, \mu) \tag{3}$$

where $\vec{x} = (x_1, x_2, \ldots, x_n)$ is a vector field and $\vec{F} = (F_1, F_2, \ldots, F_n)$ a n-dimensional vector [21]. The equation 3 in general describes an ordinary differential equation because every differential equation of order n can be reduced to an n-dimensional system of ordinary differential equations. μ is called the control parameter which influences the system but is not dependant on time t. Fixed points in the system are of particular interest. A fixed point $\vec{x}_\mathrm{f}$ is defined by

$$\vec{F}(\vec{x}_\mathrm{f}, \mu) = 0. \tag{4}$$

A fixed point has due to equation 3 no time dynamics and represents a singular point in phase space, spanned by the components x_i with $i \in \{1, 2, \ldots, n\}$ [21].
The difference between an ordinary and a partial differential equation is that in the latter partial derivates occur. Therefore the field depends on more than one variable, for example, time and space. An example of a partial differential equation is the one-dimensional Heat equation

$$\frac{\partial T(x,t)}{\partial t} = a \frac{\partial^2 T(x,t)}{\partial x^2} \tag{5}$$

[22] where T is the temperature and a the thermal diffusivity coefficient. This is a partial differential equation because partial derivatives with respect to space x and time t occur. With the equation, the propagation of heat can be viewed from a certain initial state.
For an ordinary differential equation, fixed points were of particular interest. An analogous to these is formed by the stationary solutions in partial differential equations. Here the partial time derivative vanishes.
In this work the complex cubic-quintic Ginzburg-Landau equation

$$\mathrm{i}\frac{\partial A}{\partial z} + \frac{D}{2}\frac{\partial^2 A}{\partial t^2} + |A|^2 A + \mu |A|^4 A = \mathrm{i}\delta A + \mathrm{i}\varepsilon |A|^2 A + \mathrm{i}\beta\frac{\partial^2 A}{\partial t^2} + \mathrm{i}\mu |A|^4 A.$$

will be discussed. This partial differential equation is the master equation to describe a system of passively mode-locked lasers.

2.2 Stationary solutions and their stability

If a stationary solution of a partial differential equation is known, the stability of this solution is a physically interesting question. What happens if a small perturbation is added to the system? Is the solution stable or unstable under that perturbation?
A simple example that illustrates this topic is the damped pendulum. This pendulum has two fixed points shown in the following figure 1.

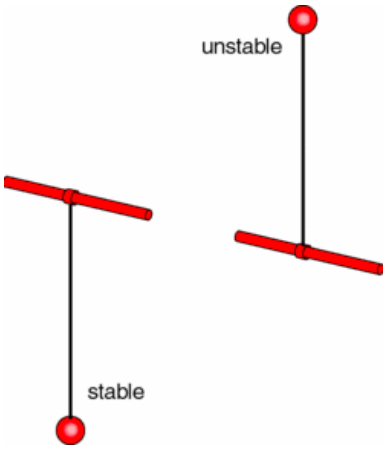

Figure 1: Equilibrium positions of pendulum. On the left-hand side is the stable solution $x_1 = (0,0)$ and on the right-hand side the unstable one $x_2 = (\pi,0)$. The coordinates used represent the angle φ and the angular velocity ω, specified as a tuple (φ,ω). [23]

The two equilibrium positions x_1 and x_2 shown in the figure 1 are in mechanical equilibrium since the mass of the pendulum does not experience any acceleration. Mathematically, the damped pendulum is given by the system of differential equations

$$\begin{aligned} \dot{\omega} + \gamma\omega + \frac{g}{l}\sin(\varphi) &= 0 \\ \dot{\varphi} &= \omega \end{aligned} \tag{6}$$

[21]. To derive a fixed point, equation 4 must be applied:

$$F(x_\mathrm{f}) = 0 \qquad \Rightarrow \qquad -\frac{g}{l}\sin(\varphi) \stackrel{!}{=} 0. \tag{7}$$

Using the definition of the sinus, both fixed points $x_1 = (0,0)$ and $x_2 = (\pi,0)$ follow directly. Both fixed points can be explained by the fact that the gravitational force applied to the mass of the pendulum acts downwards in figure 1 and since the length of the rod is constant, no movement of the pendulum is triggered. This example shows the importance of the stability of the equilibrium positions because the unstable solution x_2 would change over to the stable position x_1 via oscillations if a small disturbance is applied. The stability of a solution is therefore important for the physical application.
To calculate the stability of a solution mathematically, different concepts can be applied but the mainly used concept is the concept of linear stability. There a small perturbation $\delta\vec{x}(t)$ is applied to the fixed point $\vec{x}_\mathrm{f}$

$$\vec{x} = \vec{x}_\mathrm{f} + \delta\vec{x}. \tag{8}$$

This ansatz is put into the ordinary differential equation (see equation 3) that should be analyzed and then linearized for small perturbations

$$\frac{\mathrm{d}\vec{x}_\mathrm{f}}{\mathrm{d}t} + \frac{\mathrm{d}\delta\vec{x}}{\mathrm{d}t} = \vec{F}(\vec{x}_\mathrm{f},\mu) + \frac{\mathrm{d}\vec{F}(\vec{x}_\mathrm{f},\mu)}{\mathrm{d}\vec{x}} \cdot \delta\vec{x} + O(|\delta\vec{x}|^2), \tag{9}$$

where $\frac{\mathrm{d}\vec{x}_\mathrm{f}}{\mathrm{d}t} = \vec{F}(\vec{x}_\mathrm{f},\mu) = 0$ is true because $\vec{x}_\mathrm{f}$ is a fixed point. If one neglects the nonlinear terms in δx it results in

$$\frac{\mathrm{d}\delta\vec{x}}{\mathrm{d}t} = \frac{\mathrm{d}\vec{F}(\vec{x}_\mathrm{f},\mu)}{\mathrm{d}\vec{x}} \cdot \delta x. \tag{10}$$

Hereby $\frac{\mathrm{d}\vec{F}(\vec{x}_\mathrm{f},\mu)}{\mathrm{d}\vec{x}}$ is the Jacobian:

$$\frac{\mathrm{d}\vec{F}(\vec{x}_\mathrm{f},\mu)}{\mathrm{d}\vec{x}} = \begin{pmatrix} \frac{\partial F_1}{\partial x_1} & \frac{\partial F_1}{\partial x_2} & \cdots & \frac{\partial F_1}{\partial x_n} \\ \frac{\partial F_2}{\partial x_1} & \ddots & & \vdots \\ \vdots & & \ddots & \vdots \\ \frac{\partial F_n}{\partial x_1} & \cdots & \cdots & \frac{\partial F_n}{\partial x_n} \end{pmatrix}_{(\vec{x}=\vec{x}_\mathrm{f})} . \tag{11}$$

At this point the following ansatz

$$\delta\vec{x}(t) = \vec{u} \cdot e^{\lambda t} \tag{12}$$

is used. Inserting this into equation 10 it results in an eigenvalue equation

$$\frac{\mathrm{d}\vec{F}(\vec{x}_\mathrm{f},\mu)}{\mathrm{d}\vec{x}} \cdot \vec{u} \cdot e^{\lambda t} = \lambda \cdot \vec{u} \cdot e^{\lambda t} \tag{13}$$

with the help of which the eigenvalues λ_i and the associated eigenfunctions $\vec{u}_i$ can be determined for the to be examined fixed point. At this point, one can see that in the one-dimensional case only the sign of λ decides the stability of the fixed point under perturbation (see equation 12). Due to equation 8, follows

$$x = x_\mathrm{f} + u \cdot e^{\lambda t}. \tag{14}$$

If $\lambda < 0$, than the perturbation δx subsides over time up to $x = x_\mathrm{f}$ so that the fixed point is stable under small disturbances. For $\lambda > 0$ the perturbation δx increases over time and the fixed point is unstable regarding perturbations. In the case, $\lambda = 0$ the system is marginally stable, which means that the nonlinear terms neglected in equation 9 determine the stability of the system. If λ has an imaginary part, it generates an oscillation and is therefore irrelevant for the stability of the solution.
In the more dimensional case, eigenvalues $\lambda_1, \lambda_2, \ldots, \lambda_n$ exists that influence the stability. The general solution is a linear combination of those eigenmodes

$$\delta\vec{x} = \sum_{i=1}^{n} c_i \cdot \vec{u}_i \cdot e^{\lambda_i t}, \tag{15}$$

which means that the fixed point is stable if all eigenfunctions $\vec{u}_i$ are stable.
Using this linear stability analysis one can calculate the stability of the solution of the damped pendulum example. In the one-dimensional case of the linear stability analysis, it follows

$$\lambda = \frac{\mathrm{d}F(x_\mathrm{f})}{\mathrm{d}x} \overset{\text{Gl. (6)}}{=} -\frac{g}{l}\cos(\theta) \tag{16}$$

If now the fixed points x_1 and x_2 are put into the equation, it yields for x_1 that $\lambda = -\frac{g}{l} < 0$ there it is a stable fixed point and for x_2 follows $\lambda = +\frac{g}{l} > 0$ and therefore it is unstable, as depicted in figure 1.

2.3 Bifurcations

With the help of the theory described above, it is possible to calculate fixed points (stationary solutions) of an ordinary (partial) differential equation including their stability. Now, it is possible that if a parameter is changed in such a way that it results in a change of stability of the solution or it causes a new solution to arise. Such a change of the solution is called bifurcation and the parameter value at which it occurs is called bifurcation point (see [21]).
Bifurcations are typically shown in a bifurcation diagram. Here the varied parameter is shown compared to a solution norm. For a partial differential equation, it is common to use a L_p-norm. Which norm is used depends on how the results can be presented clearly. In some systems, it could be useful to take the total energy of the system or the propagation speed. In a bifurcation diagram, stable solutions are marked with a solid line, whereas unstable solutions are shown with dashed lines. There are different types of bifurcations to characterize the appearing bifurcation.

The common local bifurcation types are called Pitchfork-, Saddle-Node, Andronov-Hopf, and transcritical bifurcation.
The transcritical bifurcation is characterized by the fact that it exchanges the stability of two known solutions. This bifurcation is shown in figure 2.

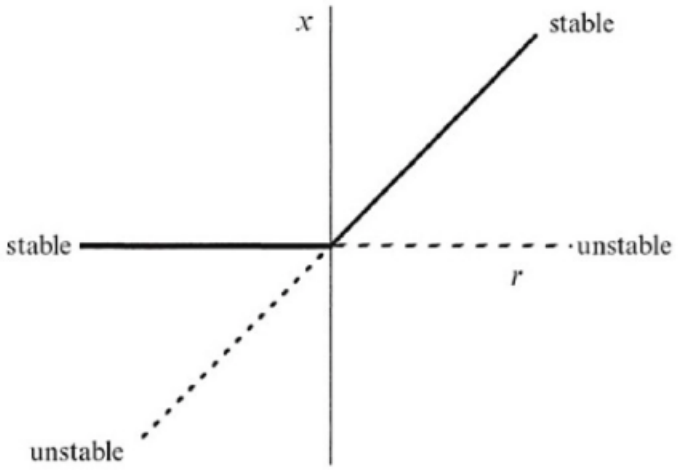

Figure 2: Basic form of a transcritical bifurcation. [21]

Every bifurcation type has a normal form. A normal form is a simplified mathematical equation that describes the behaviour of the equation. It is easy to understand the physical behaviour looking at that equation and equations in this form show the same behaviour. The normal form of a transcritical bifurcation is

$$\frac{\mathrm{d}x}{\mathrm{d}t} = rx - x^2. \tag{17}$$

Next up is the characteristic of a saddle-node bifurcation. There is a known solution that changes its stability, which is shown in the following figure 3.

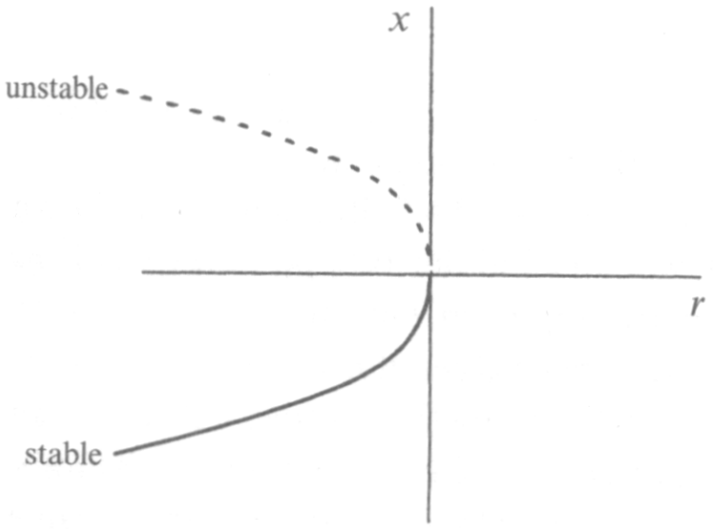

Figure 3: Basic form of the saddle-node bifurcation. [21]

The bifurcation point for the saddle-node bifurcations is also called fold point because of the fold-like shape of this type of bifurcation. This notation will be used in this work. Its normal form is given by

$$\frac{\mathrm{d}x}{\mathrm{d}t} = r + x^2. \tag{18}$$

At a pitchfork bifurcation point, two new solutions with the same stability arise and the old solution changes its stability. Due to the symmetrical shape of the new solutions, this bifurcation looks like a pitchfork, hence the name. Here a distinction between subcritical and supercritical pitchfork bifurcation is common. They differ in an exchange of signs in the considered equation. In the following figure 4, the two different types of pitchfork bifurcation are depicted.

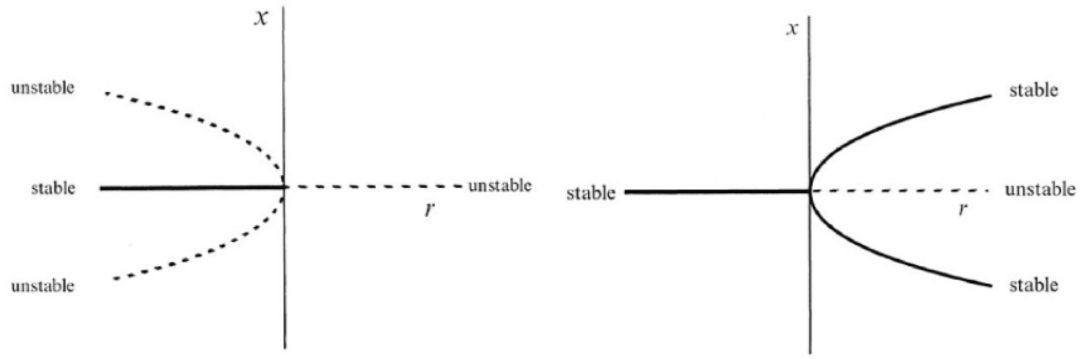

Figure 4: Both types of a pitchfork bifurcation. On the left-hand side is the subcritical bifurcation and on the right-hand side the supercritical one. [21]

The normal form of a pitchfork bifurcation is given by

$$\frac{\mathrm{d}x}{\mathrm{d}t} = rx \pm x^3 \tag{19}$$

where the ± sign corresponds for plus to the subcritical case and for minus to the supercritical one. The distinction between subcritical and supercritical is not unique to the pitchfork bifurcation. It also occurs for the earlier discussed transcritical and saddle-node bifurcation. The key difference is that in that case both are not equivalent when using symmetry operation but they are topologically equivalent. The last part is not true for the pitchfork bifurcation, hence the distinction in this case.

For the Andronov-Hopf bifurcation or short hopf bifurcation, a pair of complex conjugated eigenvalues crosses the imaginary axis as shown in figure 5.

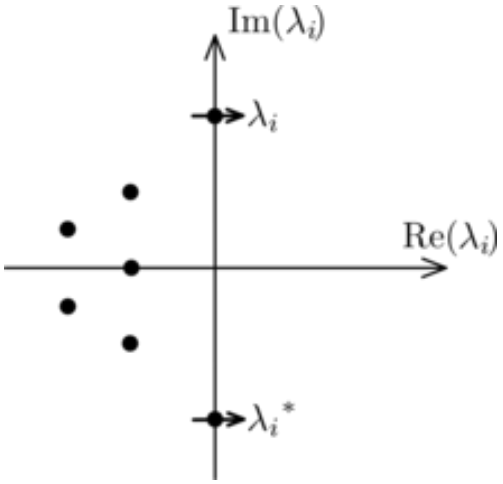

Figure 5: Sketch of the complex conjugated eigenvalues changing sign in the case of a hopf bifurcation. [24]

In contrast to the other bifurcations where real eigenvalues change sign here the imaginary part does it which ensures a temporally periodic behaviour of the solutions. Therefore there are stable and unstable fixed points and limit cycle solutions.

3 Localized solutions and soliton resonance in cubic-quintic Ginzburg-Landau equation

In this section, the theoretical basics are presented to get a better overview of the topic of mode-locked laser and to understand the connection to the complex cubic-quintic Ginzburg-Landau equation and soliton solutions. Aside from that existing numerical results of localized solutions like the composite pulse or pulsating solitons and the phenomenon of dissipative soliton resonance will be summarized.

3.1 Dissipative Solitons

„Soliton“ is a term, which is used to describe localized solutions of differential equations. Their characteristic is to maintain their shape and velocity after colliding with each other [5]. Originally the term was invented to describe nonlinear solitary wave solutions of integrable equations like the nonlinear Schrödinger equation [25]. Then it was found, that solitary waves also exist in non-integrable systems, so the term „dissipative soliton“ arose. It started with nonlinear optical systems with nonlinear gain or loss mechanisms like in [26] and [27]. That gave an interesting new aspect into the stability of optical solitons. For conservative solitons, the nonlinearity of the material works against the diffraction in spatial systems or against the dispersion in temporal systems [25]. In addition to that, for dissipative solitons, another counterplay of energy loss and gain could be added. It needs some energy input to remain intact while giving a certain energy output. This dynamic is shown in the following picture in figure 6

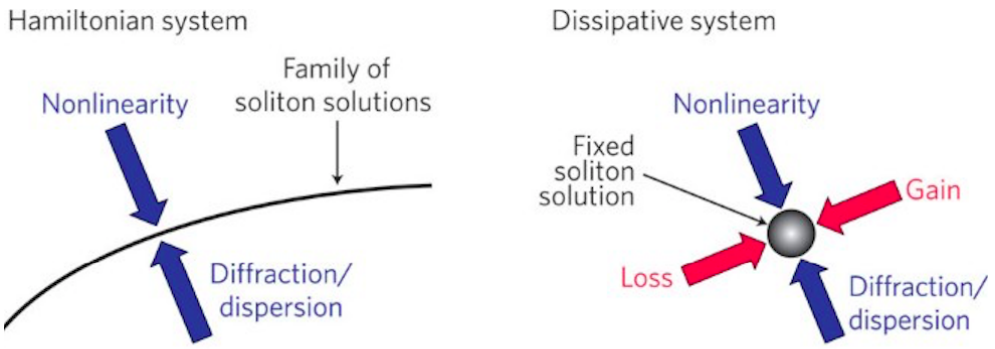

Figure 6: Balancing effects needed for solitons solutions in a conservative and dissipative systems. [5]

On the left side of figure 6 the conventional solitons can exist because of a balance between the nonlinear effects of the system or the underlying material and the diffraction or dissipation. In such a system it leads to an infinite number of solutions, a family of solutions, for one set of parameters [5]. In a dissipative system, as shown on the right side of figure 6, only one (localized) fixed point occurs. This is due to the additional balance between energy gain and loss. Here the shape of the soliton is not given by initial conditions, but by the system parameters. When

changing the system parameters it is also possible to witness bifurcations. For example, the existence of pulsating solitons, which form a limit cycle [7]. In this context, it was also shown that there is a periodic doubling behaviour leading to chaos.

3.2 Complex cubic-quintic Ginzburg-Landau equation

As seen in the last section, the concept of solitons occurs in a wide range of applications not only in nonlinear optics but also in other fields for example in plasma physics [3] or in biology and medicine [4]. Dissipative solitons also occur in the context of passive mode-locked lasers, which are used for the generation of self-shaped ultrashort laser pulses [7]. The resulting nonlinear dynamics are discussed in this work.

The basis for numerical analyses is a mathematical model describing the system of passively mode-locked lasers. There are many models describing laser systems with varying complexity because they take different components into account. The first models made to describe mode-locking were similar to the complex cubic Ginzburg-Landau equation, see [28] and [29]. Afterwards, a quintic term was included to assure the stability of the solitons [5]. The basic idea behind that concept will be explained using figure 7

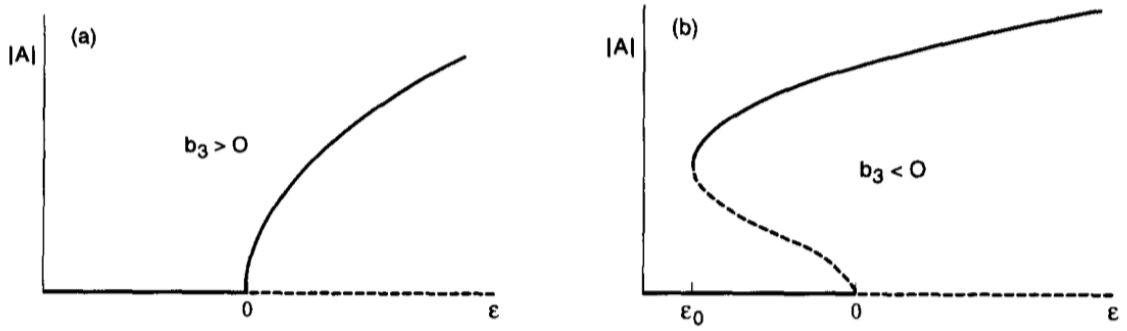

(a) cubic (b) cubic-quinitc

Figure 7: Example bifurcation diagrams described in [30] in respect to the there defined Ginzburg-Landau equation in the form $\partial_t A = \varepsilon A + (b_1 + \mathrm{i}c_1)\partial_x^2 A + (b_3 + \mathrm{i}c_3)\,|A|^2\,A + (b_5 + \mathrm{i}c_5)\,|A|^4\,A$. a) supercritical bifurcation at $\varepsilon = 0$ for $b_3 > 0$ and $b_5 = c_5 = 0$, corresponding to a complex cubic Ginzuburg-Landau equation. b) subcritical bifurcation for $b_3 < 0$ and $b_5 > 0$ for stability, corresponding to a complex cubic quinitc Ginzburg-Landau equation.

In the left figure 7a a typical bifurcation diagram for the only cubic equation is shown. It consists of a rather simple supercritical pitchfork, which is reasonable because of the mathematical structure similar to its normal form. The point is that this behaviour is not expected for the solitons, but a stabilized subcritical bifurcation due to quintic terms is. This is shown in figure 7b. The soliton solution emerging from the bifurcation point is unstable until a saddle-node bifurcation corresponding to the quintic term $b_5 > 0$ (following the nomenclature in [30]) occurs. For this parameter regime, there are stable soliton solutions for $\varepsilon < 0$ or energy loss, which is an expected result (see for example figure 20). For positive ε no soliton solutions are expected because the

global solution is unstable. Therefore a quintic term is needed for the description of passive mode-locked lasers.

The complex cubic-quintic Ginzburg-Landau equation is normally given in the following form:

$$\mathrm{i}\frac{\partial A}{\partial z} + \frac{D}{2}\frac{\partial^2 A}{\partial t^2} + |A|^2 A + \mu |A|^4 A = \mathrm{i}\delta A + \mathrm{i}\varepsilon |A|^2 A + \mathrm{i}\beta\frac{\partial^2 A}{\partial t^2} + \mathrm{i}\mu |A|^4 A. \tag{20}$$

From that form one can see, that it is an extension of the nonlinear Schrödinger equation for higher-order (cubic-quintic) and dissipative terms [5]. The left-hand side contains conservative terms, while the right-hand side contains the dissipative ones. Equation 20 is non-integrable so in general analytical solutions are not known. Just special cases are calculable so that a numerical analysis of the equation is useful.

In equation 20 the function A describes the normalized optical field envelope. It is a function of z the normalized propagation distance and t the retarded time. The parameter D is called group velocity dispersion coefficient, corresponding if positive to an anomalous and if negative to a normal regime. δ is the linear gain ($\delta > 0$ or loss ($\delta < 0$) coefficient, while ε is the nonlinear one. $\beta > 0$ includes spectral filtering and $\mu < 0$ gives the saturation of the nonlinear gain, while ν represents the saturation of the nonlinear refractive index. All in all, every coefficient can be related to physical parameters, see [31], [32] and [33].

To discuss the equation 20 in a more detailed way, it is useful to rearrange it so that the derivative with respect to z stands alone on the left-hand side. By bringing the conservative terms onto the right-hand side and multiplying by the imaginary unit i, the equation becomes

$$\frac{\partial A}{\partial z} = \left(\beta + \frac{D}{2}\mathrm{i}\right)\frac{\partial^2 A}{\partial t^2} + \delta A + (\varepsilon + \mathrm{i})|A|^2 A + (\mu + \nu\mathrm{i})|A|^4 A. \tag{21}$$

This is the standard form of a partial differential equation and is useful for mathematical and numerical analysis in different forms. Normally the derivatives on the left-hand side correspond to a time derivative so that the change with time can be better understood. Even if it does not look like it at first glance, this principle also applies here. Formally both z and t can be understood as time parameters in this case. To explain this idea and to get a better understanding of the physical meaning of the parameters, look at the following figure 8.

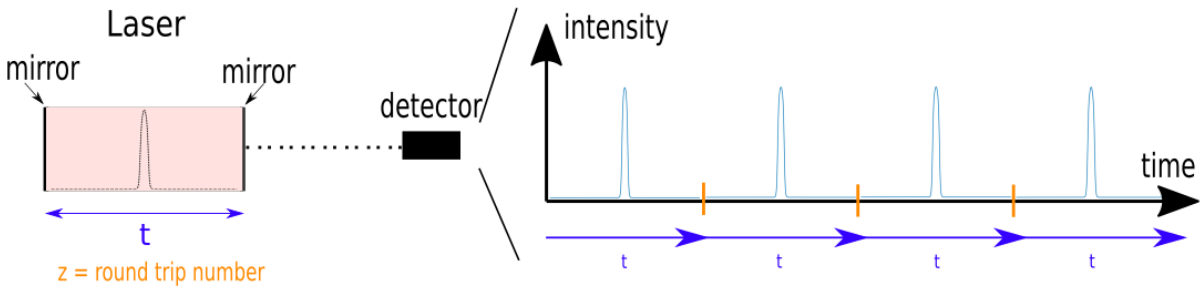

Figure 8: Simplified sketch of a laser experiment to understand the meaning of both coordinates t and z.

The basic principle of a laser is the optical amplification of light within the concept of stimulated emission. For that light is reflected in between two mirrors until it fulfills the condition to leave the laser. Let t describe the distance between those two mirrors. Then it is possible to draw the light profile within the laser, which is depicted as some sort of pulse shape. The laser emits this profile within one round trip and it can be detected using for example a photodiode. There a time-dependent intensity can be measured. Here the distance t becomes a time because each position between both mirrors arrives at a different time at the detector. At the next round trip again a maybe different profile between both mirrors can be drawn and measured at the detector. Let z be the round trip number. Then z can be understood as a time on the time axis of the intensity measurement of the detector: The whole intensity profile consists of smaller ones with width t at the different round trips. That means one can mark the different round trips as time on the time axis. All in all, the normalized propagation distance or round trip number z can be understood as a time scale.
The setup shown in figure 8 is just a simplified sketch to understand the physical meaning of the coordinates. An example for a real experimental setup for a so-called „dissipative-soliton laser“ is shown in figure 9.

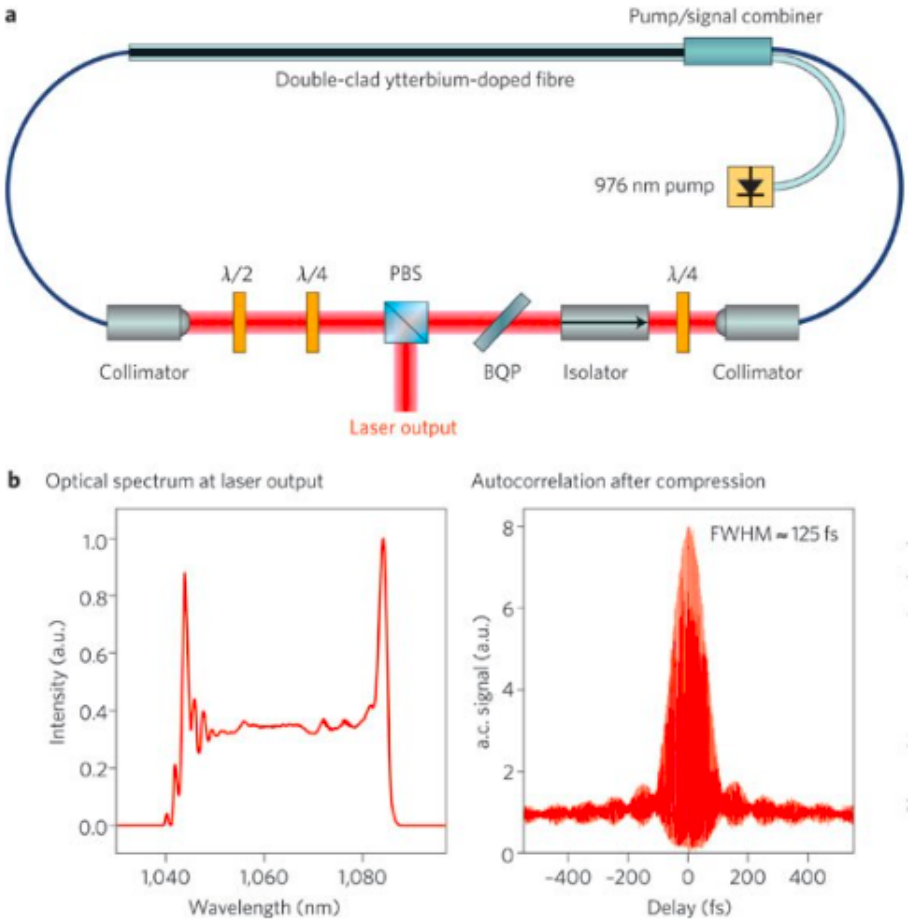

Figure 9: Ytterbium-doped mode-locked fibre laser a) experimental setup b) output spectrum and autocorrelation. [5]

Figure 9a shows the experimental setup of a Ytterbium-doped mode-locked fibre laser. It is called a „dissipative-soliton laser“, because dissipative effects per roundtrip influence pulse formation and stability [5]. In figure 9b the characterization of the output pulse is shown. This design can produce pulses with energies above 31 J at a repetition rate of 70 MHz [5].

3.3 Different solutions of the Ginzburg-Landau equation

In this next paragraph, many different types of solutions of the complex cubic-quintic Ginzburg-Landau equation will be shown to get an overview of the known structures. There are for example localized solutions like a plain pulse or a composite pulse, pulsating and exploding solitons.
There are four important basic types of solutions, which can build more complex structures. They are shown in the following figure 10.

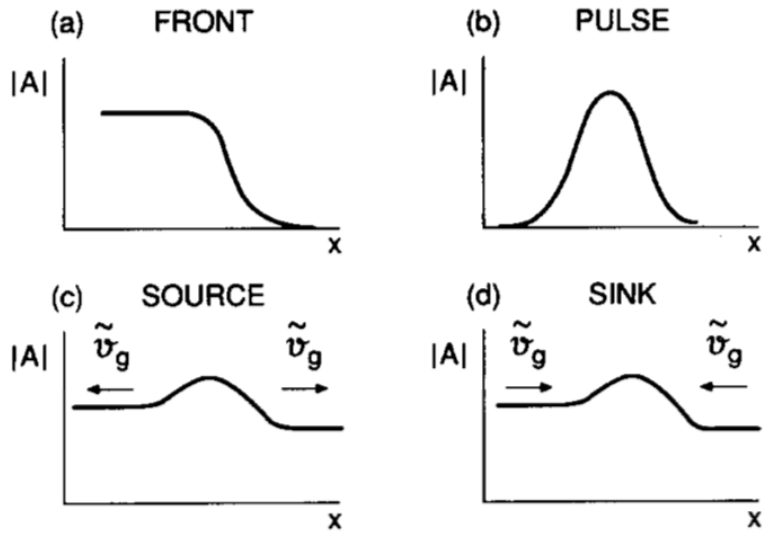

Figure 10: Sketch of different nonlinear wave states of the complex cubic-quintic Ginzburg-Landau equation. $\tilde{v}_g$ is the group velocity in the frame moving with the structure at velocity v, the coordinate x corresponds to t in equation 21. Types: a) front b) pulse c) source d) sink. [30]

The structures which are shown in figure 10 were found to be fixed points of a simplified system of ordinary differential equations of the Ginzburg-Landau equation, see [30]. The solutions are nonlinear wave states of the Ginzburg-Landau equation because an ansatz of the form

$$\begin{aligned} A(t,z) &= \mathrm{e}^{\mathrm{i}\omega z} \cdot \tilde{A}(t-vz) \\ \tilde{A}(t-vz) &= a(\eta) \cdot \mathrm{e}^{\mathrm{i}\phi(\eta)} \end{aligned} \tag{22}$$

with $\eta = t - vz$ for the solution was taken. They found that front solutions are a two-parameter family (plus a discrete set for respectively δ positive and negative). There is a discrete set of sources, same for pulses and a one-parameter family of sinks [30].

There are three basic types of localized solutions of the cubic-quintic Ginzburg-Landau equation, called plain pulse, composite pulse, and also an „expanded structure“ was found. These types were first described in [8]. They observed them by selecting a wide, close to a rectangular shape as the initial condition for a direct numerical analysis of equation 20. The results are shown in the following figure 11.

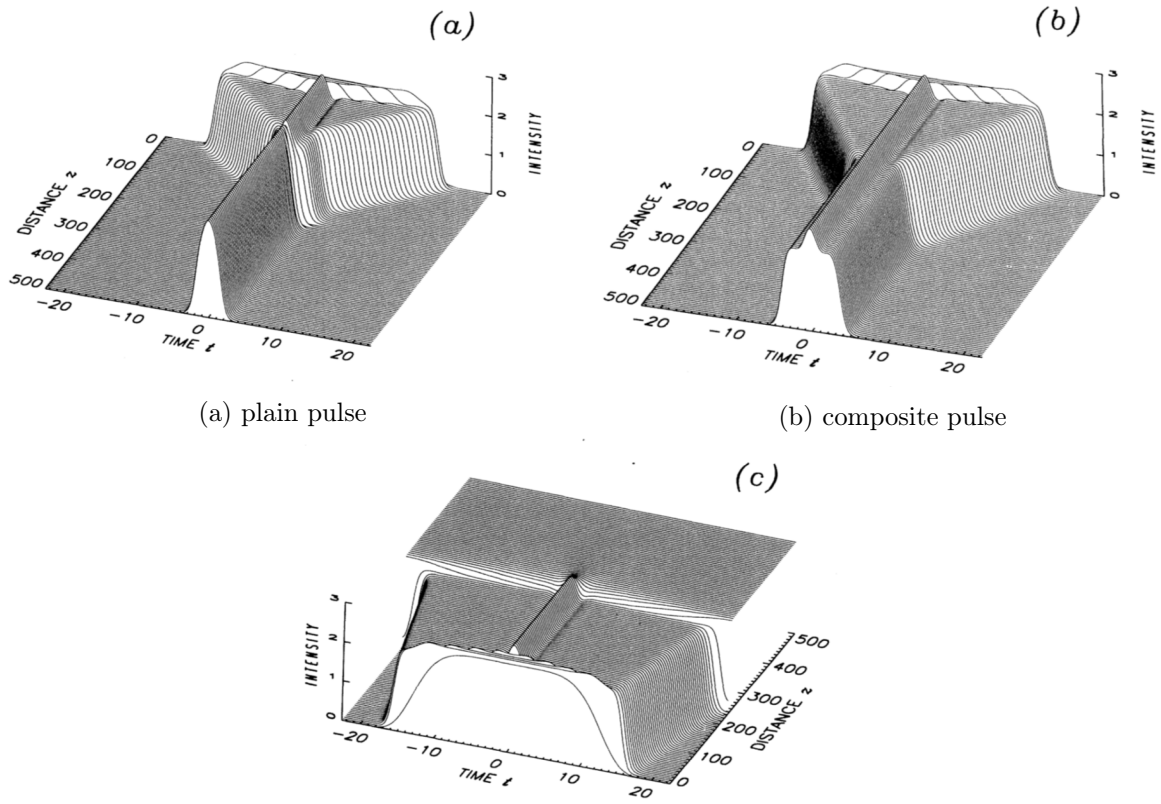

(a) plain pulse

(b) composite pulse

(c) expanded structure

Figure 11: Dynamics of wide rectangular like pulse, building a coherent transition structure consisting of two fronts and one source and then staying in three different types of stable structures for different ε. System parameters: $\delta = -0.5$, $\beta = 0.5$, $\mu = -1$, $\nu = -0.1$ and $D = 1$. a) $\varepsilon = 2.51$ plain pulse b) $\varepsilon = 2.52$ composite pulse c) $\varepsilon = 2.53$ expanded structure (with mirrored z-axis in contrast to the others). [8]

The rectangle-like initial condition builds in all three cases after a few time steps a transition structure, consisting of two fronts and one source. In the first two examples in figure 11a and 11b both fronts move closer to each other and the structure shrinks. As they collide they either build a plain pulse (see figure 11a) or a composite pulse (see figure 11b). When both fronts move away from each other, the structure expands and a homogeneous state is built as shown in figure 11c. The two localized states of the plain and the composite pulse are similar to each other, so their intensity and phase profile, and as well the spectrum is compared in the figure 12.

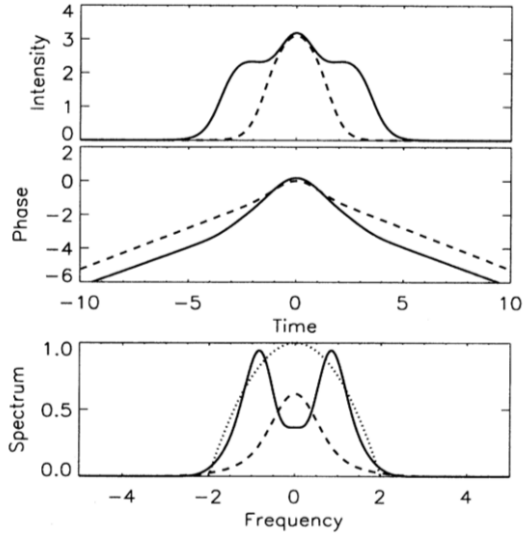

Figure 12: Comparison of the intensity, phase and spectrum between the plain pulse (dashed line) and the composite pulse (solid line). System parameters: $\delta = -0.5$, $\beta = 0.5$, $\mu = -1$, $\nu = -0.1$ and $D = 1$. [8]

The middle peak part of the composite soliton has the same height and form as the peak from the plain pulse. This middle peak of the composite pulse still acts like a source with two motionless fronts at the side, which can be seen in the spectrum. It consists of two peaks, corresponding to the fronts and a drop, the source, in the middle.
Both localized solutions can exist at the same parameter values, as shown in figure 13.

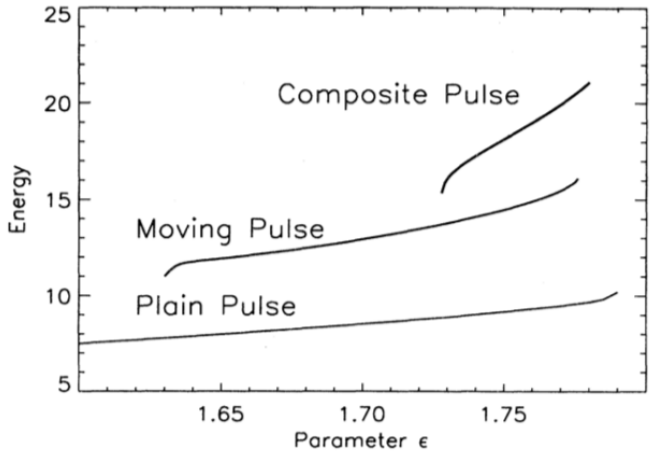

Figure 13: Energy of the plaine, composite and moving pulse in dependance of ε. System parameters: $\delta = -0.5$, $\beta = 0.5$, $\mu = -1$, $\nu = -0.1$ and $D = 1$. [8]

It is shown that there is a regime at about $\varepsilon = 1.75$ where the composite and the plain pulse are both stable. Both bistable solutions are at different energy levels. The energy, in this case, is proportional to the intensity which is the area under the $|A|^2$ curve. The energy of the composite pulse is higher in contrast to the plain pulse, as explained by the intensity profile in figure 12.

In this figure 13 there is also an additional solution type visible. The moving pulse results from an instability of the composite pulse. A formation of the asymmetric moving pulse from a composite pulse is shown in figure 14

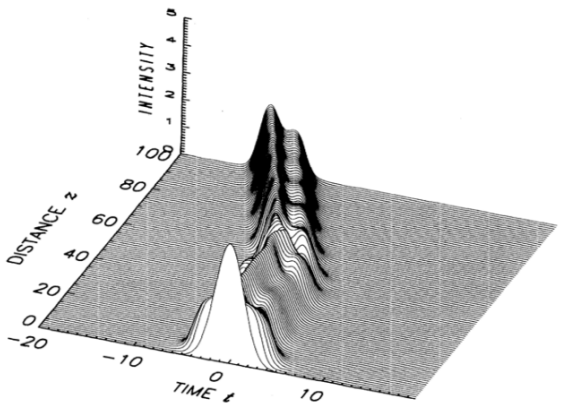

Figure 14: Formation of the moving pulse, after building a composite pulse. System parameters: $\delta = -0.1$, $\beta = 0.5$, $\mu = -0.8$, $\nu = -0.1$, $D = 1$ and $\varepsilon = 1.8$. [8]

It is possible to witness both left- and right-moving pulses. They are related to the symmetry $t \leftrightarrow -t$ of the Ginzburg-Landau equation (eq. 20) [8]. The moving pulse is a nonlinear superposition of a plain pulse and a front that results in an asymmetry which results in a movement of the pulse to the side of the plain pulse. This superposition can be seen in figure 15.

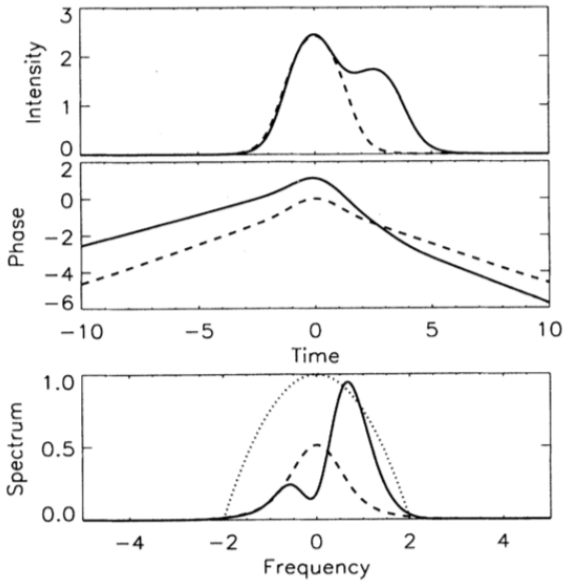

Figure 15: Comparison of the intensity, phase and spectrum between the plain pulse (dashed line) and the moving pulse (solid line). System parameters: $\delta = -0.1$, $\beta = 0.5$, $\mu = -0.8$, $\nu = -0.1$, $D = 1$ and $\varepsilon = 1.8$. [8]

All in all, there are many different types of localized solutions. Now different types of localized soliton structures that change their form with time are shown. Examples are pulsating, exploding,

and creeping solitons. Starting with pulsating solitons, one period of such a soliton is shown in the following picture (figure 16).

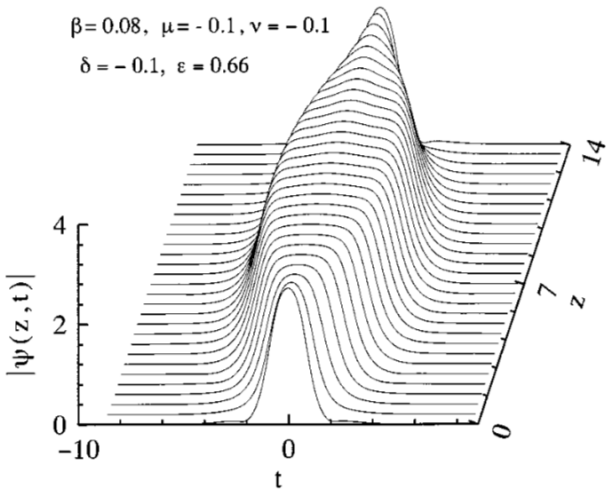

Figure 16: One period of a pulsating soliton. System parameters: $\delta = -0.1$, $\beta = 0.08$, $\mu = -0.1$, $\nu = -0.1$, $D = 1$ and $\varepsilon = 0.66$. [7]

Those pulsating solitons build limit cycles because they change their form with time z: There is a periodic repetition in a pulsating form. With the change of form also the pulse energy changes with time. Such solitons can be observed when stationary pulse solutions become unstable in isolated regions in parameter space [7].

A pulsating soliton can undergo period-doubling bifurcations for example by variation of ε. After such a bifurcation, instead of the repetition of the simple shape after only one period, it repeats itself after two pulsation cycles. Therefore it has a double periodicity. At another period-doubling bifurcation, another duplication occurs so that there is quadruple periodicity. The distance between bifurcation points $\varepsilon_{n+1} - \varepsilon_n$ gets smaller for higher n until a transition into chaos occurs at ε_∞, building a Feigenbaum diagram like the logistic map (see [21]). In this case, it results in the following diagram 17

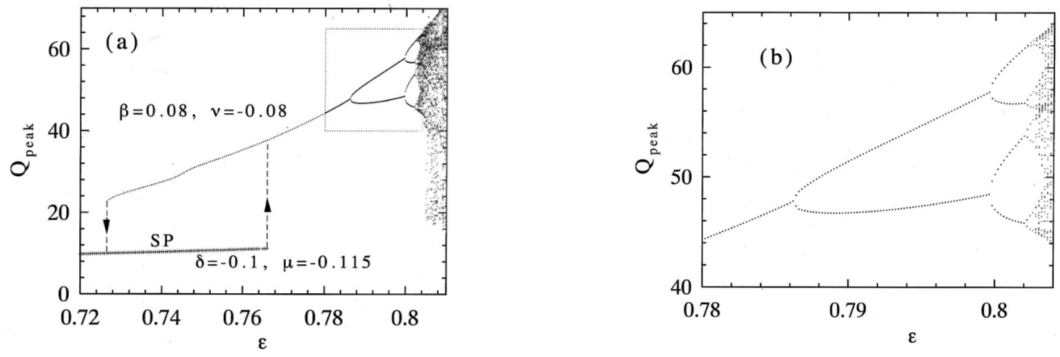

Figure 17: Poincaré map of peak energy versus ε with system parameters: $\delta = -0.1$, $\beta = 0.08$, $\mu = -0.115$, $\nu = -0.08$ and $D = 1$. In a) the whole diagram with stationary pulse and pulsating pulse including a hysteresis transition process is shown. On the right side, the periodic doubleing process is shown. A zoom of it is shown in subfigure b). [7]

To draw this diagram a time interval set to $z = 500$ for a certain value was numerically simulated. Then the energy Q was calculated at each step resulting in an oscillating pattern due to the pulsating shape. Each maximum is then taken and drawn into the diagram. A simple pulsating soliton as in figure 16 has just one always repeating peak energy value. Therefore just one point is present in the diagram for that ε value. If double periodicity is present there are two different peak energy values and two different points can be seen in the poincaré map at that given ε value. Like this, the periodic doubling behaviour can be understood which is depicted in figure 17. In contrast, a chaotic regime is characterized by a lot of different points at random energy values.
To summarize, a lot of different concepts of nonlinear physics can be seen when discussing pulsating solitons. But there are other types of localized solitons that change with time. Another class are the creeping solitons which are shown in figure 18

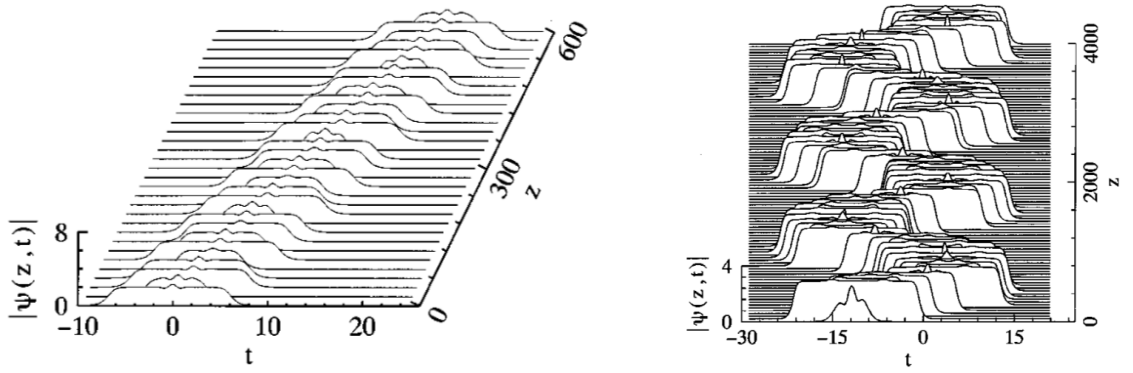

(a) example 1 (b) example 2

Figure 18: Two examples for creeping solitons. a) System parameters $\delta = -0.1$, $\beta = 0.101$, $\mu = -0.3$, $\nu = -0.101$, $D = 1$ and $\varepsilon = 1.3$. b) System parameters $\delta = -0.1$, $\beta = 0.08$, $\mu = -0.11$, $\nu = -0.08$, $D = 1$ and $\varepsilon = 0.835$. [7]

In figure 18a there is a rectangular pulse with two fronts and a sink at the top. Those two fronts are pulsating asymmetrically at both sides of the sink which results in a movement to the side of the whole soliton. The pulse shape is in the form of a composite soliton. A creeping soliton can have two different frequencies in its motion, an example is shown in figure 18b. This soliton moves with a constant speed back and forth around a fixed value.
Creeping solitons form a different type to pulsating and exploding solitons because they exist in an isolated parameter space [7]. Speaking of exploding solitons, they are the last here described example. The evolution of an exploding soliton is shown in figure 19.

The evolution, shown in figure 19, starts with a stationary localized soliton, which is stable in form for a few time steps. Then the from destabilizes and builds smaller peaks erupting from the middle and moving to the sides. This destabilization gets bigger until the whole structure consists of seemingly random peaks. Afterwards the form of the stationary localized soliton regains stability and this exploding process starts again. Thereby this process is not periodic because two explosions do not look the same, but it always ends up being the same localized structure.

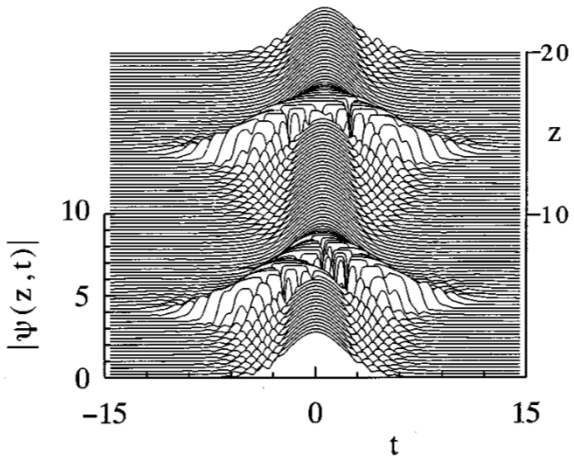

Figure 19: Time evolution of two soliton explosions. System parameters: $\delta = -0.1$, $\beta = 0.125$, $\mu = -0.1$, $\nu = -0.6$, $D = 1$ and $\varepsilon = 1.0$. [7]

The stability of exploding solitons was analyzed using a continuation approach in [12]. The basic idea behind continuation is explained in section 4.2 „Continuation approach“ because the same method will be used in this work. Their numerical results are shown in figure 20

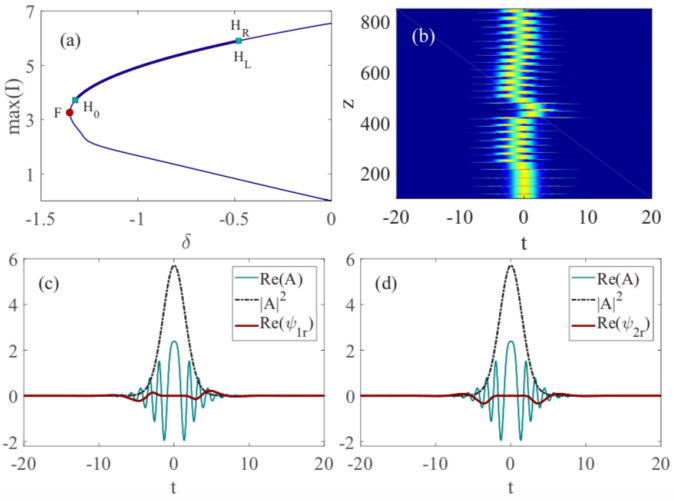

Figure 20: Numerical analysis with system parameters: $\beta = 0.125$, $\mu = -0.1$, $\nu = -0.6$, $D = 1$ and $\varepsilon = 1.0188$. a) Bifurcation diagram of a localized soliton with continuation parameter δ and as a measure the maximum intensity. b) Direct numerical simulation of the space-time evolution of a symmetrically-asymmetrically expolding localized soliton. c)/d) intensity profile (black), real part of critical eigenvalue function (red) and real part of the field (cyan) at $\delta = -0.6$ for asymmetric and symmetric soliton explosions. [12]

In figure 20a a bifurcation diagram with the maximum intensity of the field against δ as an axis is shown. The localized soliton solution branch emerges subcritical from a homogenous zero state, which destabilizes at $\delta = 0$, then goes through a fold point (F) and stabilizes with a hopf bifurcation (H_0). At that point, a pair of complex eigenvalues connected to symmetrical pulsation is stabilized. Afterwards, a double hopf bifurcation (H_L, H_R) occurs and destabilizes the system.

They are connected to symmetric and asymmetric perturbations as seen in the eigenmodes in the figures 20c and d [12]. They showed that the double hopf bifurcations splits into two when taking into account higher-order terms.

3.4 Soliton resonance

An experimentally interesting phenomenon is ultra-short high-energy laser pulses. Dissipative solitons with high energy were found in the context of passively mode-locked lasers. By varying D which corresponds to an anomalous or normal dispersion regime, the energy of the pulses changes and it is forming a resonance. This so-called dissipative soliton resonance was discussed in [15], [16] and [18]. The results will be shortly summarized here.
Firstly the results in the normal dispersion regime $D < 0$ will be shown. In [15] they used a split-step Fourier method within a direct numerical analysis of the complex cubic-quintic Ginzburg-Landau equation to draw a diagram by varying the dispersion parameter D as it is shown in figure 21.

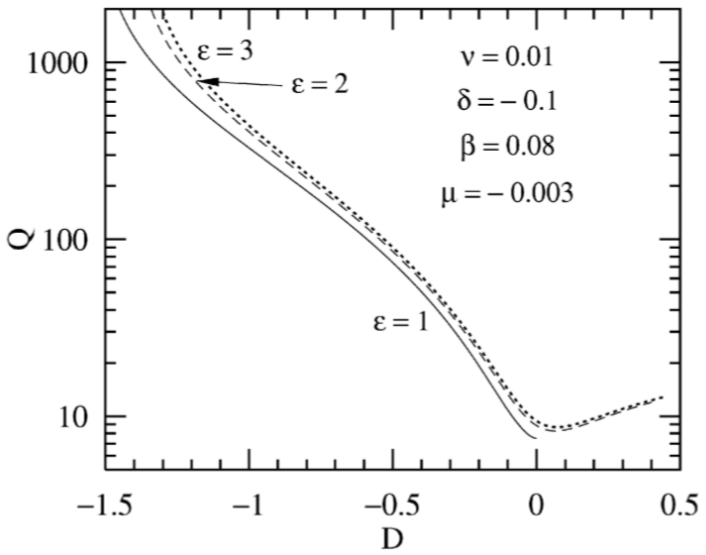

Figure 21: Soliton energy Q against D the dispersion parameter for three different values of ε. System parameters: $\delta = -0.1$, $\beta = 0.08$, $\mu = -0.003$ and $\nu = -0.01$. [15]

It is clear that the soliton energy rises with an increasing absolute value of D when looking at figure 21. Also, the energy value reaches a very high value of over 1000 dimensionaless units. The slope at that position suggests that even higher energy values might be possible which could even increase indefinitely. The energy changes its order of magnitude rapidly as the logarithmic scale on the ordinate suggests. This result is replicated in the same form for all three different ε values. The three curves are just shifted to the side but the basic shape is maintained.
To show that the energy Q can increase indefinitely and that a resonance occurs, an approximation using a technique called the method of moments [34] was made, see [16]. Here five moments

$$
\begin{aligned}
Q &= \int_{-\infty}^{\infty} |A|^2 \ \mathrm{d}t \\
P &= \frac{1}{2} \int_{-\infty}^{\infty} (AA_t^* - A^* A_t) \ \mathrm{d}t \\
I_1 &= \int_{-\infty}^{\infty} t\,|A|^2 \ \mathrm{d}t \\
I_2 &= \int_{-\infty}^{\infty} (t - t_0)^2\,|A|^2 \ \mathrm{d}t \\
I_3 &= \frac{1}{2} \int_{-\infty}^{\infty} (t - t_0)(A^* A_t - AA_t^*) \ \mathrm{d}t
\end{aligned}
\tag{23}
$$

were defined. They are not conserved for the complex cubic-quintic Ginzburg-Landau equation. Then the system was truncated by taking the derivative with respect to z of all five moments and a trial function

$$
A(t, z) = A_0 \cdot \mathrm{e}^{-\frac{t^2}{w^2} - \frac{t^4}{4mw^4}} \cdot \mathrm{e}^{\mathrm{i}ct^2} \tag{24}
$$

was definite to approximate the localized solutions of the Ginzburg-Landau equation where $A_0(z)$ is the amplitude, $w(z)$ is the width and $c(z)$ is the chirp of the soliton and m an adjustment constant. Using this ansatz a dynamical system of three coupled differential equations was derived and a numerical analysis was performed. To see how accurate this model is in comparison to the ansatz using the complex cubic-quintic Ginzburg-Landau equation as discussed before, the region of stable solution were compared, as shown in figure 22.

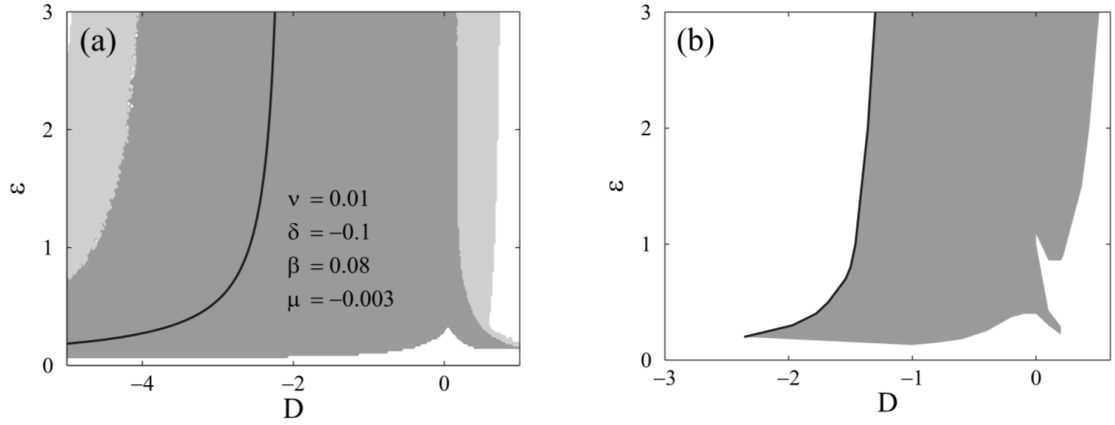

(a) moment of methods

(b) results of [15]

Figure 22: Comparison of a) stable fixed points of the dynamical system using the method of moments and b) numerical simulations of the Ginzburg-Landau equation from [15]. The black curve is the Resonance curve and in light gray oscillating solutions like pulsating solitons are depicted. They are not shown in diagram b). [16]

As it can be seen in figure 22 the approximation of [16] is in relatively good agreement with the results in [15]. Now, this model can be used to reproduce figure 21. The results are shown in figure 23.

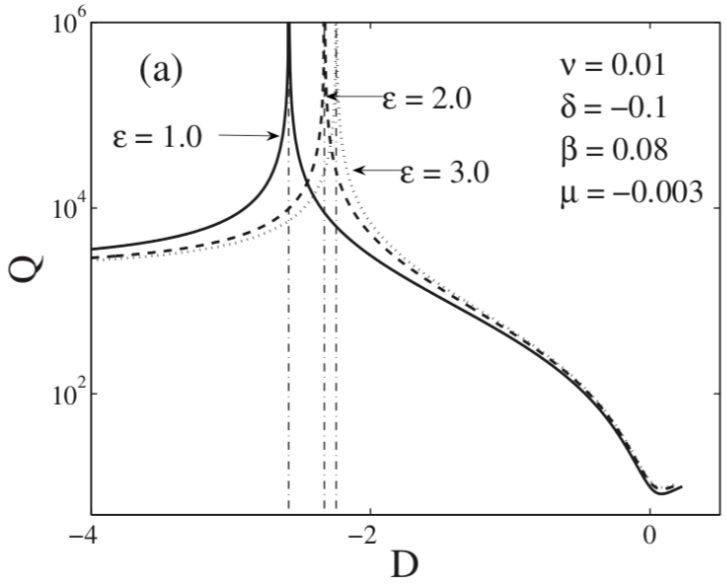

Figure 23: Soliton energy Q against D the dispersion parameter for three different values of ε from the modell in [16]. System parameters: $\delta = -0.1$, $\beta = 0.08$, $\mu = -0.003$ and $\nu = -0.01$. [16]

The diagram in figure 23 shows a typical resonance curve with a nearly asymptotic increase of the soliton energy. The left-hand side of the curve is an artifact of the approximation and may represent unstable solutions. As in figure 21, for different values of ε, the whole curve is shifted to the side, but the energy which could be reached is an order of magnitudes higher than before in figure 21. Near the resonance, the soliton increases in width while keeping its amplitude constant at a value of about

$$A \approx \sqrt{-\frac{\varepsilon}{\mu}} \tag{25}$$

[16]. The resonance curve in figure 22a could be approximated using system parameters and one gets

$$D \approx \left(\frac{3.8\nu}{\mu} - \frac{6.333}{\varepsilon}\right)\beta \tag{26}$$

[16]. The resulting curve is approximately in agreement with the resonance curve shown in figure 22. By now setting the parameters in equation 26 to the values shown in figure 23 one can get an approximation for the value D where the resonance occurs. This value is marked with dashed horizontal lines in figure 23 and is in good agreement with the results.
In this section, the phenomenon of soliton resonance was only discussed in the normal dispersion

regime. As shown in [18] it can also occur in the anomalous regime. Here again simulations of the complex cubic-quintic Ginzburg-Landau equation using a split-step technique were done. The results are shown in figure 24.

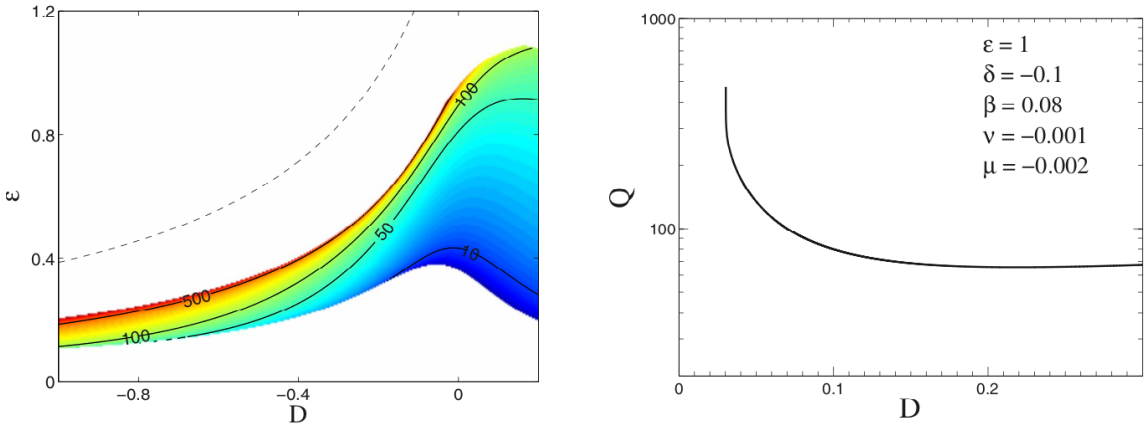

(a) Region of existence of stable solitons

(b) Dissipative soliton resonance

Figure 24: a) The region of existence of stable solitons in the (ε, D) plane. The energy Q of the soliton is marked with color where red corresponds to the highest values and blue to the lowest. System parameters: $\delta = -0.1$, $\beta = 0.08$, $\mu = -0.002$ and $\nu = -0.001$. b) Dissipative soliton resonance in anormalous dispersion regime, with resonance at about $D \approx 0.03$. System parameters: $\delta = -0.1$, $\beta = 0.08$, $\mu = -0.002$, $\nu = -0.001$ and $\varepsilon = 1$. [18]

In figure 24a, the region of existence of stable solitons in the (ε, D) plane is shown. The dashed line corresponds to the approximation in [16]. The diagram shows that the resonance effect is more dominant in the normal dispersion regime but can also occur in the anomalous regime as shown in figure 24b for $\varepsilon = 1$. This value of ε was used, because it is near the resonance curve in figure 24a for the given set of parameters. It can be seen that the energy increases but is limited by numerical errors [18].

4 Numerical methods

This work aims to evaluate these localized solutions of the Ginzburg-Landau equation and the occuring soliton resonances, described in section 3.3 „Localized solutions of the Ginzburg-Landau equation“ and 3.4 „Soliton resonance“, using bifurcation diagrams. This will be done using numerical methods, where two methodically different methods will be applied. They can be separated into a direct and an indirect numerical approach. In the direct approach, a solution to the equation is approximated directly without iterating to get a more exact solution. The latter is exactly what is done in an indirect approach, like the here used continuation approach. The direct method is used to get an initial solution for the indirect continuation method. How this works in detail, is described in the following section.

4.1 Direct numerical method

The name „direct method“ originates from the idea of getting the numerical solution of an equation by directly calculating it. Due to a finite number of steps, rounding errors, and possible approximations done by calculating the solution, it will be an approximate solution. This method stands in contrast to an „iterative method“, where an initial solution is improved step by step.
Such a direct method was used in [25], results shown for example in figure 16. It was used to get different types of solutions at different parameter regimes of the Ginzburg-Landau equation. In principle, the same can be done in this work to confirm the previous results, but that is not the reason it is useful here. The direct numerics solutions will be used as an initial solution for the numerical continuation, which enables following its branch and in the end draw a bifurcation diagram.
The direct method used here is the (pseudo-) spectral method. It can be used on a nonlinear partial differential equation like the complex cubic-quintic Ginzburg-Landau equation which will be examined. By taking the Fourier transformation, the numerical problem simplifies to an ordinary differential equation, that is easier to work on. A typical framework is given by the Runge-Kutta methods. This is a family of explicit and implicit methods, like the Euler method or the RK4-method, which are used to obtain different approximate solutions of an ordinary differential equation. So in the end those two methods need to be used for the Ginzburg-Landau equation. In the last part of this section, it is shown how it was done.

4.1.1 Numerical methods for an ordinary differential equation

The central problem is to numerically approximate the solution of an initial value ordinary differential equation

$$\frac{\mathrm{d}y(t)}{\mathrm{d}x} = f(x, y) \qquad \text{with} \qquad x(0) = x_0 \tag{27}$$

where $y : \mathbb{R} \to \mathbb{R}$ and $f : [a, b] \times \mathbb{R} \to \mathbb{R}$ are functions and $[a, b]$ is a closed interval. Here the problem is shown in a simplified way, in general the functions can exists on a more dimensional

functional space.
The basic idea from Euler, was now to describe the t-axis with a grid of $n+1$ equally distanced lattice points $x_0, x_1, ..., x_n$ with corresponding values $y_0, y_1, ..., y_n$ of the function $y(x)$ at the given lattice points. If a point (x_0, y_0) is known, the next one can be calculated by the following formula:

$$y_1 = y_0 + h \cdot \frac{\mathrm{d}y(x_0)}{\mathrm{d}x} = y_0 + h \cdot f(x_0, y_0) \tag{28}$$

where $h = x_n - x_{n-1}$ is the distance between two lattice points. This formula is based on the following approximation explained by this illustration 25

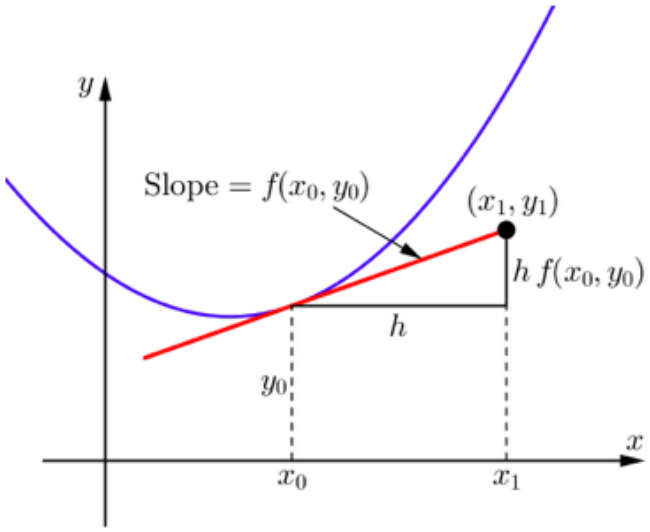

Figure 25: Approximation of the solution using the Euler method. [35]

As shown in figure 25 the basic idea behind the Euler method is the usage of the definition of a derivative. Starting at the known point (x_0, y_0), if now the slope at the point is known, then the height difference between y_0 and y_1 can be approximated by multiplying the slope with the equidistant step size h. To finally get an expression for y_1, one can add the previous height to this term. After also remembering equation 27, the expression in equation 28 follows.
Applying formula 28 again and again, the whole function $y(x)$ can be approximated on the lattice points and the iterative procedure is given by

$$y_n = y_{n-1} + h \cdot f(x_{n-1}, yn - 1). \tag{29}$$

[36]. After all, this formalism has a high order of inaccuracy [37], so the mathematician Runge improved upon this in his work published in 1895 [38]. He used the midpoint and the trapezoidal rules to do so. The not yet calculated mid and endpoint were given a preliminary approximation using the Euler method.
After that idea, especially Heun and Kutta developed the algorithm further so that there was a

family of explicit and implicit Runge-Kutta methods, which all could be used to solve ordinary differential equations [37]. This family of (explicit) methods of m-th stage can be described with the following formula 30

$$y(x_{n+1}) := y(x_{n+1}) = y_n + h \cdot \sum_{i=1}^{m} c_i k_i \tag{30}$$

with

$$\begin{aligned} k_1 &= f(x_n, y_n) \\ k_2 &= f(x_n + \alpha_2 h, y_n + h\beta_{2,1} k_1(x_n, y_n)) \\ &\vdots \\ k_m &= f\left(x_n + \alpha_m h, y_n + h \cdot \sum_{j=1}^{m-1} \beta_{m,j} k_j\right). \end{aligned} \tag{31}$$

A method of this family can be specified by setting the parameters m, α_i (for $i = 2, 3, ..., m$), $\beta_{i,j}$ (for $1 \leq j < i \leq m$) and c_j(for $i = 1, 2, ..., m$) to a certain value [39].
In this work, a classical fourth-order Runge-Kutta method (short: RK4) was used, which is given by

0				
$\frac{1}{2}$	$\frac{1}{2}$			
$\frac{1}{2}$	0	$\frac{1}{2}$		
1	0	0	1	
	$\frac{1}{6}$	$\frac{1}{3}$	$\frac{1}{3}$	$\frac{1}{6}$

Figure 26: Butcher tableau. [40]

$$\begin{aligned} k_1 &= f(x_n, y_n) \\ k_2 &= f\left(x_n + \frac{h}{2}, y_n + \frac{h}{2} k_1\right) \\ k_3 &= f\left(x_n + \frac{h}{2}, y_n + \frac{h}{2} k_2\right) \\ k_4 &= f\left(x_n + h, y_n + h k_3\right) \end{aligned} \tag{32}$$

$$y_{n+1} = y_n + \frac{h}{6} \cdot (k_1 + 2k_2 + 2k_3 + k_4).$$

The order of the numerical error is connected to the order of the Runge-Kutta method. The fourth-order is given by

$$|y_{n+1} - y(t_{n+1})| \leq \mathcal{O}(h^5), \tag{33}$$

where $y(t_{n+1})$ describes the exact solution of the differential equation [36]. An approximation of the numerical error is indispensable, when interpreting numerical results, thus it is given here. Comparing equation 33 to the numerical error of the Euler method of $\mathcal{O}(h^2)$ [36], the improvement is visible. That comparable low error reinforces, why the classical fourth-order Runge-Kutta method is used in this work.

4.1.2 Numerical methods for a partial differential equation

In an ordinary differential equation, there are just derivatives with respect to one parameter. This parameter often corresponds to a time or space derivative in physics. Examples of such a type of differential equations are the newtons equation of motion, the Lotka-Volterra equations, or the Lorenz system. But in a vast amount of applications there is not just a derivative with respect to one parameter, but to more. An example for this so-called partial differential equation is the one to be examined complex quintic-cubic Ginzburg-Landau equation (eq. 21)

$$\frac{\partial A}{\partial z} = \left(\beta + \frac{D}{2}\mathrm{i}\right)\frac{\partial^2 A}{\partial t^2} + \delta A + (\varepsilon + \mathrm{i})\,|A|^2\,A + (\mu + \nu\mathrm{i})\,|A|^4\,A$$

As described before there is a derivative with respect to the cavity round-trip number z and as well with respect to the retarded time t. Due to the two distinct derivatives, the Runge-Kutta method can not be applied directly. There needs to be some way to embed the t-derivative into the existing algorithm. One example of how to cope with it is the pseudo-spectral approach. Here the derivative can be expressed by using a Fourier transformation.
The Fourier transformation of an integrable function $f(x)$ is defined by

$$\mathcal{F}(f) = \tilde{f}(k) = \int_{-\infty}^{\infty} f(x)\cdot \mathrm{e}^{-\mathrm{i}kx}\mathrm{d}x. \tag{34}$$

To understand how that helps this definition needs to be applied to a derivative $\frac{d}{dx}$. By doing that, it follows

$$\begin{aligned}
\mathcal{F}\left(\frac{d}{dx}f\right) &= \int_{-\infty}^{\infty}\left(\frac{d}{dx}f(x)\right)\cdot \mathrm{e}^{-\mathrm{i}kx}\mathrm{d}x \\
&= 0 - \int_{-\infty}^{\infty} f(x)\cdot\left(\frac{d}{dx}\mathrm{e}^{-\mathrm{i}kx}\right)\mathrm{d}x \\
&= \mathrm{i}k\cdot\int_{-\infty}^{\infty} f(x)\cdot \mathrm{e}^{-\mathrm{i}kx}\mathrm{d}x \\
&= \mathrm{i}k\cdot\tilde{f}(k).
\end{aligned} \tag{35}$$

Therefore the derivative $\frac{d}{dx}$ can be expressed as a multiplication by $\mathrm{i}k$ in Fourier space. This phenomenon is now used in the (pseudo-) spectral approach: Here the differential equation will be numerically solved in real space, but the disruptive derivatives for the Runge-Kutta method are handled in Fourier space by using multiple Fourier transformations. That results in the ability to apply the Runge-Kutta algorithm for a partial differential equation.

4.1.3 Implementation of the Ginzburg-Landau equation

This segment will be presented how the pseudo-spectral approach and the Runge-Kutta method are applied to the Ginzburg-Landau equation. First from a more mathematical standpoint and then what it results in for the program.

Mathematically the pseudo-spectral approach needs to be applied to the equation. Looking at the sorted form of the Ginzburg-Landau equation (21)

$$\frac{\partial A}{\partial z} = \left(\beta + \frac{D}{2}\mathrm{i}\right)\frac{\partial^2 A}{\partial t^2} + \delta A + (\varepsilon + \mathrm{i})\,|A|^2 A + (\mu + \nu\mathrm{i})\,|A|^4 A.$$

only the blue marked term needs to be rewritten using Fourier transformation as in the definition in equation 34. Because there is no multiplication of two fields, there is no problem with convolution and it follows

$$\left(\beta + \frac{D}{2}\mathrm{i}\right)\frac{\partial^2 A}{\partial t^2} = \left(\beta + \frac{D}{2}\mathrm{i}\right)\cdot\mathcal{F}^{-1}(-k^2\cdot\mathcal{F}(A)). \tag{36}$$

Inserting this into equation 21, the pseudo-spectral ansatz gives

$$\frac{\partial A}{\partial z} = \left(\beta + \frac{D}{2}\mathrm{i}\right)\cdot\mathcal{F}^{-1}(-k^2\cdot\mathcal{F}(A)) + \delta A + (\varepsilon + \mathrm{i})\,|A|^2 A + (\mu + \nu\mathrm{i})\,|A|^4 A, \tag{37}$$

which is an ordinary differential equation when using Fourier transformations. Now the equation is in the form, in which it can be numerically analyzed using the Runge-Kutta algorithm. How this is done exactly as shown in the following paragraph.
The program for the direct numerical analysis is written in python, which is a simple and sufficient language for what is needed. The program starts by first importing python packages to include simple math tasks (line 1) and drawing pictures of the results (line 2).

```
1 import numpy as np
2 import matplotlib.pyplot as plt
```

After that, the parameter regime of the Ginzburg-Landau equation, which should be examined, is defined (lines 3 to 9). Followed by the basic parameters of the numerical analysis like step size and the number of grid points (lines 11 to 16).

```
3 # define parameters
4 beta=0.08
5 D=1.0
6 delta=-0.2
7 epsilon=0.66
8 mu=-0.1
9 nu=-0.1
10
11 # settings
12 Tend = 500
13 h = 0.00005 # step size for z-steps
```

```
14 totaltimesteps = int(Tend/h) # total z-steps
15 N=2048 # number grid points in t-space
16 L=12*np.pi # length of t-space
```

Next up is the definition of arrays for the different axis in real and Fourier space (lines 17 to 20) and defining some initial guess (lines 22 to 27). Here a gauss-like function is taken because it gives some pulse shape, which is expected when compared to other results (see figure 11). For other solution types, like a continuous wave solution, another initial guess is better suited.

```
17 # define t,z and k space
18 t = np.linspace(int(-L/2),int(L/2),N,endpoint = False)
19 z = np.linspace(0,Tend,totaltimesteps+1)
20 k = np.fft.fftfreq(N,L/(N*2*np.pi)) # mesh in k-space: k_n=dx/(2*pi)
21
22 # initial value function
23 def A0(t):
24     return 10* np.exp(-t**2/1.5)
25
26 A = np.zeros(t.size, dtype=np.complex)
27 A[:]= A0(t)
```

Now the partial differential equation is simplified to an ordinary differential equation by using the pseudo-spectral method. Therefore the right-hand side of the equation can be written using the numerical (inverse) Fast-Fourier transformation and equation 37. This is expressed in the definition of a function for the right-hand side (lines 26 to 28).

```
28 # rhs of the ODE using pseudo-spectral method
29 def rhs(k,beta,D,delta,epsilon,mu,nu,A):
30     return (beta+(D/2)*1j)*np.fft.ifft(-k**2 * np.fft.fft(A)) + delta*
          A + (epsilon+1j)* abs(A)**2 *A +(mu+nu*1j)*abs(A)**4 * A
```

And in the last step, the classical Runge-Kutta method is applied to this right-hand side of the ordinary differential equation (line 31-38).

```
31 # RK4 algorithm
32 for i in range(totaltimesteps):
33     k1 = rhs(k,beta,D,delta,epsilon,mu,nu,A[:])
34     k2 = rhs(k,beta,D,delta,epsilon,mu,nu,A[:]+(h/2)*k1)
35     k3 = rhs(k,beta,D,delta,epsilon,mu,nu,A[:]+(h/2)*k2)
36     k4 = rhs(k,beta,D,delta,epsilon,mu,nu,A[:]+h*k3)
37
38     A[:] = A[:] + (h/6) * (k1 + 2*k2 + 2*k3 +k4)
```

So in line 38 the approximation of the field $A(t, z)$ is given for a specific time z corresponding to the index of the loop (line 32). With this information, there can be done a variety of things like a profile plot of the field for a given z, a space-time plot, or just an export of the solution after all time steps to import as an initial solution in the numerical continuation.

4.2 Continuation approach

The second method is the arclength continuation method, which can find and follow solutions branches and detect bifurcations to be able to draw bifurcation diagrams. This method is applied using pde2path, which is a matlab package for bifurcation and continuation analysis of elliptic partial differential equations, see [19]. It uses the finite element method to reiterate an approximate solution to get a better residuum and therefore a more exact approximation. Due to this, it is an indirect numerical method, in contrast to the Runge-Kutta method as discussed in the last paragraph.
In the following section, the mathematical basics behind the finite element method will be displayed firstly, to get an better understanding of the underlying principles which are used in the pde2path formalism. The basic feature of the continuation approach will be explained afterwards. In the last section, the implementation of the complex cubic-quintic Ginzburg-Landau equation is shown.

4.2.1 Finite element method

The finite element method (or short FEM) is a widely used numerical method to approximate solutions of differential equations. It can be used for elliptic partial differential equations and also for space discretization in parabolic equations. The finite element method is a Galerkin method, which uses finite elements as smaller and simpler parts to describe the problem. In this section, an overview of the mathematically methods will be shown, for more detail see [41].
Galerkin methods are based on the energy minimization principle. In physics, a system always strives for the state of minimal energy. So if X is a Function space and $E : X \to \mathbb{R}$ an energy functional, then the solution u can be derived by

$$u = \arg\max_{x \in X}(E(x)) \tag{38}$$

Now the subspace $X_h \subset X$ discretizes it to get a numerical discretization problem

$$u_h = \arg\max_{x_h \in X_h}(E(x_h)) \tag{39}$$

with u_h being the approximate solution [41]. To now get u_h as the minimum of the energy functional, the functional derivative

$$\frac{\mathrm{d}}{\mathrm{d}\varepsilon} E(u_h + \varepsilon x_h) \Big|_{\varepsilon=0} = 0 \tag{40}$$

for every test function $x_h \in X_h$, can be taken. This idea helps now by the evaluation of a partial

differential equation because an elliptic partial differential equation can be derived from this energy minimization so that it is mathematically equivalent to solving the equation.
To write this in a more mathematical way, a general Ritz-Galerkin method of a variational problem with a bilinear form $b : X \times X \to \mathbb{R}$ and a function of the dual space of X

$$b(u, \varphi) = f(\varphi) \qquad \forall \varphi \in X_h \tag{41}$$

is definite by

$$b(u_h, \varphi_h) = f(\varphi_h) \qquad \forall \varphi_h \in X_h. \tag{42}$$

[41]. The Existence and uniqueness of u_h follow by the Lax-Milgram theorem. Also, the equation 42 can be rewritten as a matrix-vector equation and therefore can be solved numerically.
As explained before the finite element method is also a type of Ritz-Galerkin method. The different types can be differentiated by the choice of the subspace X_h. The special choice of X_h also defines the finite element method. It divides the space Ω into non-overlapping subspaces of geometrical objects. A simple example are simplicial Lagrange elements. In two dimensions they consist of triangles, in three dimensions tetrahedrons, and in n dimensions they are simplexes. A s-dimensional simplex in $\mathbb{R}$ is defined by

$$T := \left\{ x \in \mathbb{R}^d \,\middle|\, x = \sum_{i=0}^{s} \lambda_i a_i,\ \lambda_i \leq 0,\ \sum_{i=0}^{s} \lambda_i = 1 \right\}, \tag{43}$$

with $s \in \{1, ..., d\}$ and the points $a_0, ..., a_s \in \mathbb{R}^d$ are called edges [41]. Those simplexes now need to cover the space, on which the elliptic equation is defined Ω, in a certain way: A permissible triangulation τ_h is needed, which is defined by

$$\tau_h := \{ T_j \mid j = 1, ..., m \text{ and } T_j \text{ is } d\text{-dimensional simplex in } \mathbb{R}^d \} \tag{44}$$

with the property, that if the intersection of two different simplexes $T_i \cap T_j$ consists of either one point, which is the corner point of T_i and T_j or multiple points, then $T_i \cap T_j$ is the edge of T_i and T_j [41]. An example for such triangulation is shown in the following figure 27.

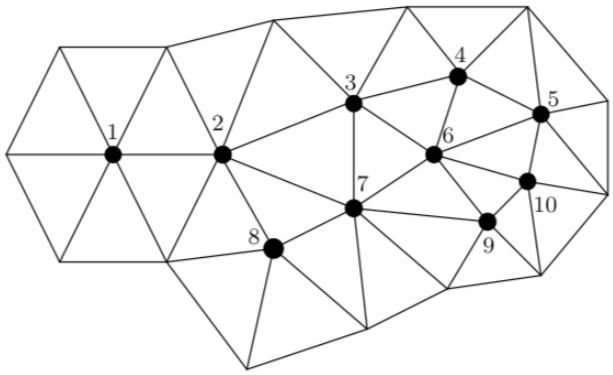

Figure 27: Triangulation with triangles of a polygon Ω with arbitrary numbered nods [42].

To now get the total definition of the space X_h defined by the Galerkin method, there also needs to be test functions $\varphi_1, \varphi_2, ..., \varphi_n$ to be able to model the partial differential equation. Those functions are not equal to zero just on one simplex. An example in one dimension are triangle like functions shown in the following figure 28

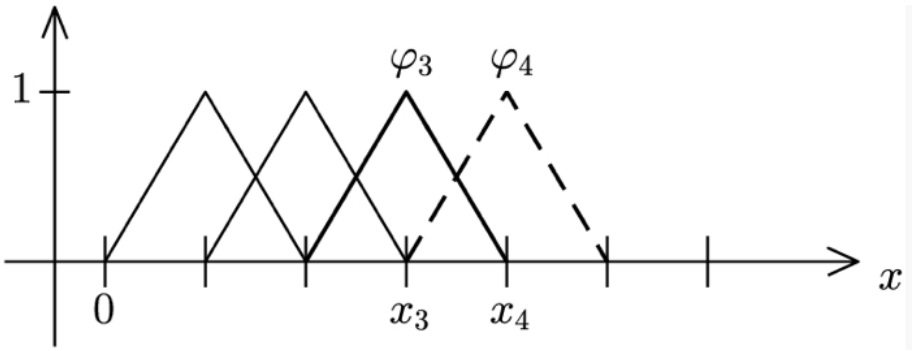

Figure 28: Some triangular shaped test functions shown in an one dimensional space Ω [43].

The picture shows that in one dimension the triangulation of space just appears as a grid on the x-axis with the simplexes being intervals with corner points. The test functions φ_i are defined on distinct intervals but are zero in others.
The test functions φ_j are used to describe the numerical solution u_h on the corner points of the simplex by calculating

$$u_h = \sum_j c_j \varphi_j \tag{45}$$

with c_j being the value of u_h on the corner points.
Following this, derivatives are defined in principle by the weak derivative: Normally with this method, it is possible to assign a derivative to a non-differentiable function ψ. For a continuously differentiable test function φ on interval $I = [a, b]$ the derivative of function ψ is given by

$$\int_I \frac{\partial \phi(x)}{\partial x} \cdot \psi(x) \, \mathrm{d}x = -\int_I \phi(x) \cdot \psi'(x) \, \mathrm{d}x. \tag{46}$$

This condition is also true in the finite element formalism because it directly follows from integration by parts after neglecting the non-integral summand. The term vanishes for periodic or Neumann boundary conditions.
This helps numerically because derivatives can be described as matrices. Those matrices are specific for the to be examined differential equation. The matrix which evaluates a function on finite elements is labeled as mass matrix M. K_x is the matrix that also evaluates the function on finite elements but also takes their derivative. Lastly the stiffness matrix K is taking additionally the second derivative. (see [43]).
The matrix structure can be calculated directly using the definition of for example the K matrix

$$K_{i,j} = \int \frac{\partial \varphi_i}{\partial x} \cdot \frac{\partial \varphi_j}{\partial x} \, \mathrm{d}x \tag{47}$$

[41], so using equation 45, it follows

$$(K \cdot u_h)_i = \int \frac{\partial \varphi_i}{\partial x} \cdot \sum_j \frac{\partial \varphi_j}{\partial x} \cdot c_j \, \mathrm{d}x \tag{48}$$

$$= \int \frac{\partial \varphi_i}{\partial x} \cdot \frac{\partial u_h}{\partial x} \, \mathrm{d}x. \tag{49}$$

To simply this term further, the more dimensional integration by parts rule must be used. For a subset $\Omega \subset \mathbb{R}^n$ with edge $\partial\Omega$ and orientation in normalized direction $\vec{n}$, as well as a continuously differentiable vector field $\vec{f}$ and a continuously differentiable scalar field g, the following relation is valid

$$\int_\Omega \vec{f}(\vec{x}) \cdot \vec{\nabla} g(\vec{x}) \, \mathrm{d}\vec{x} = \int_{\partial\Omega} \vec{f}(\vec{x}) \cdot g(\vec{x}) \cdot \vec{n} \, \mathrm{d}f - \int_\Omega \vec{\nabla} \vec{f}(\vec{x}) \cdot g(\vec{x}) \, \mathrm{d}\vec{x} \tag{50}$$

[44]. Using this formula (eq. 50) in equation 49, then it follows

$$(K \cdot \phi)_i = \int_\Omega \frac{\partial \varphi_i}{\partial x} \cdot \frac{\partial u_h}{\partial x} \, \mathrm{d}x \tag{51}$$

$$= \int_{\partial\Omega} \frac{\partial u_h}{\partial x} \cdot \varphi_i \cdot \vec{n} \, df - \int_\Omega \frac{\partial^2 u_h}{\partial x^2} \cdot \varphi_i \, \mathrm{d}x \tag{52}$$

$$= - \int_\Omega \frac{\partial^2 u_h}{\partial x^2} \cdot \varphi_i \, \mathrm{d}x, \tag{53}$$

The last line follows again by applying the boundary conditions.
So to summarize, with the finite element method and the weak formulation it is possible to derive substitution rules for the derivatives in differential equations. If a function ϕ needs to be evaluated on finite elements, it is possible with $M\phi$. The first or respectively the second derivative is evaluated on elements given by

$$\frac{\partial}{\partial x}\phi \qquad \Rightarrow \qquad K_x \phi \tag{54}$$

$$\frac{\partial^2}{\partial x^2}\phi \qquad \Rightarrow \qquad -K\phi. \tag{55}$$

For the stiffness matrix, an extra minus sign is present.
In summary, the finite element method is used to numerically evaluate an elliptic partial differential equation. The finite element method is a Galerkin method with a spatial choice of the subspace X_h of the Hilbert space X. It is built of test functions on a permissible triangulation of simplexes, which can mathematically describe the numerical solution u_h. The Galerkin method can be put in a matrix-vector form for a simple computation. The derivatives in the partial differential equation

are not disturbing, because they can also be written as matrices.
The next topic is the numerical error of this method. There are two different ways to state the error. There is an a priori and an a posteriori error. The first one is calculated before doing the numerical procedure and therefore gives a wider error range. In contrast the a posteriori error is calculating the error for the already determined u_h. Mathematically calculating both errors is quite hard, because a lot of steps must be taken from the Lemma of Cea over Interpolation error estimator to the Lemma of Aubin-Nitsche. For this reason, the numerical errors will just be stated here.
u is a solution of the elliptical partial differential equation and u_h is the solution of the corresponding finite element procedure. If $u \in H^{s+1}(\Omega)$ for a s in $1, ..., k$ with k being the polynomial degree of the functions defined by the finite element method, there is a constant c so that

$$\|u - u_h\|_{L^2(\Omega)} \leq ch^s \ |u|_{H^{s+1}(\Omega)}. \tag{56}$$

This formula can still be improved with a few assumptions using the Interpolation error estimator and the Lemma of Aubin-Nitsche. But this should be enough here. The space H^s is a typical space when talking about norms in numerics for partial differential equations. It is defined by

$$\|u\|_{H^s(\Omega)} = \left(\sum_{|\alpha| \leq m} \int_{\Omega} |\partial^\alpha u| \right)^{\frac{1}{2}} \tag{57}$$

[41]. The a posteriori error is based on the residuum. For a equation $\frac{\partial u}{\partial x} = f(u)$ it yields

$$R(u_h) = \frac{\partial u}{\partial x} - f(u) \tag{58}$$

It expresses how good the partial differential equation is fulfilled and therefore also how exact the approximation u_h is. The solution is exact if the residuum is zero. Using this definition, it is possible to derive the lower bound for the residuum in the form of

$$|R(u_h)|_{H^{-1}(\Omega)} \leq c \cdot \eta_h(u_h) \tag{59}$$

with

$$\eta_h(u_h) = \sum_{T \in \tau_h} \left(h(T)^2 |f + \Delta u_h|^2_{L^2(\Omega)} + \frac{1}{2} h(T) \sum_{S \in \partial T \ \partial\Omega} |\nabla u_h \cdot \vec{n}|^2_{L^2(S)} \right)^{\frac{1}{2}}. \tag{60}$$

4.2.2 Pde2path - A matlab package for Continuation

Pde2path is a matlab package, which is used for Continuation and Bifurcation analysis [19]. Throughout this work the 2.9 version [45] is used. It is an upgrade to the original version with new features like fold continuation or easier use of auxiliary equations. Here is shown just a simplified explanation of the functionality. To get a better overview, see [19], or [46] and the mathematical concepts behind it, see for example [47] or [48].
Pde2path treats a partial differential equation in the general form

$$G(u,\lambda) := -\nabla\cdot(c\otimes\nabla u) + au - b\otimes\nabla u - f = 0 \tag{61}$$

[19] with $x \in \Omega$, where Ω is the domain, where the function $u(x) \in \mathbb{R}^n$ is defined. λ is the continuation parameter (vector). a, b, c and f are functions depending on $x, u, \nabla u$ and parameters.

4.2.2.1 Continuation of solution branches

The goal of a continuation algorithm is to follow a stationary solution of a partial differential equation in phase space under the variation of a control parameter. Throughout this also the stability should be examined, to be able to detect bifurcation points and follow new solution branches. In this paragraph, the basic ideas of the continuation of solution branches will be explained. It consists in general of two steps, which will be illustrated using the following figure 29.

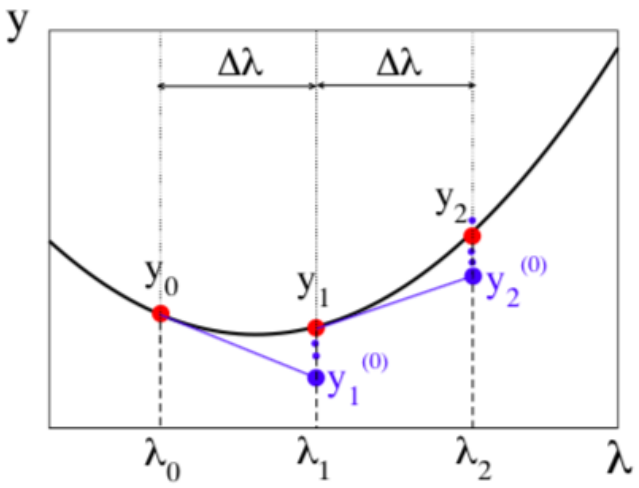

Figure 29: In this sketch of the functionalty of continuation the stationary solution y is shown in phase space. It is calculated numerically at different control parameter values of λ [49].

In figure 29 the solution y is shown in phase space. A measure to show the solution on the one-dimensional ordinate. On the abscissa, the control parameter λ is shown. The solution is approximated at λ_i with $i \in \mathbb{N}_0$ in a distance $\Delta\lambda$. At those positions the stationary solution has the value z_i with $i \in \mathbb{N}_0$. The algorithm starts at a known solution y_0, which comes from the direct

numerics or might be calculated directly. In the first step a predictor $y_1^{(0)}$ for the solution y_1 at λ_1 is assumed. It corresponds to the functional value at position λ_1 of the tangent in phase space at point y_0. The second step consists of using Newton's method to iterate to the actual solution y_1 until a threshold is reached. Then the solution y_1 at position λ_i is known approximately. To get more points, repeat the above steps: Use a predictor with the tangent and then calculate the solution with Newton's method.
The Newton method is a numerical method, which is used to approximate the zero values of a function. To approximate them for a one dimensional function $f(x)$, the procedure is as follows: Choose a starting position x_0 with $f'(x_0) \neq 0$ and then calculate the intersection position x_1 of the tangent at x_0 with the x-axis. It yields $x_1 = x_0 + \Delta x$ with an unknown distance Δx. To calculate it, a Taylor series of $f(x_0 + \Delta x)$ is performed

$$f(x_1) = f(x_0 + \Delta x) \approx f(x_0) + f'(x_0) \cdot \Delta x \stackrel{!}{=} 0 \tag{62}$$

and this is then set to zero because a zero value is searched for. Now the formula is rearranged to get the distance δx to get:

$$\Delta x = -\frac{f(x_0)}{f'(x_0)}. \tag{63}$$

All in all, there is an iterative formula to get the zero values of a function f:

$$x_i = x_{i-1} - \frac{f(x_{i-1})}{f'(x_{i-1})} \qquad \Leftrightarrow \qquad f'(x_{i-1}) \cdot \Delta x_i = f(x_{i-1}), \tag{64}$$

with $\Delta x_i = x_i - x_{i-1}$ (see [50]). To be able to apply that for the more dimensional system in pde2path, like

$$\frac{\partial \vec{y}}{\partial t} = \vec{G}(\vec{y}, \lambda), \tag{65}$$

a more dimensional equivalent of the Newton's method is needed. By analogy, it follows:

$$\vec{G}_{\vec{y}}(\vec{y}^{(i)}, \lambda) \cdot \Delta \vec{y}^{(i)} = \vec{G}(\vec{y}^{(i)}, \lambda), \tag{66}$$

whereby $\vec{G}_{\vec{y}}(\vec{y}^{(i)}, \lambda)$ is the Jacobian of $\vec{G}$

$$\vec{G}_{\vec{y}}(\vec{y}^{(i)}, \lambda) = \begin{pmatrix} \frac{\partial G_1}{\partial y_1} & \frac{\partial G_1}{\partial y_2} & \dots & \frac{\partial G_1}{\partial y_n} \\ \frac{\partial G_2}{\partial y_1} & \ddots & & \vdots \\ \vdots & & \ddots & \vdots \\ \frac{\partial G_n}{\partial y_1} & \dots & \dots & \frac{\partial G_n}{\partial y_n} \end{pmatrix}. \tag{67}$$

With the Newton method it is now possible to get from a starting value $y_i^{(0)}$ to a solution y_i. Next up is to get the tangent to make a predictor $y_i^{(0)}$. Therefore the tangent direction $\frac{\partial \vec{y}}{\partial \lambda}$ needs to be calculated. By applying the partial derivate with respect to λ and taking into account the chain rule of the function $\vec{G}(\vec{y}, \lambda)$, it gives

$$\frac{\partial \vec{G}}{\partial \vec{y}} \cdot \frac{\partial \vec{y}}{\partial \lambda} + \frac{\partial \vec{G}}{\partial \lambda} = 0, \tag{68}$$

whereby $\frac{\partial \vec{G}}{\partial \vec{y}}$ is the Jacobian after equation (67). Therefore there is a system of equations

$$\vec{G}_{\vec{y}} \cdot \frac{\partial \vec{y}}{\partial \lambda} = -\frac{\partial \vec{G}}{\partial \lambda}, \tag{69}$$

which can be used to derive the searched for tangent direction $\frac{\partial \vec{y}}{\partial \lambda}$. In general the predictor $y_{j+1}^{(0)}$ starting from y_j is given by

$$y_{j+1}^{(0)} = y_j + \Delta\lambda \cdot \frac{\partial \vec{y}}{\partial \lambda}. \tag{70}$$

After that basic explanation of the used mathematical methods, here is a short overview of how this is applied in the more complex setting of pde2path while using the finite element method (For a detailed explanation, see [19]).
Consider a branch $s \to z(s) := (u(s), (\lambda(s))$ of steady solutions of equation 65 and setup the system

$$H(u, \lambda) := \begin{pmatrix} G(u, \lambda) \\ p(u, \lambda, s) \end{pmatrix} = 0 \tag{71}$$

[46]. Here p is used to make the parametrization s to an approximation to the arclength of the solution branch [46]. Then the tangent vector τ_0 at a given point $(u_0, \lambda_0) := (u(s_0), \lambda(s_0))$ is set to $\tau_0 := (u_0', \lambda_0') := \frac{\mathrm{d}}{\mathrm{d}s}(u(s), \lambda(s))\big|_{s=s_0}$ [46]. It follows:

$$p(u, \lambda, s) := \xi \left\langle u_0', u(s) - u_0 \right\rangle + (1 - \xi) \left\langle \lambda_0', \lambda(s) - \lambda_0 \right\rangle - (s - s_0) \tag{72}$$

[46]. Using this definitions, the predictor is given by $(u^1, \lambda^1) = (u_0, \lambda_0) + (s - s_0)\tau_0$ and the corrector using Newton's method is in the form:

$$\begin{pmatrix} u^{j+1} \\ \lambda^{j+1} \end{pmatrix} = \begin{pmatrix} u^j \\ \lambda^j \end{pmatrix} - A(u^j, \lambda^j)^{-1} H(u^j, \lambda^j) \tag{73}$$

with

$$A = \begin{pmatrix} G_u & G_\lambda \\ \xi u_0' & (1 - \xi)\lambda_0' \end{pmatrix} \tag{74}$$

[46].

4.2.2.2 Detecting Bifurcations

As described before in the chapter 2.3 „Bifurcations“, at bifurcation points there is a change in stability of the solution. This results in eigenvalues of the Jacobian G_u crossing the imaginary axis. To determine the type of bifurcation there needs to be additional information, but the key to detecting bifurcations is to detect eigenvalues changing sign. There are mainly two different methods to use:
The first method is to look for sign changes on the determinant of G_u (or more generally A). The determinant is connected to a multiplication of all eigenvalues using matrix similarity. So if an eigenvalue changes sign, it is seen in a sign change of the determinant, which corresponds to some sort of bifurcation taking place. A big problem of this approach is therefore also clear: If two eigenvalues change sign at the same time due to a too large step size or due to a hopf bifurcation taking place, the determinant does not change sign. That results in no detection of a bifurcation, even if there is one. In general, no hopf bifurcations can be observed with this algorithm.
That problem is not appearing in the second method. Here a chosen number of eigenvalues of G_u (or in general A) are calculated numerically. This is numerically much more demanding and takes more time in each continuation step. So it is useful to only compute a few eigenvalues near the imaginary axis. It works well if just a few eigenvalues are near zero but if not the number of calculated eigenvalues might be too low and therefore bifurcations can be undetected.
Due to the fact, that hopf bifurcations are expected because there are time dependant solutions like in [7] or [11], the second method will be used.

4.2.2.3 Phase shift symmetry and translation invariance

The complex quintic-cubic Ginzburg-Landau equation has two invariants, the phase shift symmetry, and translation invariance. For translation invariance, it means if a solution profile $A(t)$ is shifted to the side by δt, resulting in $A(t+\delta t)$, it also stays a solution of the problem. The same is the case if a phase shift is present. Such a shift can occur due to for example numerical errors, which results in a detection of a bifurcation point, even if the same solution with the same eigenvalue is observed. To avoid this behaviour an additional constraint for both invariants must be added. In the following paragraph, it is shown how the constraints need to look like.
Starting again with the translation invariance, where a new solution $\tilde{A}(t) = A(t+\delta t)$ is a shift of the old solution $A(t)$ by a small $\delta t \ll 1$. To gain a mathematical condition, so that it does not result in a bifurcation, the Taylor series for $\delta t \ll 1$ must be calculated:

$$A(t+\delta t) \approx A(t) + \frac{\partial A}{\partial t} \cdot (t+\delta t-t) + \frac{1}{2}\frac{\partial^2 A}{\partial t^2} \cdot (t+\delta t-t)^2 \tag{75}$$

By simplifying the equation 75 and neglecting nonlinear orders in t, it looks like

$$A(t+\delta t) \approx A(t) + \frac{\partial A}{\partial t} \cdot \delta t, \tag{76}$$

which is equivalent to

$$A(t+\delta t) - A(t) = \frac{\partial A}{\partial t} \cdot \delta t. \tag{77}$$

This equation 77 states that the difference between old and new solution ΔA is proportional to the derivative $\frac{\partial A}{\partial t}$. To prevent the detection of the new solution, this proportionality must not occur. Nonproportionality in functional space means that both functions must be orthogonal to each other, so their scalar product is equal to zero. The following constraint in equation 78 does exactly that:

$$\Delta A \cdot \frac{\partial A}{\partial t} \stackrel{!}{=} 0. \tag{78}$$

Next up is the analogous derivation of the constraint for the phase shift symmetry. The scalar product of the phase derivative with the difference between new and old solution must be zero:

$$\Delta A \cdot \frac{\partial A}{\partial \phi} \stackrel{!}{=} 0. \tag{79}$$

The concrete implementation of both constraints is explained in the section 4.2.3.3 „Additional constraints“.

4.2.3 Implementation of the Ginzburg-Landau equation

In this section, the continuation formalism will be applied for the cubic-quintic complex Ginzburg-Landau equation (equation 20). The basics of the numerical continuation are defined in a file called gl1d_init.m, like the parameters, boundary conditions, control parameter, or grid size. The output of the continuation like the measure can be changed in gl1d_bra.m.

4.2.3.1 Stationary solutions and a system of real equations

For the continuation the Ginzburg-Landau equation needs to be simplified and rewritten, which consists of two steps: Firstly we search for stationary, localized solutions of equation 20, like in the direct numerics results depicted in section 3.3 „Different solutions of the Ginzburg-Landau equation“. That simplifies the equation and needs to be implemented. Secondly, the still complex equation must be rearranged as a system of two real equations to be able to use the continuation formalism.
To start the Ginzburg-Landau equation can be written as (see eq. 21)

$$\frac{\partial A}{\partial z} = \left(\beta + \frac{D}{2}\mathrm{i}\right)\frac{\partial^2 A}{\partial t^2} + \delta A + (\varepsilon + \mathrm{i})\,|A|^2 A + (\mu + \nu\mathrm{i})\,|A|^4 A$$

using basic equivalent conversion. In this form, the order of magnitudes and of derivatives of the field $A(t,z)$ can be seen easier. This is useful in the first step, where the goal is to get stationary, localized solutions. To get this type of solution the following ansatz

$$A(t,z) = A(t - vz) \cdot \mathrm{e}^{-\mathrm{i}\omega z} \tag{80}$$

is used. Here v is the propagation speed and ω is a spectral parameter. This ansatz in equation 80 now needs to be inserted into equation 21. Therefore the second derivative with respect to t and the first derivative with respect to z need to be calculated. Looking first at the t derivatives, using the chain rule, they can be written as:

$$\frac{\partial A(t,z)}{\partial t} = \frac{\partial A(t-vz)}{\partial t} \cdot \mathrm{e}^{-\mathrm{i}\omega z} = \frac{\partial A(t-vz)}{\partial (t-vz)} \cdot \frac{\partial (t-vz)}{\partial t} \cdot \mathrm{e}^{-\mathrm{i}\omega z} = \frac{\partial A(t-vz)}{\partial (t-vz)} \cdot \mathrm{e}^{-\mathrm{i}\omega z} \tag{81}$$

and by analogy, it follows

$$\frac{\partial^2 A(t,z)}{\partial t^2} = \frac{\partial^2 A(t-vz)}{\partial (t-vz)^2} \cdot \mathrm{e}^{-\mathrm{i}\omega z}. \tag{82}$$

Using the product rule, the partial derivative with respect to z gives:

$$\frac{\partial A(t,z)}{\partial z} = -\mathrm{i}\omega A(t-vz) \cdot \mathrm{e}^{-\mathrm{i}\omega z} + \frac{\partial A(t-vz)}{\partial z} \cdot \mathrm{e}^{-\mathrm{i}\omega z}. \tag{83}$$

Due to the following relation

$$\frac{\partial A(t-vz)}{\partial z} = \frac{\partial A(t-vz)}{\partial (t-vz)} \cdot \frac{\partial (t-vz)}{\partial z} = -v \cdot \frac{\partial A(t-vz)}{\partial (t-vz)}, \tag{84}$$

equation 83 can be simplified to

$$\frac{\partial A(t,z)}{\partial z} = \left(-v \frac{\partial}{\partial (t-vz)} - \mathrm{i}\omega \right) A(t-vz) \cdot \mathrm{e}^{-\mathrm{i}\omega z} \tag{85}$$

By defining $\tilde{t} = t - vz$, dropping the tilde and inserting the ansatz (eq. 80) into equation 21 with the calculated derivates in equation 82 and 85, it yields to

$$0 = \left(\beta + \frac{D}{2}\mathrm{i} \right) \frac{\partial^2 A}{\partial t^2} + v \frac{\partial A}{\partial t} + (\delta + \omega \mathrm{i}) A \cdot \mathrm{e}^{-\mathrm{i}\omega z} + (\varepsilon + \mathrm{i}) \left| A \cdot \mathrm{e}^{-\mathrm{i}\omega z} \right|^2 \cdot \mathrm{e}^{-\mathrm{i}\omega z} + (\mu + \nu \mathrm{i}) \left| A \cdot \mathrm{e}^{-\mathrm{i}\omega z} \right|^4 \cdot \mathrm{e}^{-\mathrm{i}\omega z}. \tag{86}$$

Using also the relation

$$\left| \mathrm{e}^{-\mathrm{i}\omega z} \right|^2 = 1 \tag{87}$$

and dividing by $\mathrm{e}^{-\mathrm{i}\omega z}$, the equation is finally simplified to

$$0 = \left(\beta + \frac{D}{2}\mathrm{i} \right) \frac{\partial^2 A}{\partial t^2} + v \frac{\partial A}{\partial t} + (\delta + \omega \mathrm{i}) A + (\varepsilon + \mathrm{i}) |A|^2 A + (\mu + \nu \mathrm{i}) |A|^4 A. \tag{88}$$

Now the second part, where next the equation needs to be rewritten as a system of real equations,

can be done. To get this the complex equation is split into the real and imaginary part. This is done by composing the function A out of a real a_1 and an imaginary function a_2:

$$A = a_1 + \mathrm{i}a_2 \tag{89}$$

The ansatz is inserted into the equation 88

$$\begin{aligned} 0 = \quad & \left(\beta + \frac{D}{2}\mathrm{i}\right)\frac{\partial^2(a_1+\mathrm{i}a_2)}{\partial t^2} + v\frac{\partial(a_1+\mathrm{i}a_2)}{\partial t} + (\delta+\omega\mathrm{i})(a_1+\mathrm{i}a_2) \\ & +(\varepsilon+\mathrm{i})\left|a_1+\mathrm{i}a_2\right|^2(a_1+\mathrm{i}a_2) + (\mu+\nu\mathrm{i})\left|a_1+\mathrm{i}a_2\right|^4(a_1+\mathrm{i}a_2) \end{aligned}$$

and in the next step the terms must be sorted:

$$\begin{aligned} 0 = & \frac{\partial^2}{\partial t^2}\left[\left(\beta a_1 - \frac{D}{2}a_2\right) + \mathrm{i}\left(\frac{D}{2}a_1 + \beta a_2\right)\right] + \frac{\partial}{\partial t}(va_1 + va_2) \\ & + \left[\delta a_1 - \omega a_2) + \mathrm{i}(\omega a_1 - \delta a_2)\right] + \left[(\varepsilon a_1 - a_2) + \mathrm{i}(a_1 + \varepsilon a_2)\right](a_1^2 + a_2^2) \\ & + \left[(\mu a_1 - \nu a_2) + \mathrm{i}(\nu a_1 + \mu a_2)\right](a_1^2 + a_2^2)^2. \end{aligned} \tag{90}$$

Then it can now be split into two equations because the whole equation must be true for on the one hand the real and on the other hand for the imaginary part. That results in a system of two real equations, as it was searched for

$$\begin{aligned} \text{Re)} \quad 0 &= \frac{\partial^2}{\partial t^2}\left(\beta a_1 - \frac{D}{2}a_2\right) + \frac{\partial}{\partial t}va_1 + (\delta a_1 - \omega a_2) + (\varepsilon a_1 - a_2)\left|A\right|^2 + (\mu a_1 - \nu a_2)\left|A\right|^4 \\ \text{Im)} \quad 0 &= \frac{\partial^2}{\partial t^2}\left(\frac{D}{2}a_1 + \beta a_2\right) + \frac{\partial}{\partial t}va_2 + (\omega a_1 - \delta a_2) + (a_1 + \varepsilon a_2)\left|A\right|^2 + (\nu a_1 + \mu a_2)\left|A\right|^4 \end{aligned} \tag{91}$$

using $|A|^2 = a_1^2 + a_2^2$. The implementation of this system of equations in pde2path is done in the form of equation 61, which can be simplified to

$$\text{rhs} = -(-\underline{\underline{K}} \cdot \vec{A} + \underline{\underline{K_x}} \cdot \vec{A} + \underline{\underline{M}} \cdot \vec{F}) \tag{92}$$

with

$$\vec{A} = \begin{pmatrix} a_1 \\ a_2 \end{pmatrix} \tag{93}$$

$$\underline{\underline{K}} = \begin{pmatrix} \beta \cdot K & -\frac{D}{2}K \\ \frac{D}{2}K & \beta K \end{pmatrix} \tag{94}$$

$$\underline{\underline{M}} = \begin{pmatrix} M & 0 \cdot M \\ 0 \cdot M & M \end{pmatrix} \tag{95}$$

$$\underline{\underline{K_x}} = \begin{pmatrix} v \cdot K_x & 0 \cdot K_x \\ 0 \cdot K_x & v \cdot K_x \end{pmatrix} \tag{96}$$

$$\vec{F} = \begin{pmatrix} (\delta a_1 - \omega a_2) + (\varepsilon a_1 - a_2)(a_1^2 + a_2^2) + (\mu a_1 - \nu a_2)(a_1^2 + a_2^2)^2 \\ (\omega a_1 - \delta a_2) + (a_1 + \varepsilon a_2)(a_1^2 + a_2^2) + (\nu a_1 + \mu a_2)(a_1^2 + a_2^2)^2 \end{pmatrix}. \tag{97}$$

Equation 92 with the abbreviations 97 is implemented in the file gl1d_sg.m.

4.2.3.2 Jacobian and Fold continuation

For the numerical evaluation in pde2path the Jacobian for the to be examined equation is needed (see equation 67 or 73). To calculate them the derivatives with respect to a_1 and a_2 of the system of equations in equation 91 are needed:

$$\begin{aligned}
\frac{\partial \mathrm{Re}}{\partial a_1} &= 4\nu a_1^4 + 6\nu a_1^2 a_2^2 + \nu a_2^4 + 4\mu a_1^3 a_2 + 4\mu a_1 a_2^3 \\
\frac{\partial \mathrm{Re}}{\partial a_2} &= 4\nu a_1^3 a_2 + 4\nu a_1 a_2^3 + \mu a_1^4 + 6\mu a_1^2 a_2^2 + 5\mu a_2^4 \\
\frac{\partial \mathrm{Im}}{\partial a_1} &= 5\mu a_1^4 + 6\mu a_1^2 a_2^2 + \mu a_2^4 - 4\nu a_2 a_1^3 - 4\nu a_1 a_2^3 \\
\frac{\partial \mathrm{Im}}{\partial a_2} &= 4\nu a_1^3 a_2 + 4\mu a_1 a_2^3 - \nu a_1^4 - 6\nu a_1^2 a_2^2 - 5\nu a_2^4
\end{aligned} \tag{98}$$

Together with the additional constraints q_1 and q_2 corresponding to phase shift symmetry and translation invariance (see section 4.2.2.3 „Phase shift symmetry and translation invariance“), the Jacobian becomes:

$$J = \begin{pmatrix} \frac{\partial \mathrm{Re}}{\partial a_1} & \frac{\partial \mathrm{Re}}{\partial a_2} \\ \frac{\partial \mathrm{Im}}{\partial a_1} & \frac{\partial \mathrm{Im}}{\partial a_2} \end{pmatrix} \tag{99}$$

and is implemented in gl1d_sGjac.m.
Together with the additional constraints q_1 and q_2 corresponding to phase shift symmetry and translation invariance and the resulting Lagrange parameters, namely the propagation speed v and the spectral parameter ω, there is an extended system, where the Jacobian becomes

$$J = \begin{pmatrix} \frac{\partial \mathrm{Re}}{\partial a_1} & \frac{\partial \mathrm{Re}}{\partial a_2} & \frac{\partial \mathrm{Re}}{\partial \omega} & \frac{\partial \mathrm{Re}}{\partial v} \\ \frac{\partial \mathrm{Im}}{\partial a_1} & \frac{\partial \mathrm{Im}}{\partial a_2} & \frac{\partial \mathrm{Im}}{\partial \omega} & \frac{\partial \mathrm{Im}}{\partial v} \\ \frac{\partial q_1}{\partial a_1} & \frac{\partial q_1}{\partial a_2} & \frac{\partial q_1}{\partial \omega} & \frac{\partial q_1}{\partial v} \\ \frac{\partial q_2}{\partial a_1} & \frac{\partial q_2}{\partial a_2} & \frac{\partial q_2}{\partial \omega} & \frac{\partial q_2}{\partial v} \end{pmatrix}. \tag{100}$$

The derivatives of the constraints are calculated in gl1d_qfjac.m.
For a fold continuation the derivative $\partial_u(\partial_u G\phi)$ needs to be calculated using the pde2path parameter definition (see equation 61) [45]. This implementation in simplified nodal finite element method format allows for more efficient calculation in contrast to otherwise used finite differences. $\partial_u(\partial_u G\phi)$ is given by:

$$\partial_u(\partial_u G\phi) = \begin{pmatrix} (\partial_{u_1}^2 f_1)\phi_1 + (\partial_{u_1}\partial_{u_2} f_1)\phi_2 & (\partial_{u_1}\partial_{u_2} f_1)\phi_1 + (\partial_{u_1}^2 f_1)\phi_2 \\ (\partial_{u_1}^2 f_2)\phi_1 + (\partial_{u_1}\partial_{u_2} f_2)\phi_2 & (\partial_{u_1}\partial_{u_2} f_2)\phi_1 + (\partial_{u_1}^2 f_2)\phi_2 \end{pmatrix} \tag{101}$$

with $u = (u_1, u_2)$, $\vec{F} = (f_1, f_2)$ and $\phi = (\phi_1, \phi_2)$ [45] and implemented in gl1d_spjac.m.

4.2.3.3 Additional constraints

Next up is the implementation of the two additional constraints given by equation 78 and 79. An explanation of the derivation is given in the associated section. Using the pde2path formalism both equations are implemented in the file called gl1d_qf.m.
First the implementation of phase shift symmetry given by equation 79

$$\Delta A \cdot \frac{\partial A}{\partial \phi} \stackrel{!}{=} 0.$$

The complex field $A(t,z) = a_0 \cdot e^{i\phi}$ can be split into a real a_1 and an imaginary part a_2 (like in equation 89), which yields in vectorial form $A = (a_1, a_2)$. The phase derivative is then given by

$$\frac{\partial A}{\partial \phi} = i a_0 \cdot e^{i\phi} = (-a_2, a_1), \tag{102}$$

where the last expression is again written in vectorial form. Setting this into the scalar product equation 79 results in

$$\begin{aligned} & \begin{pmatrix} a_{1,\text{new}} - a_{1,\text{old}} \\ a_{2,\text{new}} - a_{2,\text{old}} \end{pmatrix} \cdot \begin{pmatrix} -a_{2,\text{old}} \\ a_{1,\text{old}} \end{pmatrix} \stackrel{!}{=} 0 \\ \Leftrightarrow \quad & q_1 := a_{1,\text{old}}(a_{2,\text{new}} - a_{2,\text{old}}) - a_{2,\text{old}}(a_{1,\text{new}} - a_{1,\text{old}}) \stackrel{!}{=} 0. \end{aligned} \tag{103}$$

This equation is directly implemented in matlab, which is shown in the following program code.

```
1 u1 = u(1:p.nu/2);
2 u2 = u(p.nu/2+1:p.nu);
3
4 u1o = p.u(1:p.nu/2);
5 u2o = p.u(p.nu/2+1:p.nu);
6
7 % new implementation: <uold_phase', u>=0, u_phase=iu
8 q1 = +u1o'*(u2-u2o) -u2o'*(u1-u1o);
```

In the first 5 lines, the fields a_1 and a_2 are in defined in both old and new form. Herefore they are renames form a to u. Afterwards in line 8 equation 103 is implemented.
The second constraint (equation 78) is given by the translational invariance

$$\Delta A \cdot \frac{\partial A}{\partial t} \stackrel{!}{=} 0.$$

The derivative $\frac{\partial A}{\partial t}$ is numerically given by the matrix K_x using the finite element method (see equation 55). ΔA is again given by the difference between old in new field like in equation 103. The equation 78 therefore turns into

$$q_2 := K_x \cdot \begin{pmatrix} a_{1,\text{old}} \\ a_{2,\text{old}} \end{pmatrix} \cdot \begin{pmatrix} a_{1,\text{new}} - a_{1,\text{old}} \\ a_{2,\text{new}} - a_{2,\text{old}} \end{pmatrix} \stackrel{!}{=} 0 \tag{104}$$

Here no further simplifications are needed because both vectors can be implemented directly, as shown below.

```
9  uoz = p.mat.Kz0*p.u(1:p.nu);
10
11 % phase condition in periodic case: <uold',u>=0
12 q2= uoz(1:p.nu)'*(u(1:p.nu)-p.u(1:p.nu));
```

The derivative is defined in line 9 and the translation-invariant constraint is implemented in line 12.

5 Results

First, the evaluation of the dynamics of localized states for passively mode-locked lasers is discussed. The results on the topic of soliton resonance are presented afterwards.

5.1 Dynamics of localized states

The goal of this analysis is to gain a better understanding of the dynamics of the localized states described in section 3.3 „Different solutions of the Ginzburg-Landau equation“ within the topic of mode-locked lasers. Using numerical continuation, bifurcation diagrams are produced to connect the different types of solutions.

5.1.1 First steps and solution measure

There are a lot of different ideas to start this topic for example the dynamics of the exploding solitons or creeping solitons. While a basic analysis for soliton explosions has been done (see [12]), the starting point of this analysis is the pulsating solution as described before using figure 16. Firstly, an initial solution using the direct numerical method has to be generated in order to start the continuation process and to generate a bifurcation diagram. For a detailed explanation of the used programs for continuation, see section 4.2 „Continuation approach“ and for the direct method, see section 4.1 „Direct numerical method“.
The same parameters, namely $\delta = -0.1$, $\beta = 0.08$, $\mu = -0.1$, $\nu = -0.1$, $D = 1$ and $\varepsilon = 0.66$, are used as in [7], on a domain given by $L = [-40, 40]$. The numerical simulation is done for 100 dimensionless time steps (corresponding to the coordinate z) with a step size of $h = 0.00025$ and 2048 grid points for the spacial coordinate t. As the initial value function a Gauß like function

$$A(t, z = 0) = 1.5 \cdot \mathrm{e}^{-\frac{t^2}{10}} \tag{105}$$

is used. The following figure 30 shows the direct numerical results.

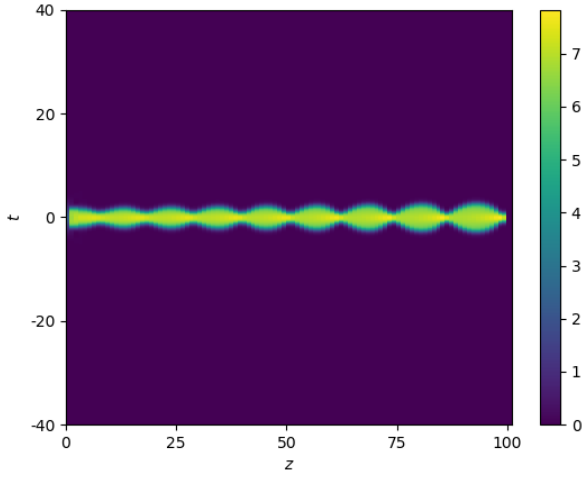

Figure 30: Direct numerical simulation of a pulsating solution for the system parameters: $\delta = -0.1$, $\beta = 0.08$, $\mu = -0.1$, $\nu = -0.1$, $D = 1$ and $\varepsilon = 0.66$.

In figure 30 one can see that after a short settling phase a periodic pulsating solution is built which is stable over time even if the stabilizing process is probably not finished yet. Thus the results of [7] are reproduced. The pulsating soliton solution is time-dependent which excludes it for inputting it as an initial solution into the continuation algorithm. A small adjustment is needed to nevertheless investigate pulsating solitons without using them directly. To gain a stable stationary solution within this parameter regime it is useful to change the control parameter until the pulsating solution becomes unstable and a stationary solution is stable and then simply start the simulation at the parameter value of the new parameter. The control parameter, in this case, is the gain (or loss) parameter δ. For $\delta = -0.2$ and all other parameters unchanged a stable stationary solution can be found via direct numerics, as shown in figure 31.

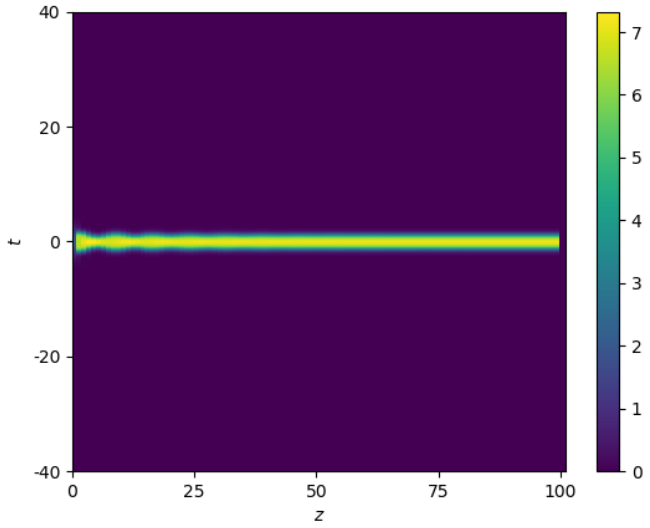

Figure 31: Direct numerical simulation of a stationary solution for the system parameters: $\delta = -0.2$, $\beta = 0.08$, $\mu = -0.1$, $\nu = -0.1$, $D = 1$ and $\varepsilon = 0.66$.

Here, in figure 31, for the first about ten time steps, the remainder of a pulsation fades away until a stationary solution is stabilized. After the total simulation time, no change with time can be seen on the shown scale. The profile at that last step is now exported so that it can be implemented as an initial solution for the continuation. Here, periodic boundary conditions are applied and the maximum intensity of a pulse profile $A(t)$

$$|A|^2_{\max} = \frac{1}{\tilde{L}} \max_{t \epsilon L} \{|A(t)|^2\} \tag{106}$$

is used as a measure in the bifurcation diagram with $\tilde{L}$ being total the domain length of the domain L, as in [12]. In the following figure 32 the resulting bifurcation diagram is shown.

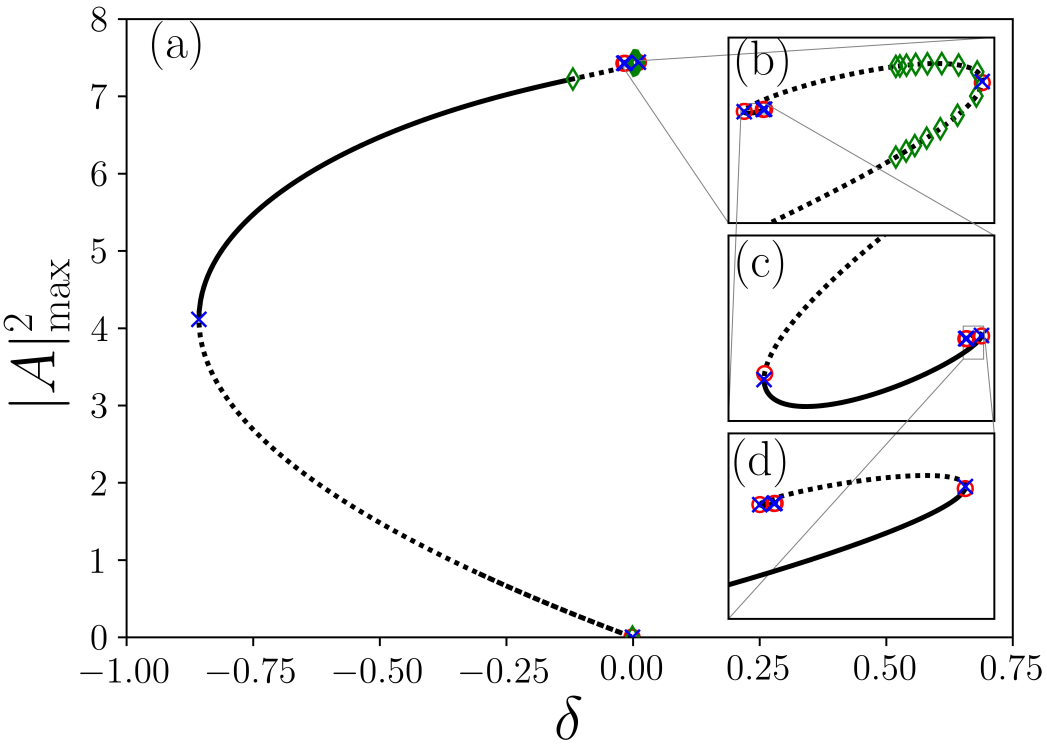

Figure 32: Bifurcation diagram for $A_{\max}$ against the gain or loss parameter δ for the system parameters: $\beta = 0.08$, $\mu = -0.1$, $\nu = -0.1$, $D = 1$ and $\varepsilon = 0.66$. Red circle corresponds to a pitchfork bifurcation, blue cross to a fold point and green rhombus to a hopf bifurcation.

One can see in figure 32 that the localized solution branch emerges subcritical from a homogeneous zero state and is then stabilized by a fold point. Afterwards, the soliton grows in maximum intensity until a hopf bifurcation occurs which destabilizes the branch again. Then a lot of bifurcation points are stacked on top of each other in the shown scale. In the zoomed-in diagrams, it can be seen that the solution changes stability multiple times while spiraling into a smaller spiral. The simulation ends after a few spirals due to numerical dependencies (values can not be distinguished within the machine precision), so it is not clear if the spiral continues indefinitely or if it ends at some point and is building a new structure.
Nevertheless, the spiral prevents the view of the entire content of the bifurcation diagram and therefore multiple zooms are needed. To alleviate this problem the measure for the graphical depiction is changed. The new one is given by the total intensity of the pulse $|A|^2_{\text{int}}$

$$|A|^2_{\text{int}} = \frac{1}{\tilde{L}} \int_{t \epsilon L} |A(t)|^2 \, \mathrm{d}t \tag{107}$$

and is proportional to the energy Q in a variety of resources dealing with soliton resonance (see for example [15], [16] or [18]). Figure 33 shows the results with the new measure $|A|^2_{\text{int}}$. In figure

33a a few positions along the bifurcation diagram are highlighted. The corresponding profiles of the solutions is shown in figure 33b.

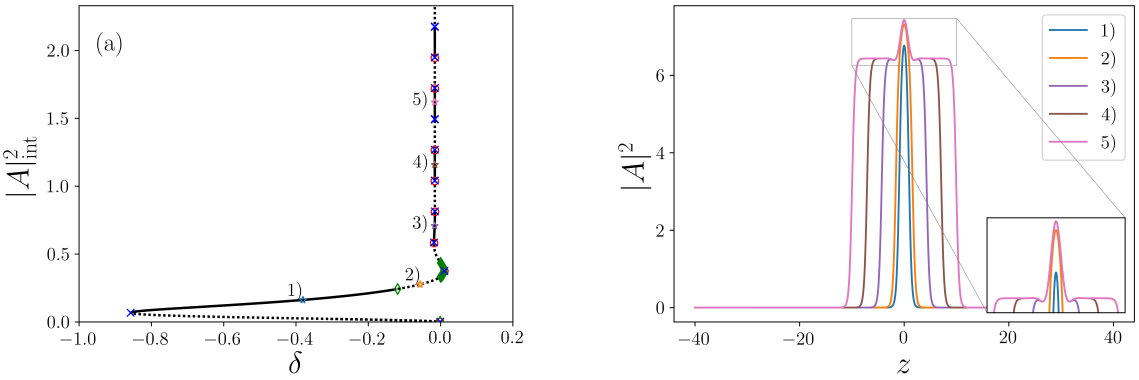

(a) Bifurcation diagram

(b) solution profile

Figure 33: a) Bifurcation diagram of figure 32 with a different measure $|A|^2_{\text{int}}$ and coloured positions which are indicated with stars. The corresponding solution profile is shown in figure b) for the different positions. System parameters: $\beta = 0.08$, $\mu = -0.1$, $\nu = -0.1$, $D = 1$ and $\varepsilon = 0.66$.

In the subdiagram 33a the bifurcation diagram in figure 32 is shown with the changed measure $|A|^2_{\text{int}}$ which is given by equation 107. If one follows the solution branch along at the beginning it looks similar to the one with maximum intensity $|A|^2_{\text{max}}$ as the measure: It still emerges subcritical from a homogeneous zero state, stabilized with a fold point, and undergoes a destabilizing hopf bifurcation until the solution behaviour of the spiral in diagram 32 is shown more clearly without the need for zooming. A similar appearance is to be expected because there was just a change of the type of representation and the physical meaning stays the same.
Looking at the behaviour previously hidden within the spiral, one can see that a lot of hopf bifurcations occur for positive δ. This results from an unstable global bifurcation which acts like a constant noise destabilizing the soliton solution. This fits with the narrative that no stable solitons exist for $\delta > 0$. Within this regime of hopf bifurcations there exists a pitchfork bifurcation and a fold point which directs the solution branch again towards the energy loss regime ($\delta < 0$). After a lot of stabilizing hopf bifurcations, the soliton branch rises in energy while periodically changing stability. There is always a stabilizing pitchfork bifurcation followed by a stabilizing fold point which results in a stable regime of the soliton branch that ends with a destabilizing pitchfork bifurcation and a fold so that there are two unstable eigenvalues. This pattern repeats itself four times until the numerical simulation stops due to numerical dependencies. As a result, there is multistability.
In figure 33b the solution profile of the marked spots in figure 33a are shown. Without looking at them it is unclear what structural change occurs at bifurcation points or in general when changing the parameter δ. Starting in the blue marked position number one there is just a plain pulse, which grows with the decrease of the absolute value of δ as seen in the profile of the green marked position. After the regime of positive δ the stable soliton solutions are composite pulses (see marked positions number three to five) which grow in width when following along the soliton

branch. Also, the previously unstable plain pulse solution can be seen as part of the solution profile when comparing the marked profiles two and three.
There is a lot that needs to be discussed within the framework of this bifurcation diagram. For example what kind of solutions emerge from the different pitchfork bifurcations or the hopf-bifurcation and where the initial pulsating soliton solution can be found. A more detailed overview will be given in the following sections. But first of all the question from earlier remains and needs to be answered first: What happens if the branch is followed further along? In figure 33b one can see that the width of the pulse grows along with the energy. Therefore an interesting point occurs when the pulse width is the same length as the whole domain. Due to numerical problems, it is not possible to answer this question for the domain $\Omega = [-40, 40]$ with the given methods, but an easy trick is to take a smaller domain size and make a similar analysis. This is done in the next section.

5.1.2 Different domain sizes

In this section, the impact of a varying domain size will be shown and analyzed. The following picture 34 shows the continuation results for four different domain sizes.

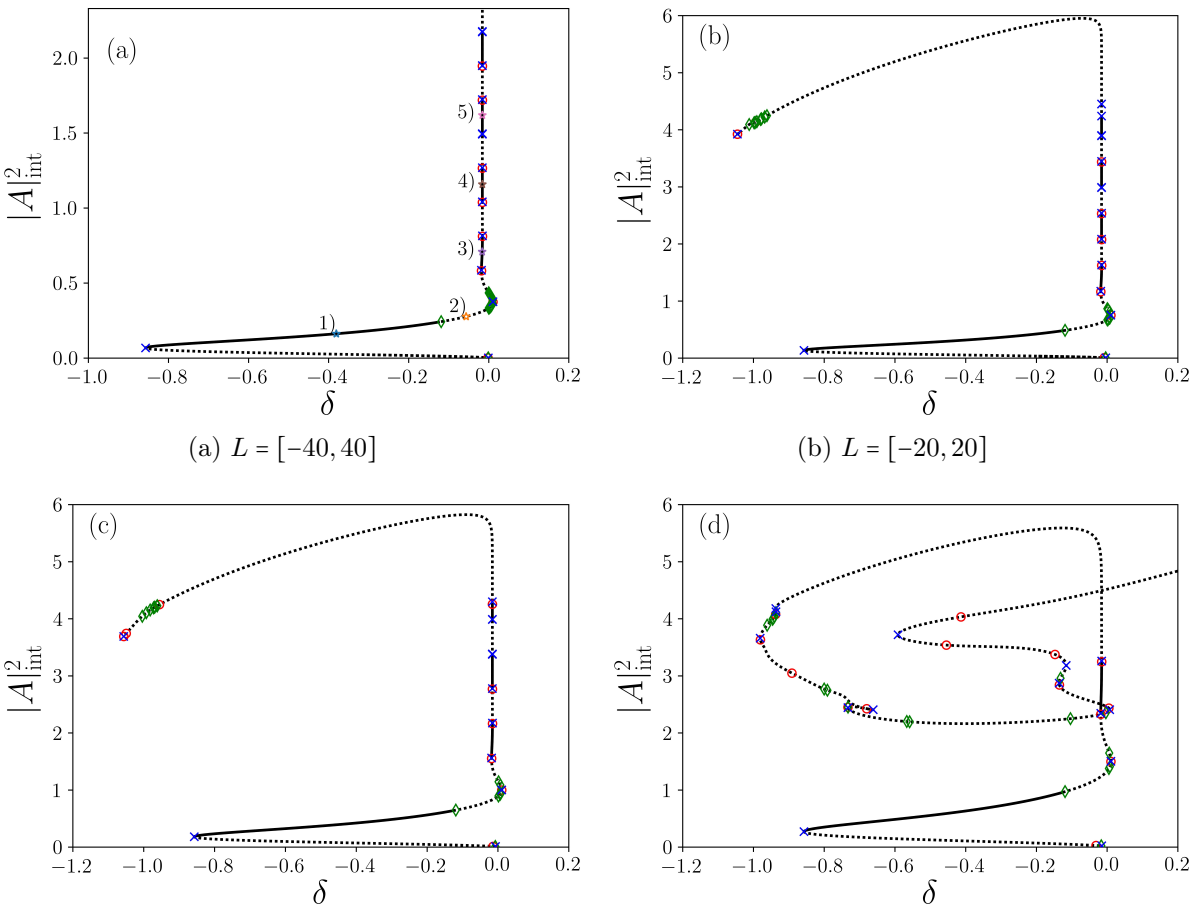

(a) $L = [-40, 40]$ (b) $L = [-20, 20]$

(c) $L = [-15, 15]$ (d) $L = [-10, 10]$

Figure 34: Bifurcation diagrams with a different measure domain size. a) $L = [-40, 40]$ b) $L = [-20, 20]$, c) $L = [-15, 15]$ and d) $L = [-10, 10]$. System parameters: $\beta = 0.08$, $\mu = -0.1$, $\nu = -0.1$, $D = 1$ and $\varepsilon = 0.66$.

Figure 34a shows the same bifurcation diagram as shown in the last section namely for a domain size of $L = [-40, 40]$. Here, the stability changing soliton branch ends abruptly due to numerical errors. To gain more insight within the numerical restrictions the domain size is halved to $L = [-20, 20]$ in the second picture 34b. The beginning of the bifurcation diagram looks similar to the emerging unstable soliton branch that is stabilized by a fold-point and afterwards the rapid growth of the intensity measure with the periodic change of stability can be seen. For this domain length, it is possible to see further development of the soliton branch. After the stability changing area, there is a small regime where the intensity measure grows further until presumably the complete domain is filled. Then the unstable solution structure changes resulting in a decreasing intensity. It then undergoes several bifurcations including pitchfork- and hopf-bifurcations as well as a fold-point, resulting in a lot of unstable eigenvalues. The branch ends in a fold-point (like the starting point), which means that it may be connected to another vastly different solution type that can not be found in this way using continuation, or another behaviour that needs to be examined. A very similar result can be seen in figure 34c where the domain length is reduced to $L = [-15, 15]$. In contrast to that a different behaviour can be seen in figure 34d with $L = [-10, 10]$. Here the previous endpoint of the branch vanishes and the soliton undergoes a lot of different bifurcations which sometimes act destabilizing and sometimes stabilizing but overall the soliton stays in the unstable regime. In the end the soliton branch seems to grow indefinitely for a positive gain $\delta > 0$ (at least until $\delta = 10$).
So all in all figure 34 can be separated into three different types: Firstly for $L = [-40, 40]$ where the diagram is not complete and ends within the stability-changing regime. Secondly, for the two sizes $L = [-20, 20]$ and $[-15, 15]$ the soliton branch ends in a fold-point. Lastly, for $L = [-10, 10]$ there is no connection of the soliton branch and it ends up increasing indefinitely with $\delta > 0$. Even though this distinction follows practically from the results it is not expedient physically. This is clear for $L = [-40, 40]$ where the diagram just ends due to numerical errors, so it does not make sense to distinguish it from the others. But the same can be true for $L = [-10, 10]$ as well: The domain length as a physical parameter is connected to the retarded time t which also describes the laser cavity (see section 3.2 „Complex cubic-quintic Ginzburg-Landau equation“). That means that the domain length is an arbitrarily large number and it does not make sense to minimize it. Doing so might result in an inability to apply the framework of this Ginzburg-Landau equation. So taking a smaller domain length in the numerical analysis, may not give physical results which occur just because of the small domain length and not due to a physical reason. Under this background, the bifurcation diagram 34d might be also an artifact of the numerical simulation due to a too-small domain length. Therefore the simulations for $L = [-20, 20]$ and $[-15, 15]$ would give the most accurate results.
There are a few different ideas to test this thesis. The first idea that comes to mind when discussing different domain lengths is to do continuation using the domain length as the control parameter. At first glance, that seems hard to do because the domain length is not a system parameter in the complex cubic-quintic Ginzburg-Landau equation (equation 20). By redefining the time scale t using for example $t' = \Omega t$ and inserting that into the equation one gets a parameter, namely Ω,

connected to the domain length and a continuation is possible. To do this, the Ginzburg-Landau equation must be numerically implemented differently. Therefore another way might be more efficient to examine. Here the change of the solution profile with the control parameter δ will be analyzed for $L = [-10, 10]$ (and $[-20, 20]$) to see differences and physically classify these.
In figure 35 the bifurcation diagram for $L = [-10, 10]$ is shown. There are a few spots marked on the diagram (figure 35a) with lightly blue stars. The solution profile of these positions is shown in the other subfigures 351 to 9).

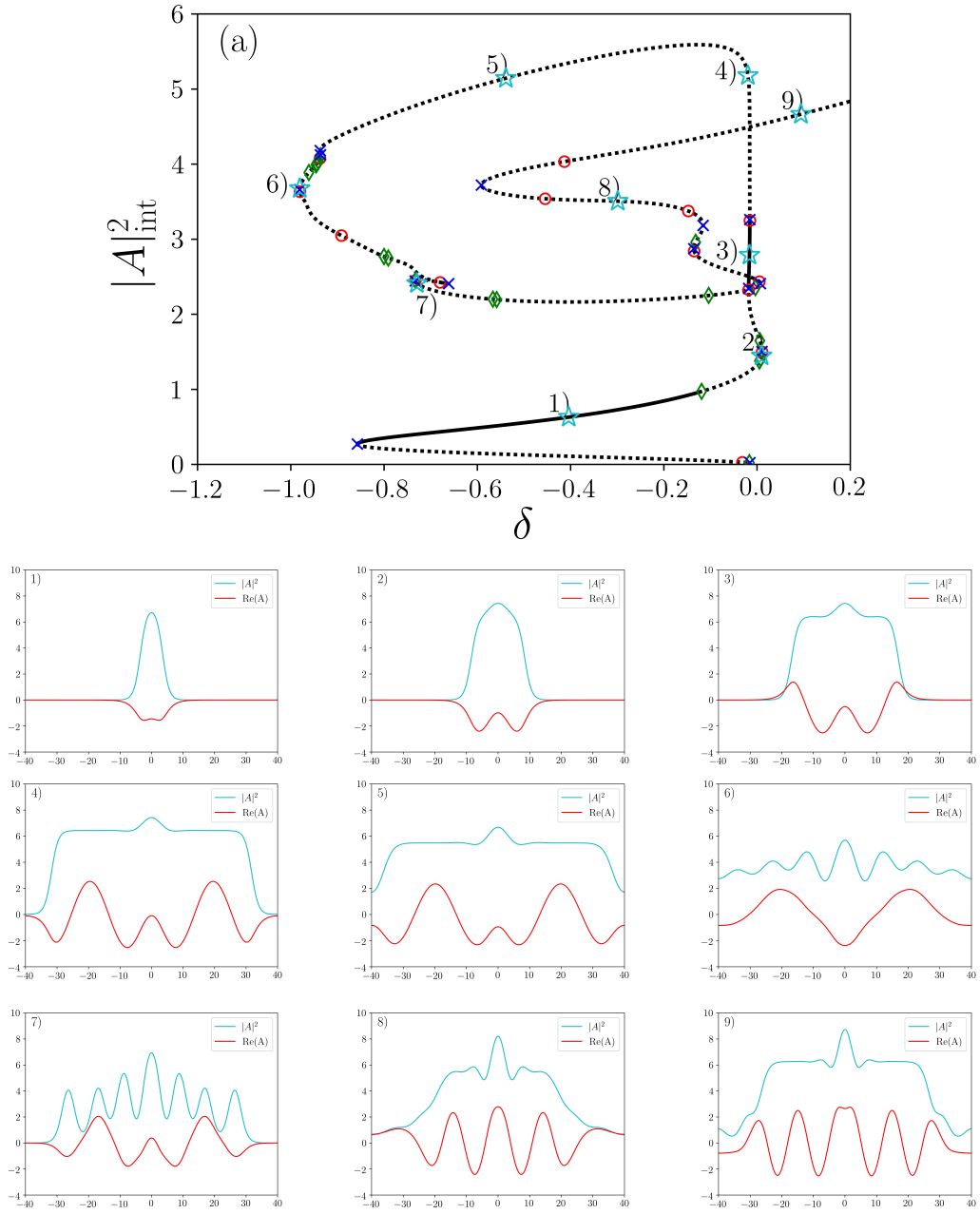

Figure 35: a) Bifurcation diagrams with domain size $L = [-10, 10]$. 1-9) Solution profile marked in figure a) with lightly blue stars. System parameters: $\beta = 0.08$, $\mu = -0.1$, $\nu = -0.1$, $D = 1$ and $\varepsilon = 0.66$.

This figure 35 shows the solution profile at different points in the bifurcation diagram for a domain size of $L = [-10, 10]$. Position 1) and 2) show the expected profile as already seen with $[-40, 40]$ in figure 33, while 3) shows the profile with its width nearly as long as the domain length. Following the soliton branch further along, the profile than gets more compact: the edges rise and the peak drops while the form destabilizes as seen in 4). Close to the endpoint from the higher domain sizes, the profile is close to the form of a sinusoidal function, see 5). Then over the next pictures 7-9) it gets back into the form of a composite soliton with multiple peaks. It seems like it is composed of more than two fronts like the standard composite soliton. All profiles 7-9) as well as the not shown profiles in between suggesting that it exists just as a side effect of the small domain length due to the lack of physical evidence. The existence of such a soliton seems interesting though ignoring the fact that it is unstable and probably exists due to a numerical effect.
The next step is to take a deeper look at a bifurcation diagram in a regime where no numerical side effects take place. It will be done in the next section using a domain length of $L = [-6\pi, 6\pi]$ which is in between both here discussed length of $[-20, 20]$ and $[-15, 15]$.

5.1.3 Connection to previous numerical results

In this section, the bifurcation diagram for a domain length of $L = [-6\pi, 6\pi]$ will be examined and the connection to the pulsating soliton, moving solitons, or other previous numerical results described in section 3 „Localized solutions and soliton resonance in cubic-quintic Ginzburg-Landau equation“ will be shown. The resulting bifurcation diagram is shown in figure 36.

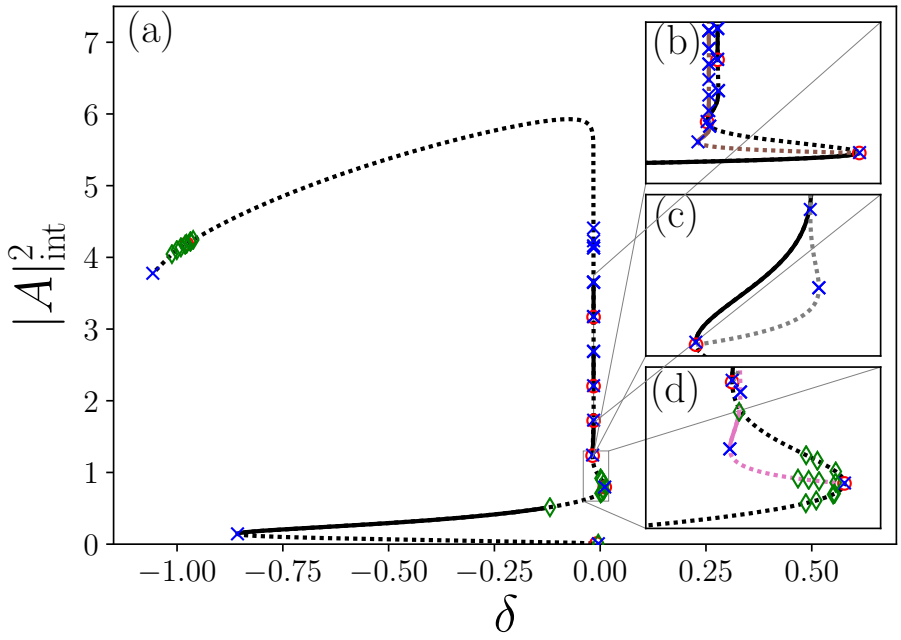

Figure 36: a) Bifurcation diagram. b) Zoom of the snaking regime (not included: the first stable area) with a brown (gray for c) and pink for d)) coloured branch corresponding to the pitchfork bifurcation. c) Zoom of the region of the first stable area of the snaking regime. d) Zoom of the fold at about $\delta = 0$. The hopf bifucation which is on the pink line and not on the black soliton branch. System parameters: $L = [-6\pi, 6\pi]$, $\beta = 0.08$, $\mu = -0.1$, $\nu = -0.1$, $D = 1$ and $\varepsilon = 0.66$.

First of all the rather strange-looking domain length of $[-6\pi, 6\pi]$ was taken to observe possible differences in the bifurcation diagram, for example the sinusoidal shape (as in figure 35,6)). Maybe this shape allows for a better fit of the solution profile into the domain. On first glance this is not the case because the bifurcation diagram, shown in figure 36, is similar to 34b. Just the periodic sequence seems irregular at the snaking regime: At the end of a stable area, there occur two fold points instead of the pitchfork bifurcation followed by a fold point. This changes nothing within the context of the number of unstable eigenvalues and might be a numerical error, because of the still changing curvature afterwards.
In the inset diagrams 36 b-d) the side branches of several pitchfork bifurcation are shown. It looks like there is always just one branch emerging because both branches share the same measure which results in an overlap of both within the diagram. Picture 36d shows a zoom of the pitchfork bifurcation point near $\delta = 0$. Again, there occur a lot of hopf bifurcations due to the global instability of solitons for positive gain $\delta > 0$. This results in a lot of hopf bifurcations on the soliton- and the subcritical pitchfork bifurcation branch. The latter is stabilized by a fold-point, giving a set of stable solutions. It is then as well destabilized by a hopf bifurcation (which only occurs on the pink branch, not on the black one) and undergoes a series of destabilizing and stabilizing fold-points while increasing its intensity measure. A similar behaviour can be seen in the inset diagrams 36b and c). At both pitchfork bifurcation points, a subcritical bifurcation occurs and is afterwards stabilized by one fold-point. This results in periodically occurring stable solutions for the transition from stable to unstable and periodically unstable solutions for the other transition from unstable to stable.
So after understanding the behaviour of the emerging branches from the pitchfork bifurcations, the same can be done, in theory, with the hopf bifurcations. The difference in analysis is the time dependant branches of the hopf bifurcation which complicates the numerical process. To include those solutions into the simulation a second coordinate, namely time z, needs to be added to the continuation process. This not only needs a mean time-intensity measure but also complicates the elliptical numerical problem. Therefore in this work no analysis of the branch structure of the emerging branches of the hopf bifurcation is given. To still get values of the presence of a hopf bifurcation: It is possible to use direct numerics to gain insight into the solution profile if there is a stable branch emerging. In general direct numerics can be used to test the continuation results: A stable solution profile of the continuation can be analyzed via direct numerics and if it then stays stable within that simulation, it supports the stability claim, else there might be an error within the simulation.
Now, to classify all different types of solutions within the bifurcation diagram 36 using the nomenclature of previous results (see section 3 „Localized solutions and soliton resonance in cubic-quintic Ginzburg-Landau equation“) the solution profile must be analyzed. In figure 37 on the next page, the bifurcation diagram and several solution profiles are shown.
The plain pulse is the result of a direct numerical simulation (see picture 31) and is therefore used as a starting point for the numerical continuation. This means that a stable plain pulse exists (see picture 11a) within the resulting bifurcation diagram. Its profile is shown in subfigure 1). The plain pulse is found on the soliton branch emerging from the homogeneous zero state. Its height grows along that branch until it is stabilized at a certain height with a fold-point.

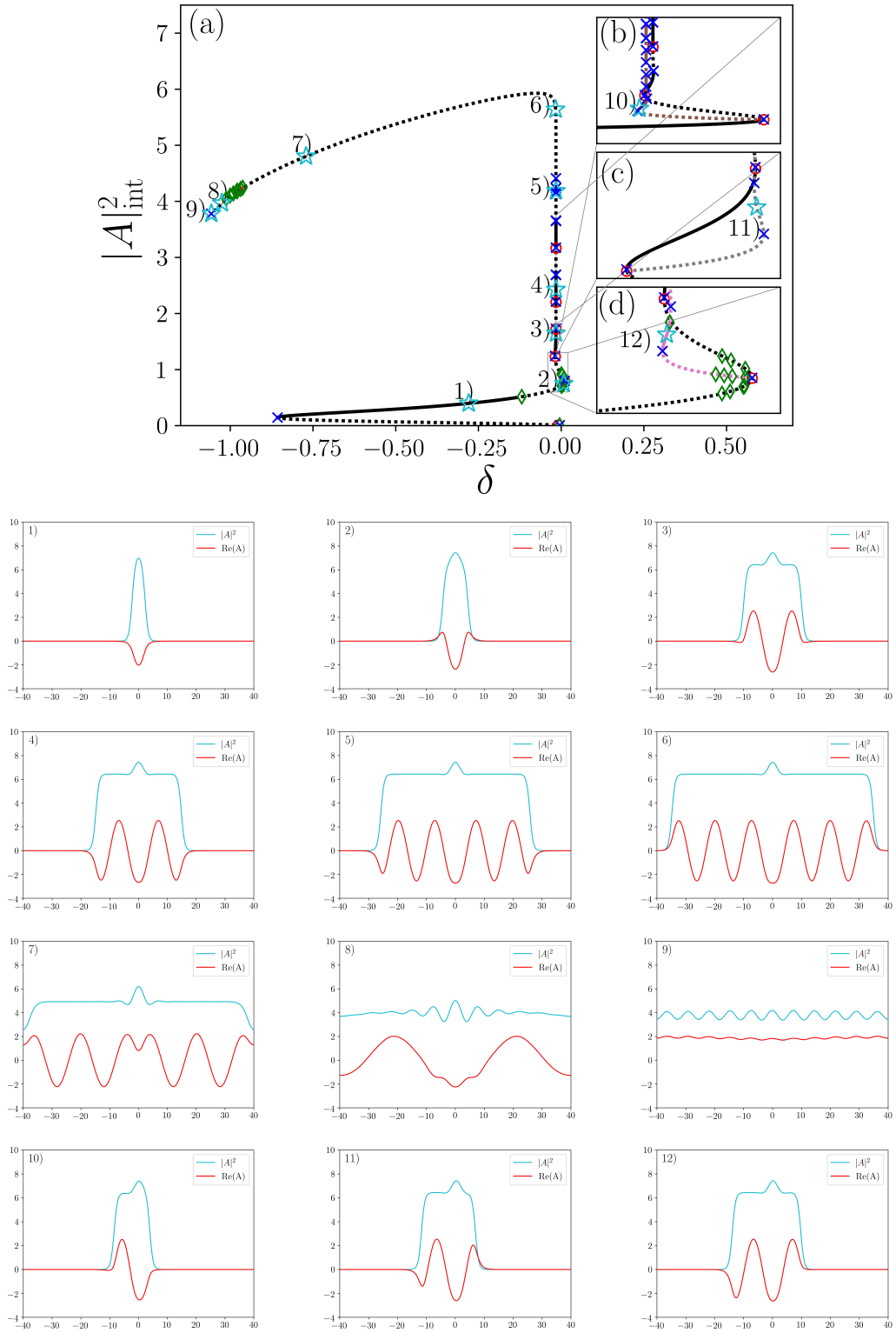

Figure 37: a) Bifurcation diagram with domain size $L = [-6\pi, 6\pi]$. 1-12) Solution profile marked in figure a) with lightly blue stars. System parameters: $\beta = 0.08$, $\mu = -0.1$, $\nu = -0.1$, $D = 1$ and $\varepsilon = 0.66$.

There is also an upper limit to the peak height of the plain soliton, as a hopf bifurcation occurs and the plain pulse solution becomes unstable. But this hopf bifurcation enables the existence of the pulsating soliton solution (see picture 16). Even though the time dependant branches from the hopf bifurcation were not analyzed using continuation, it is still possible to connect them to the pulsating soliton because of the direct numerical analysis. As seen in picture 30, the pulsating solution is stable for $\delta = -0.1$ which is the parameter regime where the hopf bifurcation occurs. By varying different system parameters it can be seen that this bifurcation changes position or vanishes completely and those changes can be seen as well in the direct numerical analysis. One example of this is the change in ε, as it is described in section 5.1.6 „Different parameter changes“. When following the plain pulse branch further along towards the regime of $\delta > 0$ it can be seen that the plain pulse (subfigure 1) slowly becomes a composite pulse (see picture 11b). This can be seen in subfigures 2 and 3). Next up, the composite soliton grows in width, as seen in the solution profiles 3-6), building a straight line within the bifurcation diagram. The growth in width can be seen in the lightly blue drawn absolute value profile, but the red coloured real part gives a better insight into what is happening in this process. The real part of the composite soliton consists of a periodic sequence of maxima and minima. When the pulse is growing in width the number of peaks increases until no more peaks can be built because the maximum width is achieved. During this snaking process, there is multistability of composite solitons with different widths at a given δ. This δ can be called Maxwell-point and the growth of the composite soliton follows along the corresponding Maxwell-line. This nomenclature originates from two colliding objects like two fronts of the composite soliton in this case. The Maxwell point, as well as the Maxwell line, are important to determine because higher energy solitons can be found there.
The next solution types that can be found within this bifurcation diagram are the moving solitons (see 14). They can be found as a part of the inset diagrams 37b-d). Marked with number 12) is a stable moving soliton solution. It is part of the right-moving branch of the pitchfork bifurcation. To make sure that it is indeed a moving solution the resulting profile was put in as an initial condition for a direct numerical simulation. The outcome can be seen in figure 38b.

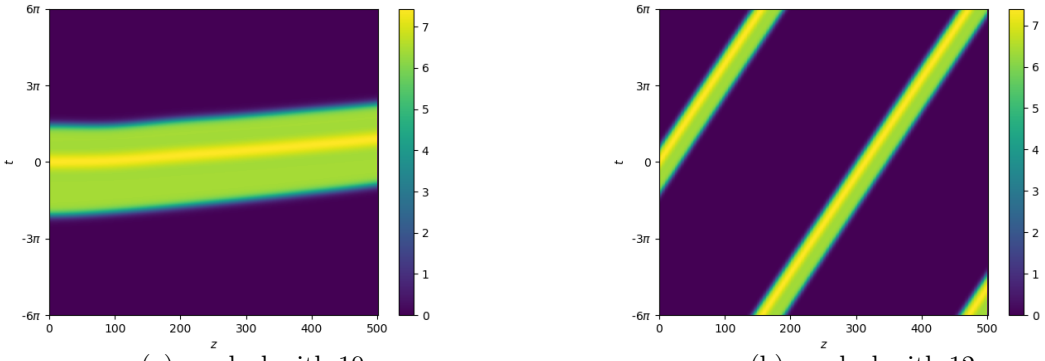

(a) marked with 10 (b) marked with 12

Figure 38: Direct numerics simulation of the solution profile of the marked points in figure 37. a) marked with 12 and b) marked with 10. System parameters: $\beta = 0.08$, $\mu = -0.1$, $\nu = -0.1$, $D = 1$ and $\varepsilon = 0.66$.

Next to it, figure 38a shows the direct numerical result for the second type of moving soliton marked with 10) in figure 37. It can be seen that both are indeed moving solitons. The difference

in velocity comes from the more asymmetric position of the peak. Another aspect is that the branches from all pitchfork bifurcations in the composite soliton regime follow along the Maxwell-line and undergo several bifurcations. They all end somewhere within that line due to numerical dependencies.
The stable regime of moving solutions is cut of by another hopf bifurcation. The emerging time dependant branches might correspond to the creeping solutions of figure 18, because of the added time dependence which is needed for this type of solution. But these snaking solutions were not be found using direct numerics which can be due to numerical errors.
There is a paper by Knobloch and Kao [51] that gives an ansatz to calculate approximately the Maxwell point which is useful because it characterizes the bifurcation diagram and has therefore also predictive usage. They used a different variation of the cubic-quintic Ginzburg-Landau equation

$$\frac{\partial A}{\partial z} = \frac{\partial^2 A}{\partial t^2} + \mu A + \mathrm{i}\left(a_1 |A|^2 \frac{\partial A}{\partial t} + a_s |A|^2 \frac{\partial A^*}{\partial z}\right) + b |A|^2 A - |A|^4 A. \tag{108}$$

and looked into stationary solutions of this equation 108

$$0 = \frac{\partial^2 A}{\partial t^2} + \mu A + \mathrm{i}\left(a_1 |A|^2 \frac{\partial A}{\partial t} + a_s |A|^2 \frac{\partial A^*}{\partial z}\right) + b |A|^2 A - |A|^4 A. \tag{109}$$

and used it as a (real) fourth-order dynamical system, by taking into account the two continuous symmetries, namely translation and phase shift symmetry. Due to Noether's theorem, there are two conserved quantities and they are given by [52]

$$E := (\mu + 2a_2 L) |A|^2 + \left|\frac{\partial A}{\partial t}\right|^2 + \frac{b}{2} |A|^4 - \left(\frac{1}{3} + \frac{a_2(a_1 + a_2)}{6}\right) |A|^6 \tag{110}$$

$$L := \frac{\mathrm{i}}{2}\left(A\frac{\partial A^*}{\partial t} - \frac{\partial A}{\partial t} A^*\right) + \frac{a_1 + a_2}{4} |A|^4 . \tag{111}$$

Using this definition it is possible to define a potential U, to construct a linearized system, and in the end to approximate the Maxwell-point.
In theory, it should be possible to do a similar ansatz that could be applied for the here used version of the Ginzburg-Landau equation if the general solution set is restricted to a subset with translation and phase shift symmetry. The problem is that in this case, it is hard to find those two conserved quantities because in general, they are not conserved for the complex cubic-quintic Ginzburg-Landau equation [53]. Therefore it was too hard to use this approach to gain an approximation for the Maxwell point. Nevertheless, there was another idea that the Maxwell point might be connected to the soliton resonance phenomenon due to the increase in energy on the Maxwell line. This will be discussed in the section 5.2 „Soliton Resonance".
Now the behaviour of the composite soliton within the Maxwell line following the regime of maximum growth in the initially analyzed bifurcation diagram in picture 37 will be examined. As it can be seen in subfigure 7-9), the solution profile shows an analogous behaviour to the one analyzed earlier for $L = [-10, 10]$ until the periodic sinusoidal structure occurred (see picture 35): A deformation of the composite soliton takes place until it ends up in a fold point with a periodic profile with eleven maxima at the end of the branch. In the following section, other possible

connections to the fold point will be examined. One possible connection is the continuous wave solution.

5.1.4 Continuous-wave solution

One possible connection to the fold point at the end of the soliton branch in figure 36 might be the continuous-wave solution or for short cw solution. Continuous-wave solutions can be characterized by their non-space t dependant profile causing a homogeneous intensity profile which still is affected by time z dependant chances to its phase corresponding to its real and imaginary part. Mathematically speaking these are solutions of the following type

$$A(t,z) = A_0 \cdot \mathrm{e}^{-\mathrm{i}\omega z}. \tag{112}$$

The idea behind the possible connection to the end of the soliton branch comes from the snaking regime. At the end of it, the composite soliton nearly fills the whole domain length. Ignoring the maximum in the middle that looks similar to a homogeneous solution so that a transition to that type of solution is imaginable. Nevertheless, a direct transition does not occur possibly due to a different structure or due to the domain length. Therefore the composite soliton deforms and undergoes bifurcations until the branch ends in a fold point.
There are two different solution types for spatial homogeneous solutions. One is the above-mentioned cw solution described by equation 112 and the other is a true homogeneous solution in space and time $A(t,z) = A_0$. The cw solution is a more likely candidate because of the more similar structure to the time and space dependant soliton branch with the remaining phase in the ansatz. Furthermore, the constant zero solution of the complex cubic-quintic Ginzburg-Landau equation should be already connected to the beginning of the soliton branch.
To examine the possible connection, a numerical continuation of the cw branch is done. Therefore the initial solution function from a direct numerical simulation needs to be inserted to start the continuation process. There is an easy way to obtain such a result by calculating an ansatz for the direct numerical approach:
First of all the cw ansatz of equation 112 $A(t,z) = A_0 \cdot \mathrm{e}^{-\mathrm{i}\omega z}$ is inserted into the complex cubic-quintic Ginzburg-Landau equation (equation 21)

$$\frac{\partial A}{\partial z} = \left(\beta + \frac{D}{2}\mathrm{i}\right)\frac{\partial^2 A}{\partial t^2} + \delta A + (\varepsilon + \mathrm{i})\,|A|^2 A + (\mu + \nu\mathrm{i})\,|A|^4 A \tag{113}$$

which gives

$$-\mathrm{i}\omega A_0 \cdot \mathrm{e}^{-\mathrm{i}\omega z} = +\delta A + (\varepsilon + \mathrm{i})A_0^3 \cdot \mathrm{e}^{-\mathrm{i}\omega z} + (\mu + \nu\mathrm{i})A_0^5 \cdot \mathrm{e}^{-\mathrm{i}\omega z}, \tag{114}$$

using the relation $|A|^2 = A_0^2$ and the t derivative vanishes due to the lack of t dependency. Dividing by $\mathrm{e}^{-\mathrm{i}\omega z}$ the equation becomes

$$-\mathrm{i}\omega A_0 = \delta A_0 + (\varepsilon + \mathrm{i})A_0^3 + (\mu + \nu\mathrm{i})A_0^5. \tag{115}$$

Now the equation is split up into a real and imaginary part

$$\begin{aligned} \text{Re)} \qquad & 0 = \delta A_0 + \varepsilon A_0^3 + \mu A_0^5 \\ \text{Im)} \qquad & -\omega = A_0^2 + \nu A_0^4. \end{aligned} \tag{116}$$

Now, to gain an ansatz for the direct numerical simulation, the real part equation can be evaluated further to determine an equation for A_0^2. The simplified real part equation is given by

$$0 = \delta + \varepsilon A_0^2 + \mu A_0^4. \tag{117}$$

therefore an expression for A_0^2 can be calculated directly

$$\Rightarrow \qquad 0 = A_0^4 + \frac{\varepsilon}{\mu} A_0^2 + \frac{\delta}{\mu} \tag{118}$$

$$\Rightarrow \qquad A_0^2 = -\frac{\varepsilon}{2\mu} \pm \sqrt{\frac{\varepsilon^2}{4\mu^2} - \frac{\delta}{\mu}}. \tag{119}$$

A solution of the equation exists if $\frac{\varepsilon^2}{4\mu^2} > \frac{\delta}{\mu}$ due to the square root. Now the starting point of the primary continuation parameter is in general a variable. To not have a problem with the existence of the continuous wave solution, the continuation is started at $\delta = 0$, which simplifies the above equation to

$$\Rightarrow \qquad A_0^2 = -\frac{\varepsilon}{2\mu} \pm \sqrt{\frac{\varepsilon^2}{4\mu^2} - 0} \tag{120}$$

$$\Rightarrow \qquad A_0^2 = -\frac{\varepsilon}{2\mu} \pm \frac{\varepsilon}{2\mu} \tag{121}$$

$$\Rightarrow \qquad A_0^2 = \begin{cases} 0 \\ -\frac{\mu}{\varepsilon} \end{cases} \tag{122}$$

so that the ansatz for the direct numerical approach is given by $A_0^2 = -\frac{\mu}{\varepsilon}$.
To do a continuation for the continuous wave branch the number of additional constraints must be adapted. Normally there are two additional constraints needed for the analysis of localized solutions of the complex cubic-quintic Ginzburg-Landau equation namely phase-shift symmetry and translation symmetry. Those symmetries are represented by the Lagrange parameters of the phase-shift velocity ω and v within the implementation. For more information about those additional constraints see section 4.2.2.3 „Phase shift symmetry and translation invariance“ and for their implementation section 4.2.3.3 „Additional constraints“.
The phase-shift invariance equation 78

$$\Delta A \cdot \frac{\partial A}{\partial t} \stackrel{!}{=} 0.$$

This relation is always true for the cw branch and therefore only the additional constraint for the phase-shift symmetry must be added. Therefore for the continuation the translational invariance parameter $q2$ is erased from the implementation for example in gl1d_qf.m and gl1d_sGjac.m.
The resulting bifurcation diagram for the cw branch with periodic boundary conditions is shown in figure 39.

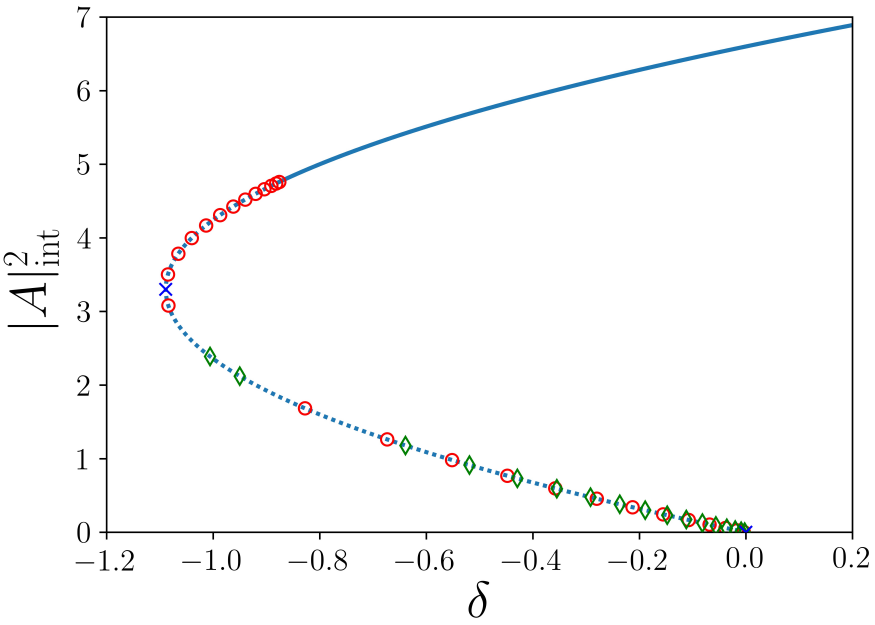

Figure 39: Bifurcation diagram for the continuous wave branch with periodic boundary conditions. System parameters: $L = [-6\pi, 6\pi]$, $\beta = 0.08$, $\mu = -0.1$, $\nu = -0.1$, $D = 1$ and $\varepsilon = 0.66$.

The continuation is started at $\delta = 0$ and done twice once in the direction of positive δ where the branch stays stable and the other time into negative δ direction which gives a more complex behaviour as seen in figure 39. The branch stays stable until it is destabilized by a lot of pitchfork bifurcations. With a fold point, it develops again into the direction towards $\delta = 0$. Then a series of stabilizing hopf bifurcations with destabilizing pitchfork bifurcations occur until just a few eigenvalues are unstable and the branch ends in a fold point. Another important point is that the number of changing stabilizing or destabilizing eigenvalues is twice as high for this simulation as it would be expected for a hopf or pitchfork bifurcation. This is explained by the fact that there might be more bifurcations in between which are restricted by the periodic boundary condition. To verify this claim the same simulation is done with Neumann boundary conditions (vanishing derivatives at the end of the domain). It can be seen in figure 40 on the next page.
In this picture 40 several more bifurcations can be seen in contrast to figure 39, where the emerging branches correspond to non-periodic solutions. Here the number of eigenvalues that change stability fits the expected amount. Therefore the bifurcation diagram with periodic boundary conditions makes sense within this context.
The next step is to understand what kind of solutions can be found on the secondary pitchfork bifurcation branches. This continuation is again done with the two auxiliary conditions connected

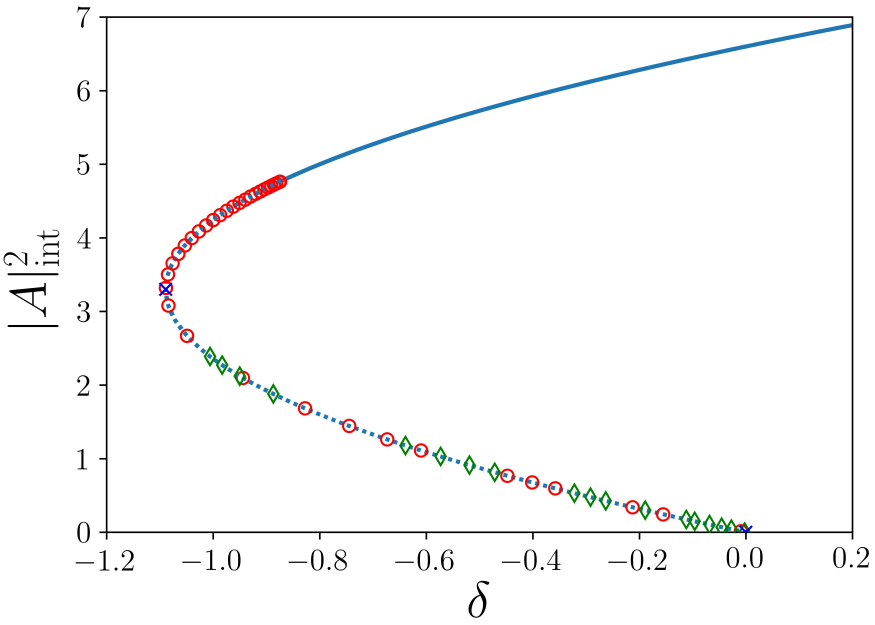

Figure 40: Bifurcation diagram for the continuous wave branch with Neumann boundary conditions. System parameters: $L = [-6\pi, 6\pi]$, $\beta = 0.08$, $\mu = -0.1$, $\nu = -0.1$, $D = 1$ and $\varepsilon = 0.66$.

to the free parameters ω and v. If that continuation is done with only one additional constraint, a lot of bifurcations get falsely detected due to the changing, not fixed free parameter. Therefore to gain a meaningful result the continuation needs to be done with two constraints which makes also sense because of the assumed connection to the soliton branch.

The following figure 41 (on the next page) shows the solution profile at different positions on the cw branch and secondary branches.

The solution profile on the cw branch, see figure 41 profile 1), is by construction a constant solution in space t with a phase that changes with time z. The height of the solution changes along the branch and is stable until a certain threshold under which it changes stability. In the solution profile 2-4), there are periodic sinusoidal solutions with a changing periodicity corresponding to a certain amount of maxima existing within the domain size. This number is connected to the order in which the bifurcations occur. So the seventh bifurcation has seven maxima as shown in figure 1). As a reminder, there are twice as much unstable eigenvalues as the bifurcation point number due to the periodic boundary conditions. The three shown branches all reconnect to another pitchfork bifurcation of the cw branch after the fold point. This is true for most of the other bifurcation points but there are a few exceptions like the first bifurcation which secondary branch has moving solutions and does not seem to reconnect again to the cw branch.

By comparing the end of the soliton branch in figure 37 9) and secondary branch from the eleventh bifurcation point in figure 41 3) they have close to the same solution structure. Therefore those two branches might be connected via a pitchfork bifurcation. This will be examined closer in the next section.

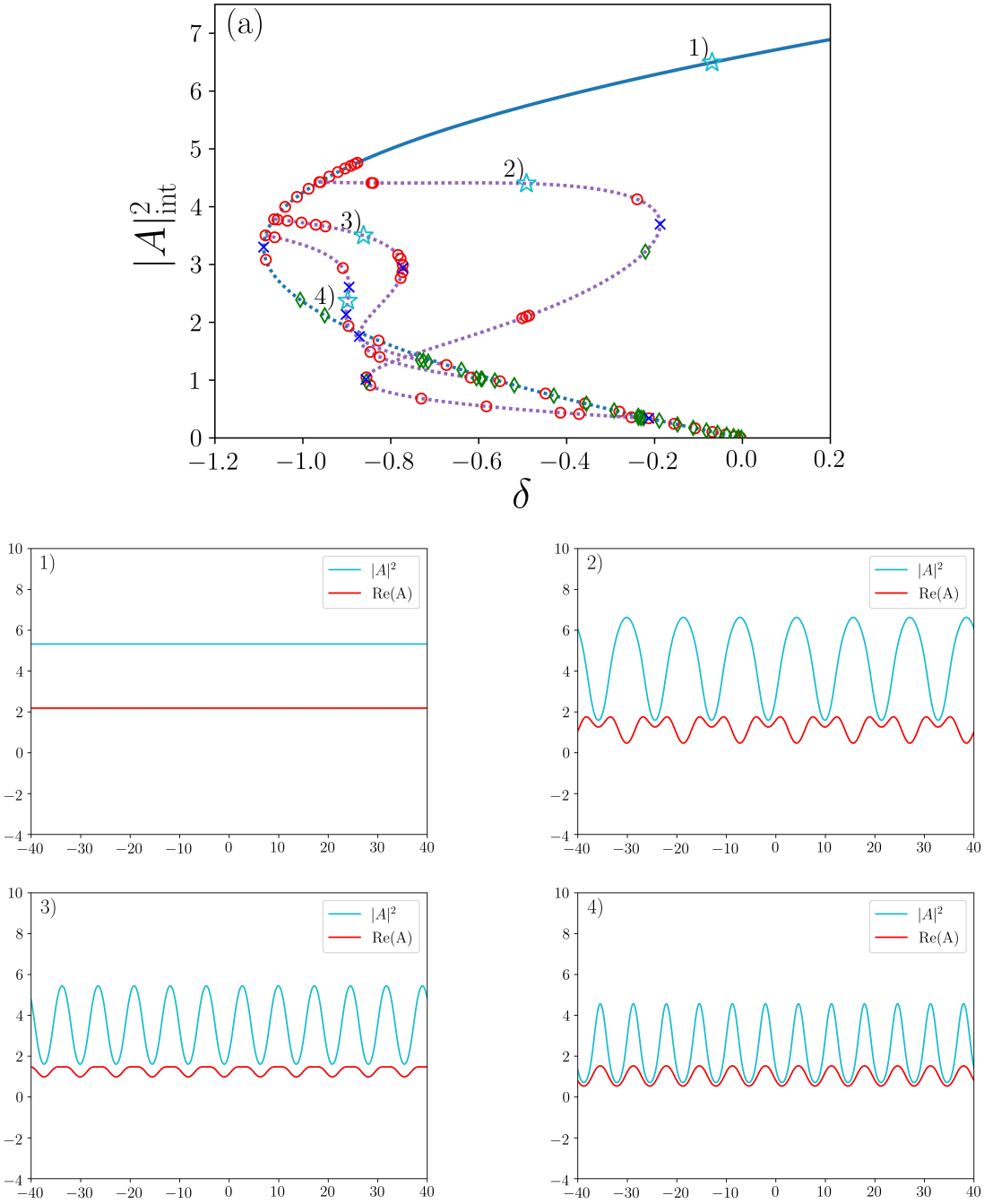

Figure 41: a) Bifurcation diagram for the continuous wave branch and secondary branches with periodic boundary conditions and marked positions. 1-4) Solution profile marked in figure a) with lightly blue stars. System parameters: $L = [-6\pi, 6\pi]$, $\beta = 0.08$, $\mu = -0.1$, $\nu = -0.1$, $D = 1$ and $\varepsilon = 0.66$.

5.1.5 Connection between cw branch and soliton branch

To examine the connection between the cw and the soliton branch both will be shown together in the following figure 42.

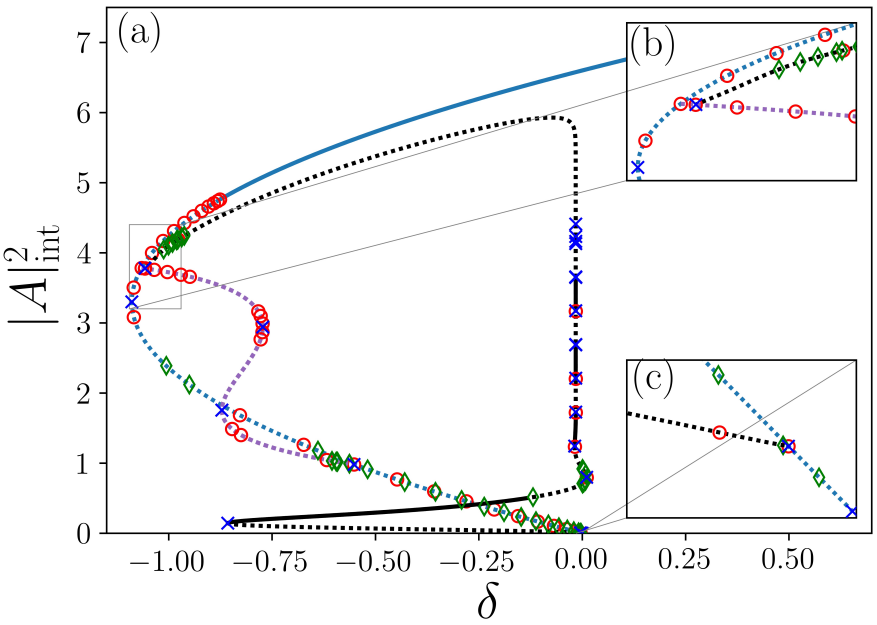

Figure 42: a) Bifurcation diagram for the soliton and the cw branch. In the inset diagrams a zoom of b) the end c) the beginning of the soliton branch is shown. System parameters: $L = [-6\pi, 6\pi]$, $\beta = 0.08$, $\mu = -0.1$, $\nu = -0.1$, $D = 1$ and $\varepsilon = 0.66$.

In figure 42 the soliton branch and the cw with the secondary branch of the eleventh pitchfork bifurcation in the case of periodic boundary conditions. There are also two inset diagrams that show the beginning and the end of the soliton branch. Starting with the end of the branch in subfigure 42b one can see that the fold point of the soliton branch is in fact connected to the pitchfork bifurcation point of the purple secondary cw branch when looking at the shown $|A|^2_{\text{int}}$ measure. To verify this claim a continuation of the branch emerging from the pitchfork bifurcation of the secondary cw branch is done. As the graphic suggests, the emerging branch is indeed the soliton branch. Therefore the end of the soliton branch is connected to a secondary bifurcation of the continuous wave branch.

Another connection between the cw and the soliton branch can be seen in subfigure 42c. Here the fold point of the black soliton branch connects to the last pitchfork bifurcation on the cw branch. It is number 26 counted within the periodic boundary conditions. This connection is again verified using another continuation of the cw branch. The continuous wave branch ends in a fold point at $\delta = 0$ connecting to the constant zero solution.

To sum up, the cw branch is connected to the soliton branch once directly and indirectly over a secondary cw branch. In general, there are a lot of either not shown or not analyzed pitchfork and hopf bifurcations on the soliton, cw, and on the secondary cw branches. Due to the number of bifurcations and their high amount of unstable eigenvalues it is hard to find, select and evaluate those which might show another interesting behaviour change of the solution possibly leading to

new stable solution types. The analysis in this work includes a lot of important structural changes but there might be more.
The next section it is analyzed how and if at all the soliton, cw branch, or its connection changes when varying different system parameters.

5.1.6 Different parameter changes

In this section, the impact of parameter changes on the bifurcation diagram is of interest. There are a lot of possibly interesting changes that can occur like bifurcations vanishing or new ones arising. Especially the impact on the connection between the cw and the soliton branch will be analyzed.

5.1.6.1 Impact of the domain size L

First up is the evaluation of the bifurcation diagram when the domain size is changed. The results are shown in figure 43.

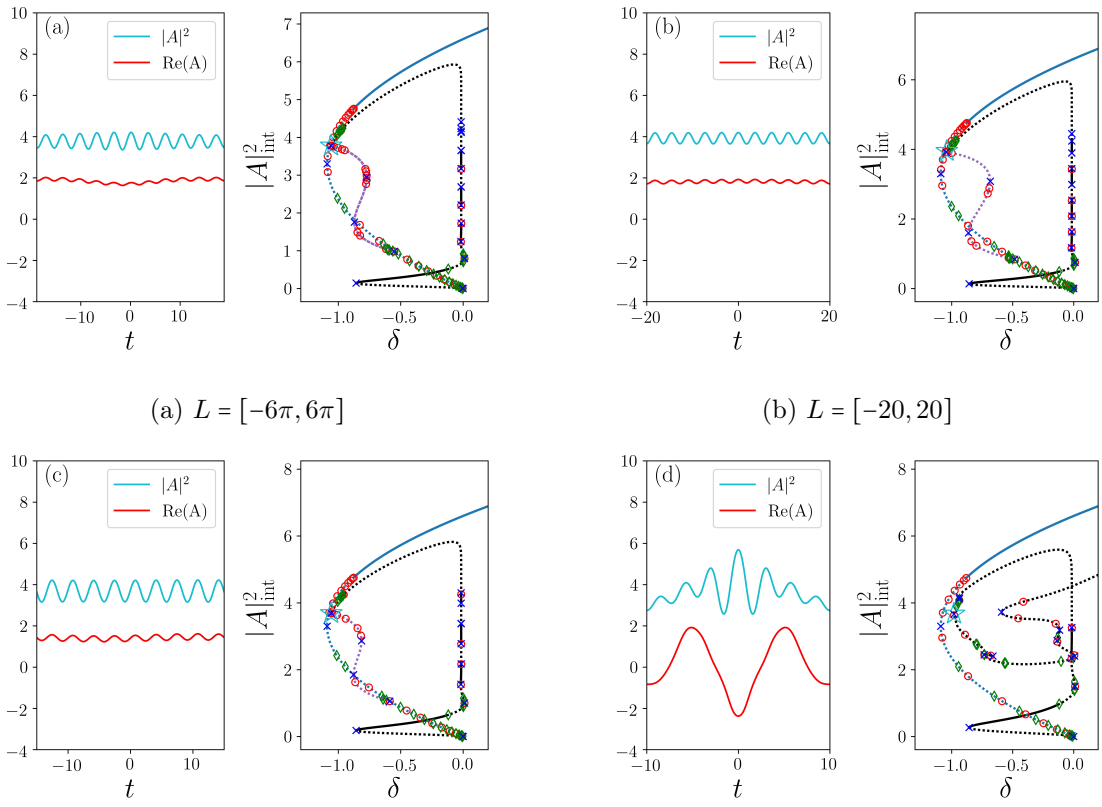

(a) $L = [-6\pi, 6\pi]$ (b) $L = [-20, 20]$

(c) $L = [-15, 15]$ (d) $L = [-10, 10]$

Figure 43: Bifurcation diagram for the continuous wave branch and soliton branch to show their connection for a varying domain size. The solution profile of the last point on the soliton branch which is marked as a light blue star is also shown within the figure. a) $L = [-20, 20]$ b) $L = [-6\pi, 6\pi]$ c) $L = [-15, 15]$ d) $L = [-10, 10]$. System parameters: $\beta = 0.08$, $\mu = -0.1$, $\nu = -0.1$, $D = 1$ and $\varepsilon = 0.66$.

By comparing the subfigures from 43a to 43d it can be seen that the number of maximums at the connection point is correlated to the domain size and the bifurcation point number on the continuous wave branch: For the similar domain length of $L = [-6\pi, 6\pi]$ and $[-20, 20]$ (as shown in figure 43b and 43a) the connection to the cw branch is at the eleventh bifurcation point and here the solution profile shows also a sinus-like solution with eleven peaks. If now the domain size is smaller like for $L = [-15, 15]$ as in figure 43c it can be seen that in both cases the number shrinks to nine.
The last subdiagram 43d shows why there is no connection between both branches for $L = [-10, 10]$, because there are no bifurcation points on the branch before the destabilizing fold point. Therefore there can not be a reconnection of secondary pitchfork bifurcation branch from a bifurcation point before the fold point to one after it, which causes the missing connection between the cw and the soliton branch for this domain size. The connection at the beginning of the soliton branch with the cw branch remains.

5.1.6.2 Impact of the nonlinear gain ε

The next parameter which is changed is the nonlinear gain or loss that depends on the sign of ε. In contrast to the domain size L it is possible, for this parameter, to do continuations using ε as control parameter due to the appearance in the Ginzburg-Landau equation (eq. 20) and the implementation in the numerical model. This enables more methods to analyze the impact of changes in ε onto the bifurcation diagram. One of them is the fold continuation. Here a fold point within an already simulated bifurcation diagram can be selected and changes onto its position can be analyzed by drawing its position in phase space while changing one parameter (here ε). If this is done with all fold points one can get an understanding of the impact of ε changes onto the initial bifurcation diagram. Here the fold continuation will be done using figure 37 as a reference point. The results are shown in figure 44

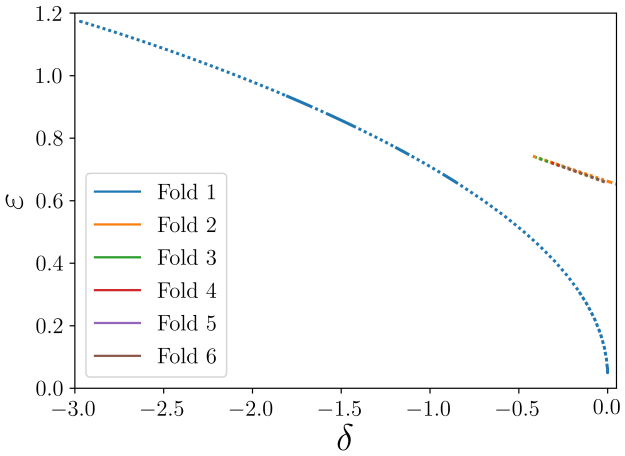

Figure 44: Fold continuation of the different fold points of the bifurcation diagram in figure 37. The number of the fold point is counted from the bottom beginning of the soliton branch. System parameters: $L = [-6\pi, 6\pi]$, $\beta = 0.08$, $\mu = -0.1$, $\nu = -0.1$, $D = 1$ and $\varepsilon = 0.66$.

To understand this fold continuation diagram it is useful to look at the behaviour of the different fold points step by step. The biggest changes can be seen for the first fold point indicated by the red line. For $\varepsilon \to 0$ the fold points position is also shifted to $\delta \to 0$. Therefore the diagram is shifted to the right side when decreasing ε. That works also the other way around: By increasing ε the diagram moves to more negative δ. Here occurs an endpoint because at about $\varepsilon = 1.17$ the line ends which means that the structure of the soliton branch changes so much that the fold point disappears. The same can be seen for the higher numbered fold points. Their branches all lay next to each other in the δ-ε plain because they all occur at roughly the same δ within the Maxwell line. They all seem to disappear at given values and show the same behaviour.
To now understand the structural changes onto the bifurcation diagram a few diagrams are made by varying ε. A basic overview can be seen in the following figure 45.

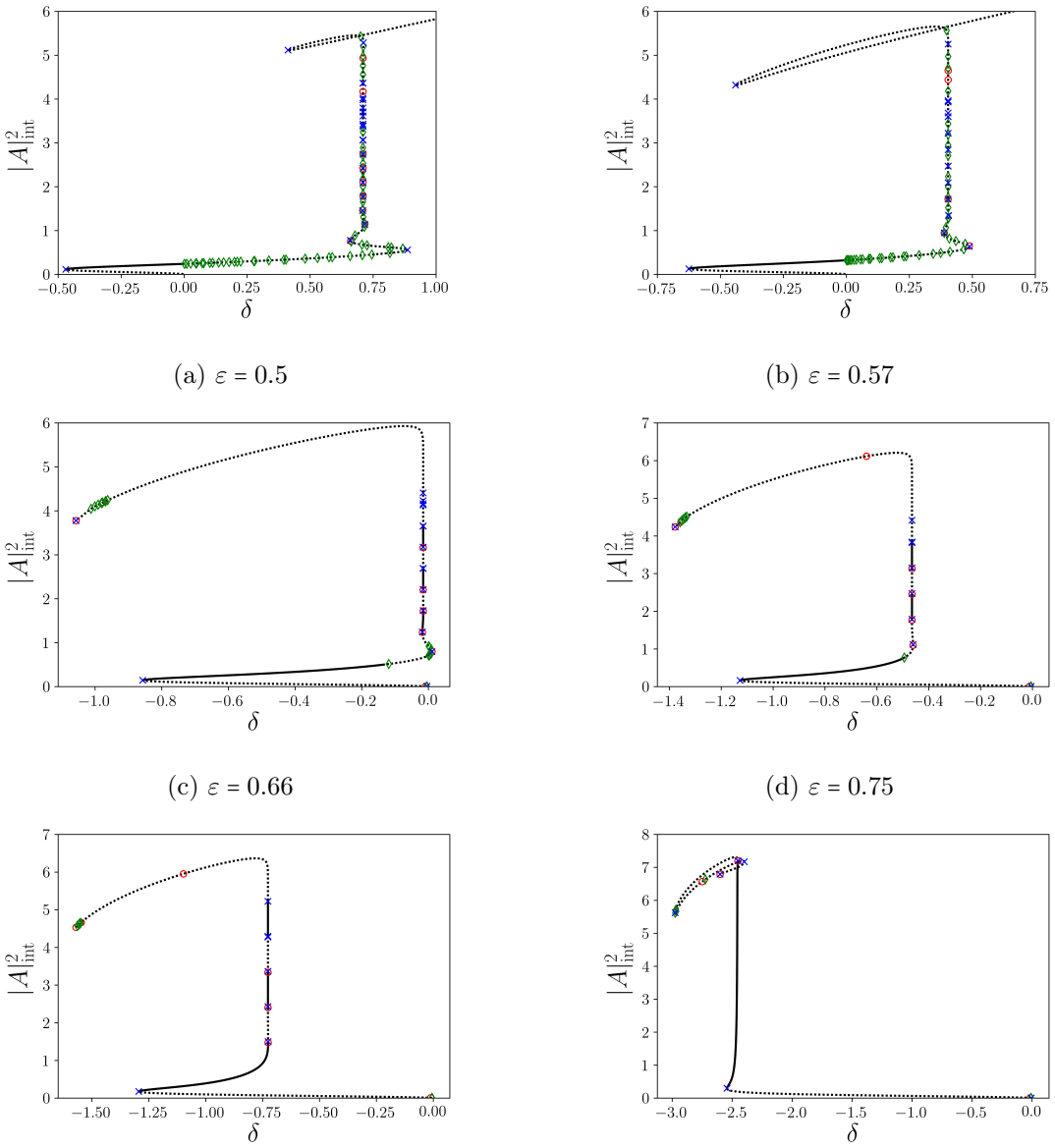

(a) $\varepsilon = 0.5$

(b) $\varepsilon = 0.57$

(c) $\varepsilon = 0.66$

(d) $\varepsilon = 0.75$

(e) $\varepsilon = 0.80$

(f) $\varepsilon = 1.0983$

Figure 45: Bifurcation diagram for different ε values. a) $\varepsilon = 0.5$ b) $\varepsilon = 0.57$ c) $\varepsilon = 0.66$ d) $\varepsilon = 0.75$ e) $\varepsilon = 0.8$ and f) $\varepsilon = 1.0983$. System parameters: $L = [-6\pi, 6\pi]$, $\beta = 0.08$, $\mu = -0.1$, $\nu = -0.1$ and $D = 1$.

For $\varepsilon = 0.5$ and $\varepsilon = 0.57$ (subfigure 45a and 45b) it can be seen that the majority of the soliton branch is in the area of positive δ and is therefore unstable like the composite solitons on the Maxwell line or the moving ones. Only the stable soliton solution is the plain pulse. The subfigure 45c represents the already analyzed diagram 37 with all different kind of stable soliton solutions. This was discussed in-depth and is shown as a reference point to the other diagram with different ε. Figure 45d shows the bifurcation diagram for $\varepsilon = 0.75$. Here the second fold point does not appear and with it the stable moving soliton solution. Also the hopf bifurcation point responsible for the pulsating soliton solution is shifted further along the soliton branch and is nearly collided with the next bifurcation point. The impact of this can be seen in figure 45e this hopf bifurcation vanishes and no pulsating solitons exist in this parameter regime. $\varepsilon = 1.0983$ is near the value of the end of the first fold point branch in the fold continuation (figure 44). It can be seen that the whole Maxwell branch disappeared and only stable plain pulses exist. All in all, it can be seen that changes in ε result in a shift to the side of the soliton branch as predicted with the fold continuation diagram.
Using those bifurcation diagrams it is possible to roughly estimate the region of existence of different types of solitons. To make a good guess a smaller step size is needed which takes a lot of computing time. But it is possible to compare the results to other works where this region was estimated with more detail as in [7]. Their results can be seen in the following figure 46.

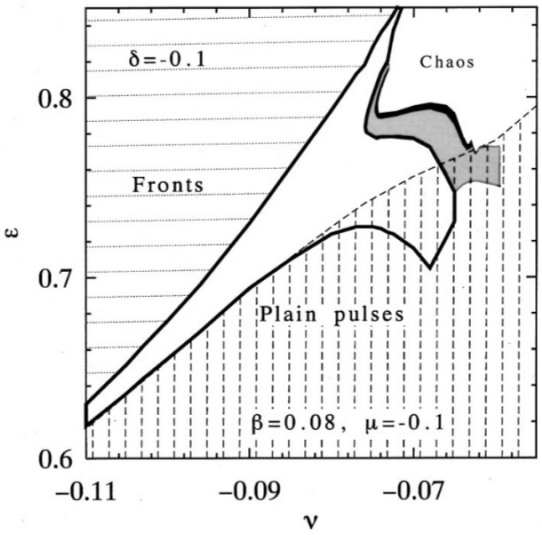

Figure 46: Estimation of the region of existance of different kind of solutions like fronts (horizontally hatched lines) stationary pulses (vertically hatched lines), period doubled (gray area) and chaos (white area) in the ν-ε plain. The enclosed regime is the region of existance for pulsating solitons. System parameters: $\beta = 0.08$, $\mu = -0.1$, $D = 1$ and $\delta = -0.1$. [7]

By taking the cross section at $\nu = -0.1$ this diagram shows the region of existence of different solutions in the here analyzed parameter regime. It can be seen that at $\delta = -0.1$ there should be plain pulses for $\varepsilon = 0.5$ and 0.57 (subfigure 45a and 45b), pulsating solitons exist at about $\varepsilon = 0.66$ (subfigure 45c) and front solutions are stable for higher ε namely $\varepsilon = 0.75$, 0.8 and 1.0983 (figure 45d to 45f). This fits to the results in figure 45. The only differing point is that for the higher

ε values only the statement can be made that there is no stable soliton solution, but it is likely that there can be continuous wave solutions or a front solution.

5.1.6.3 Impact of other parameters

Lastly, the impact of the remaining parameter namely μ, ν, β, and D will be depicted. A basic overview of their impact will be analyzed using fold continuation diagrams. The fold continuation diagrams for the different parameters are shown in the following figure 47.

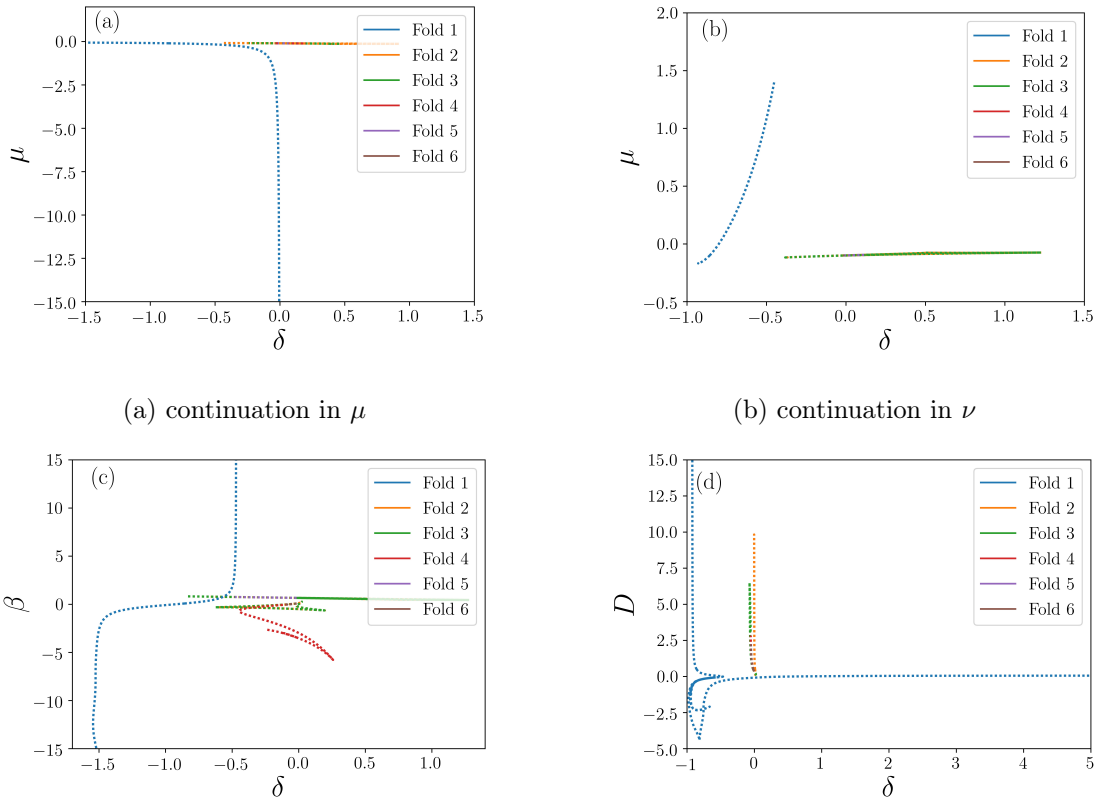

(a) continuation in μ

(b) continuation in ν

(c) continuation in β

(d) continuation in D

Figure 47: Fold continuation of the different fold points of the bifurcation diagram in figure 37. The number of the fold point is counted from the bottom beginning of the soliton branch and the continuation is done in a) μ b) ν c) β d) D. System parameters: $L = [-6\pi, 6\pi]$, $\beta = 0.08$, $\mu = -0.1$, $\nu = -0.1$, $D = 1$ and $\varepsilon = 0.66$.

All fold continuation diagrams have in common that the higher fold points all vanish and some bifurcations collide as it can be seen clearly for figure 47c and the line corresponding to fold points three and four. Even if for some continuations it seems like the higher fold points have a more interesting behaviour change, this vanishing of the snaking regime occurs in all diagrams at some parameter value. The change of the first fold point within all diagrams seems to change more drastically. If the secondary parameter change results in a δ value near $\delta = 0$ a big part of the bifurcation diagram will be in the positive gain regime and therefore all soliton solutions there are unstable. The graph of the first fold point shows in which direction the bifurcation diagram is shifted if the control parameter is changed. This can be symmetric as for β or in a nonlinear

way which can be seen for the other parameters. In general, the stability of branches and the appearance of bifurcations will change with the continuation parameter as well. This was seen for the change in ε in figure 45 and is also expected here. To verify this a more in-depth analysis is needed. This is not done here because a bifurcation diagram analysis of the stable regime of different soliton solutions is not only inaccurate and inefficient but also not the main goal here.

5.2 Soliton Resonance

To analyze the soliton resonance phenomenon the parameter set is changed into the region of normal dispersion $D < 0$. This is done to fit the parameter regime of previous results as depicted in figure 21 and 23. The changed parameters are $L = [-6\pi, 6\pi]$, $\delta = -0.1$, $\varepsilon = 1$, $\beta = 0.08$, $\mu = -0.003$ and $\nu = -0.01$. Note that δ is not the primary continuation parameter and fixed in this case. Now D is taking up that role to be able to see the resonance.
First, the resonance results in figure 21 are reproduced using direct numerics. This is done by starting at a certain D value (here $D = -1$) and then simulating 15 numerical time steps. The results are taken as an initial condition for the next step with a step size of $\Delta D = \pm 0.02$. By repeating these steps a numerical continuation diagram can be made. It is shown in figure 48 below. Note that a different solution measure in comparison to earlier

$$Q = |A|^2_{\text{int}^*} = \int_{t \epsilon L} |A(t)|^2 \ \mathrm{d}t \tag{123}$$

is used here. This is done to make the results comparable to previous works in the context of soliton resonance where they use the energy Q as a measure.

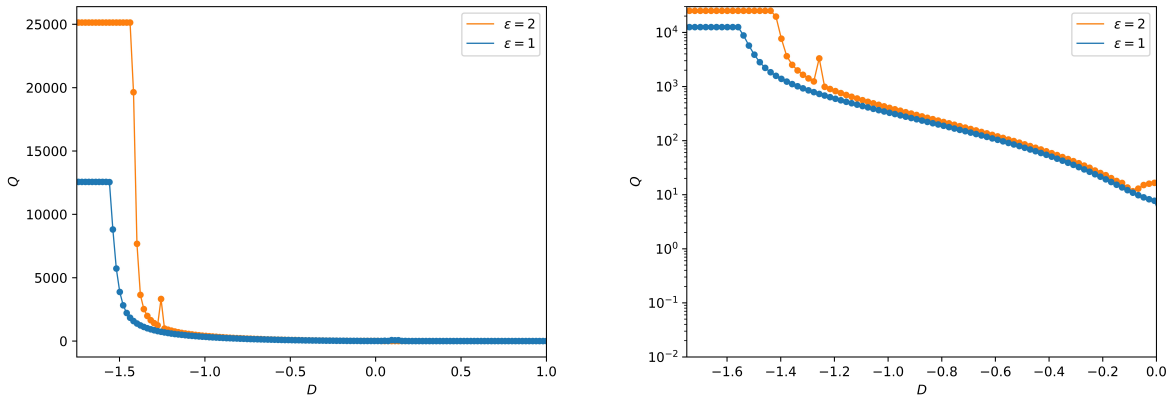

(a) normal scale

(b) logarithmic scale

Figure 48: Direct numeric results that show a soliton resonance for $\varepsilon = 1$ or 2 by varying D in normal scale a) and logarithmic scale b). System parameters: $L = [-6\pi, 6\pi]$, $\delta = -0.1$, $\beta = 0.08$, $\mu = -0.003$ and $\nu = -0.01$.

As it can be seen in figure 48, the energy of the soliton connected to Q rises exponentially like in the previous results in figure 21. This continues when decreasing D until it hits a threshold and the solution stays on the same energy level. Another difference is the not-shown branch for $\varepsilon = 3$.

This is because there was no stable soliton solution at the starting point $D = -1.0$.
While switching to positive D there is also a small maximum, this is due to the insufficient evaluation duration of 15 dimensionless timesteps. If the numerical process is evaluated further the solution drops exactly to a constant zero solution for $D = 0$. This phenomenon probably occurs because the soliton branch becomes unstable there and more timesteps are needed to find the stable solution.
To understand where those differences come from the solution profile is shown in figure 49 for a few positions within the diagram.

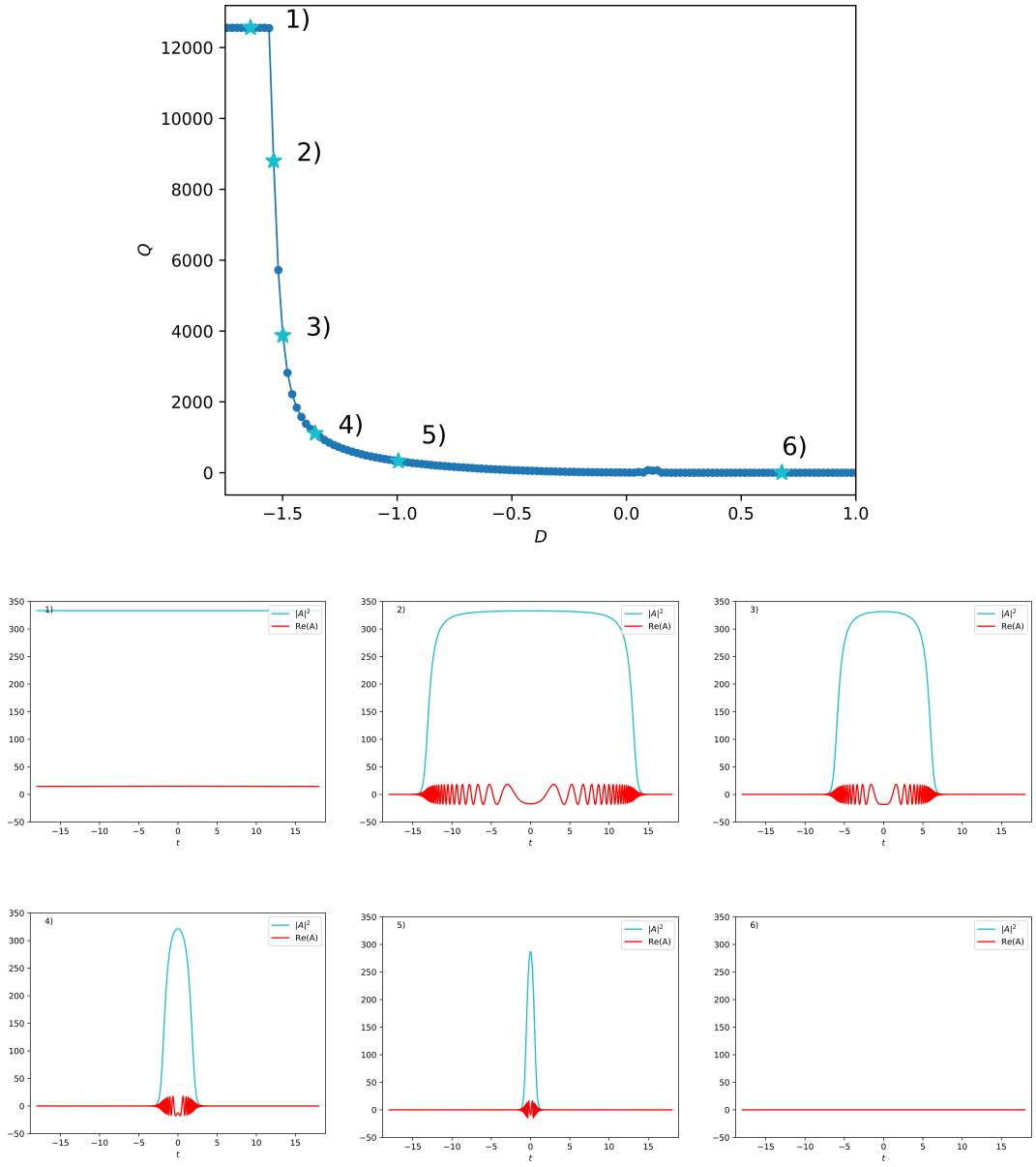

Figure 49: a) Soliton resonance diagram with marked positions. Their profile is shown in 1-6). System parameters: $L = [-6\pi, 6\pi]$, $\delta = -0.1$, $\varepsilon = 1$, $\beta = 0.08$, $\mu = -0.003$ and $\nu = -0.01$.

The plain pulse in subfigure 5) grows in width and height when decreasing D until it reaches the

resonance area (see subfigure 4). At that point, the plain soliton just increases in width which can be seen in subfigure 2 and 3. Afterwards, it changes its shape to a homogeneous one and stays on the same energy level (subfigure 1). That profile structure does not change anymore by decreasing D. For positive D only a constant zero solution exists (subfigure 6).
By looking at the direct numeric results there seems to be a bifurcation occurring that switches from the soliton branch to the constant zero solution and one where the soliton branch switches to the cw branch. Also, that growth in width while increasing in energy might again be connected to a snaking process. To test those claims the next step is to use continuation to make a bifurcation diagram to recreate the direct numerics results.
Again the stable plain soliton at $D = -1.0$ is the starting point of the numerical analysis. The continuation results are shown in figure 50

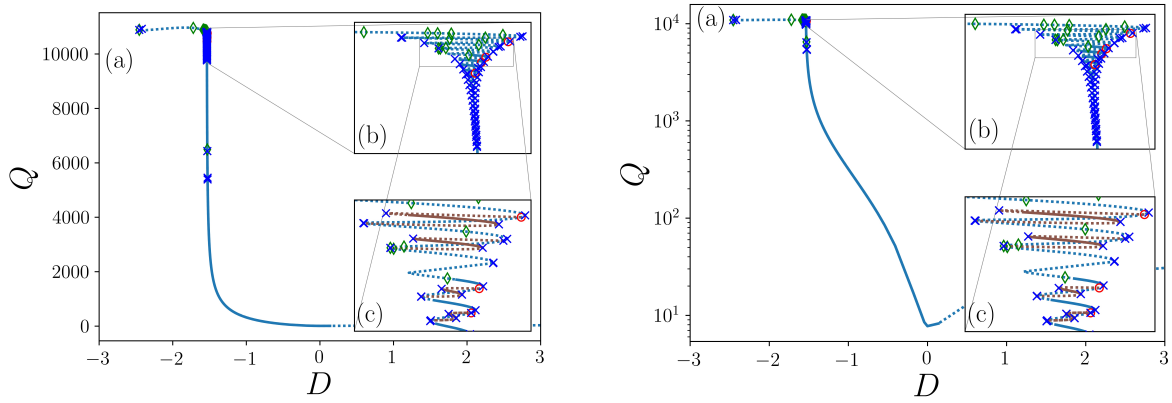

(a) normal scale

(b) logarithmic scale

Figure 50: Bifucation diagram within the regime of soliton resonance with normal scale a) and logarithmic scale b). The inset diagrams show the snaking regime. System parameters: $L = [-6\pi, 6\pi]$, $\delta = -0.1$, $\varepsilon = 1$, $\beta = 0.08$, $\mu = -0.003$ and $\nu = -0.01$.

In figure 50 the resulting bifurcation diagram is shown in normal and logarithmic scale. The logarithmic scale is important for the comparison with the other results and the normal scale allows for an easier view of the bifurcation behaviour of the high energy solitons. This simulation is numerically tedious due to the high increase in energy therefore a lot of steps are simulated with a high steps size and a low amount of calculated eigenvalues which results in not detected bifurcations. An example of that is the transition from positive to negative D. There is a stability change present but no bifurcation is detected. The bifurcation probably occurs at $D = 0$, because the point of stability change is shifted further to it the more eigenvalues are calculated. This is also in agreement with the direct numeric results in figure 48 where a transition to the constant zero solution occurs at $D = 0$.
The continuation towards more negative D shows the more interesting resonance phenomenon. The soliton branch starts to rise in energy and undergoes a few fold points they seem to change the stability of the branch only in a very small parameter regime, but after the hopf bifurcation the branch expands while undergoing a lot of fold and pitchfork bifurcation points as it can be seen in subfigure b). Here is also a constant change of stability as in the earlier discussed snaking

regime. The occurring pitchfork bifurcations all reconnect onto the branch at a later fold point (see subfigure c). At a certain height, the branch becomes completely unstable and stops increasing in height until it ends in a few fold points. Therefore it seems that there is another snaking regime that is connected to an energy increase. Maybe it is as well connected to a Maxwell point. Another interesting point is the solution structure of the secondary pitchfork bifurcation branches. Their and a few other profiles can be seen in the following figure 51.

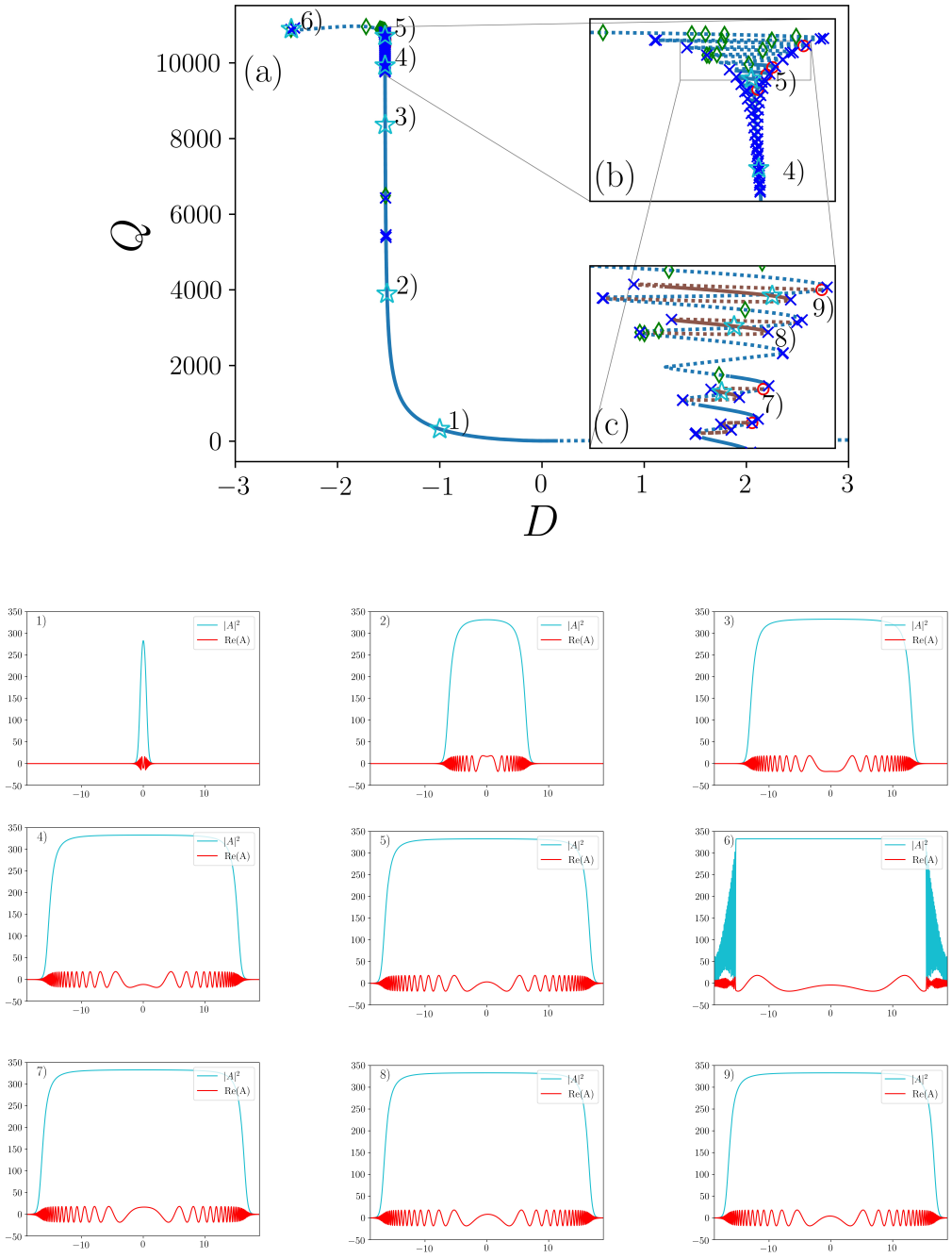

Figure 51: Bifurcation diagram with marked positions. Their profile is shown in 1-9). System parameters: $L = [-6\pi, 6\pi]$, $\delta = -0.1$, $\varepsilon = 1$, $\beta = 0.08$, $\mu = -0.003$ and $\nu = -0.01$.

In general, the profile on the soliton branch follows along the direct numerics results of figure 49. Here the solution also increases in width and height (subfigure 1-2) until it is only increasing in its width (subfigure 3-5). In contrast to the Maxwell point earlier where a composite pulse was increasing in energy, here it seems to be a plain pulse. By looking into the real part of the snaking regime one can see two periodic structures with a high frequency at both ends of the soliton. Their high frequency seems to decrease along the snaking regime so that there is a decreasing phase-shift velocity ω. In the end, some periodic structure is found on the side of the solution in its absolute value. It is an unstable structure with a vast amount of maxima and minima at the edge (see subfigure 6). The profiles in figures 7 to 9 fit the ones directly on the soliton branch and do not show much difference.
Next up is the analysis of the possible transition onto the cw branch. Therefore the cw branch needs to be added to the bifurcation diagram again. Possible values for the amplitude of the cw branch were already calculated in section 5.1.4 „Continuous-wave solution“. Equation 119 yields

$$A_0^2 = -\frac{\varepsilon}{2\mu} \pm \sqrt{\frac{\varepsilon^2}{4\mu^2} - \frac{\delta}{\mu}}.$$

This shows that the continuous wave solution is independent of the parameter D and the amplitude can be caluclated using this equation by inserting the other parameters. The independence has two main implication for the analysis. Firstly it is not useful to do a continuation of the cw branch because it will just „jump“around the real solution due to numerical errors and no additional information will be gained. But secondly it also means that the cw branch can be drawn into the bifurcation diagram as a constant line by calculating its measure because of the independence of D. This is done in figure 52 for both ε

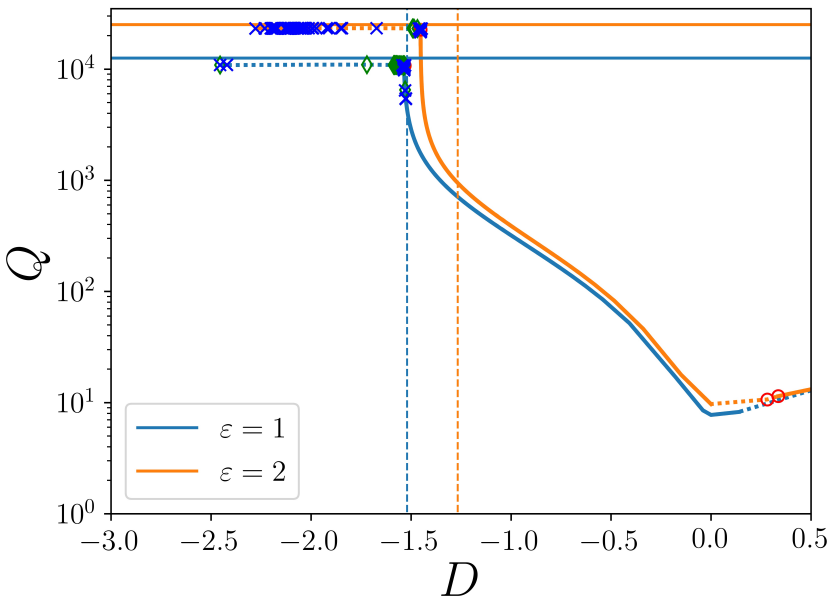

Figure 52: Bifucation diagram within the regime of soliton resonance with cw solution added for $\varepsilon = 1$ and 2 with a logarithmic scale. The dashed line represents the prediction of the value where the resonance occurs by equation 26. System parameters: $L = [-6\pi, 6\pi]$, $\delta = -0.1$, $\beta = 0.08$, $\mu = -0.003$ and $\nu = -0.01$.

It can be seen that the cw branch fits perfectly on top of the soliton branch for both ε. This explains the transition onto the cw branch in the direct numerics results. The results for $\varepsilon = 2$ are in shape and form similar to the one for $\varepsilon = 1$. It is just shifted in position which fits with the numerical results in 48 and with the previous results in figure 21.
By comparing the results with those of the approximation by the method of moments in figure 23 one can see that the left-hand side is an artifact of that approximation but the exponential increase and the position seems to fit better. The slight increase for positive D in the diagram can not be seen within the here described results. Only the direct numerics results in figure 48 show also a slight increase, but this is due to an insufficient number of timesteps for the given D value. In general, there should not be a stable soliton solution for $D > 0$ and that might be as well an artifact of the approximation. But there is another benefit of this method because it allowed them to make an approximation of the value at which the resonance occurs (equation 26)

$$D \approx \left(\frac{3.8\nu}{\mu} - \frac{6.333}{\varepsilon}\right)\beta.$$

This value is marked with a dashed line in figure 52. This line just fits for $\varepsilon = 1$ but especially for $\varepsilon = 2$, it seems to just hit the general region of the resonance. The same can be seen for the results of Akhmediev etc in figure 21 and 24b. Therefore the equation fits for $\varepsilon = 1$ but in general it makes an approximation for the general region where the resonance is occurring.
The next step is to analyze whether it is possible to increase the energy of a soliton infinitely. The cw branch is capping the soliton branch in energy so if the width of the domain is increased, the soliton branch occurs at higher energy. Therefore maximum energy of the soliton should be connected to the domain length and for an infinite domain, there could be infinite energy solitons. It is hard to widen the domain in length due to numerical problems in the continuation as discussed earlier in section 5.1.2 „Different domain sizes“. Therefore the same analysis is done with decreasing domain length to understand the connection between domain length and maximum soliton energy. The results of the continuation can be seen in the following continuation diagram (see figure 53 on the next page).
In figure 53 it can be seen that the height of the cw branch and therefore the maximum energy of a stable soliton indeed scales with the domain length. The energy of a solution is connected to the area under the absolute value curve. So for a solution constant in the absolute value like the cw solution the domain length directly influences the area under the curve. This effect occurs as well for the soliton branch which can be seen in figure 53. Therefore in principle if the connection between both branches remains and the wide soliton stays stable for even higher domain lengths it is reasonable to assume that the soliton energy is uncapped.
The next topic is the non-existing stable soliton branch for $\varepsilon = 3$. To better understand that behaviour, a continuation from the stable $\varepsilon = 2$ branch in ε direction is done. The result is shown in figure 54 which can be seen on the next page.
It can be seen that a destabilizing bifurcation occurs at about $\varepsilon = 2,9$. This explains why there was no stable branch for $\varepsilon = 3$ neither in the continuation nor in the direct numerical analysis. The reason why this might still agree to the other results in figure 21 and 23 can be the domain

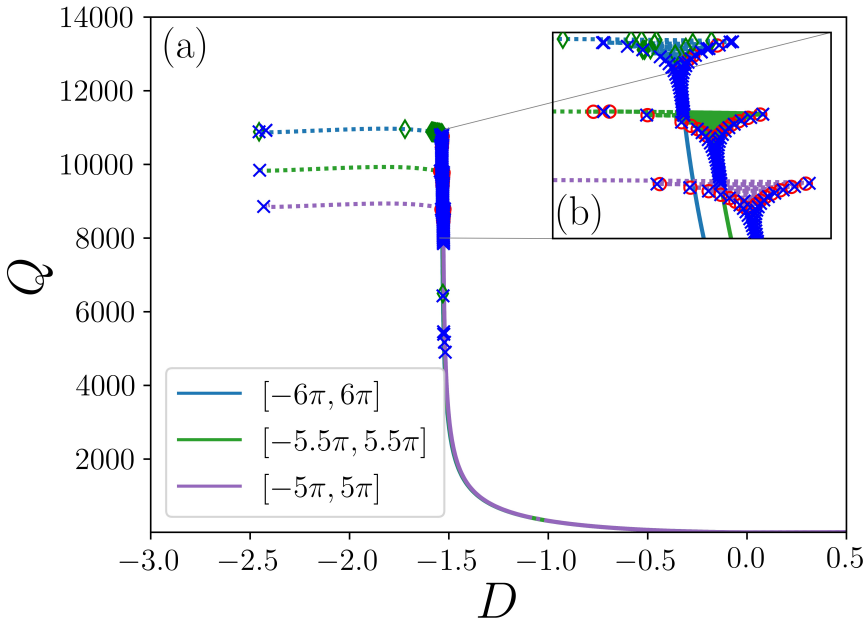

Figure 53: Bifucation diagram within the regime of soliton resonance for three different domain sizes $L = [-6\pi, 6\pi]$, $[-5.5\pi, 5.5\pi]$ and $[5\pi, 5\pi]$. System parameters: $\delta = -0.1$, $\varepsilon = 1$, $\beta = 0.08$, $\mu = -0.003$ and $\nu = -0.01$.

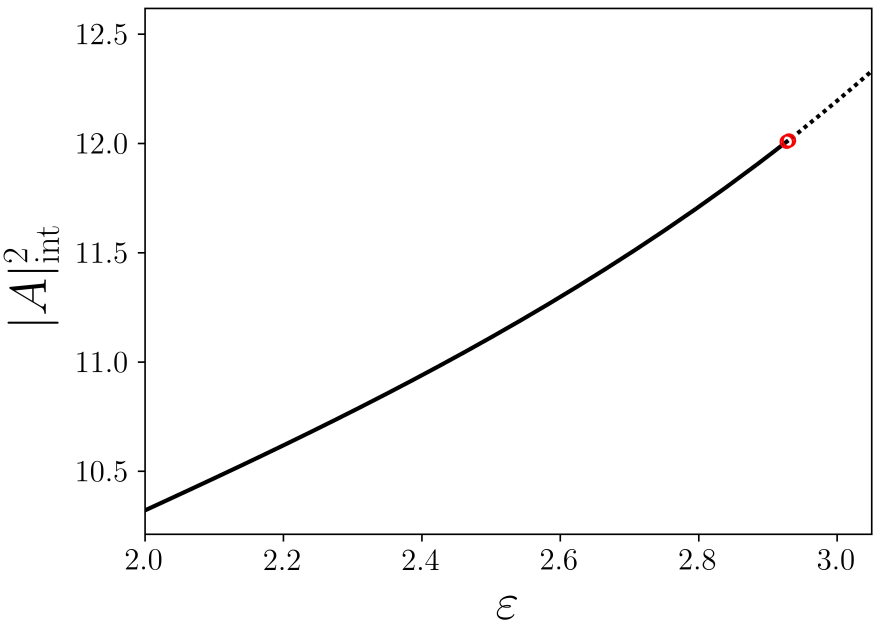

Figure 54: Continuation with ε as primary continuation parameter. System parameters: $D = -1.0$, $\delta = -0.1$,$\beta = 0.08$, $\mu = -0.003$ and $\nu = -0.01$.

length. A change in domain length might shift this bifurcation to the side and allow for stability of the $\varepsilon = 3$ branch.
In the last section, the parameter regime is shifted back to the anomalous dispersion regime to analyze possible changes in that part of the parameter space. First, the same parameter set as in [18] will be used to see the bifurcation structure in that case, and afterwards the parameter regime of the pulsating soliton earlier in this work will be used to refer to those results in the end. Both results are shown in the next figure 55 in different subfigures due to similar results.

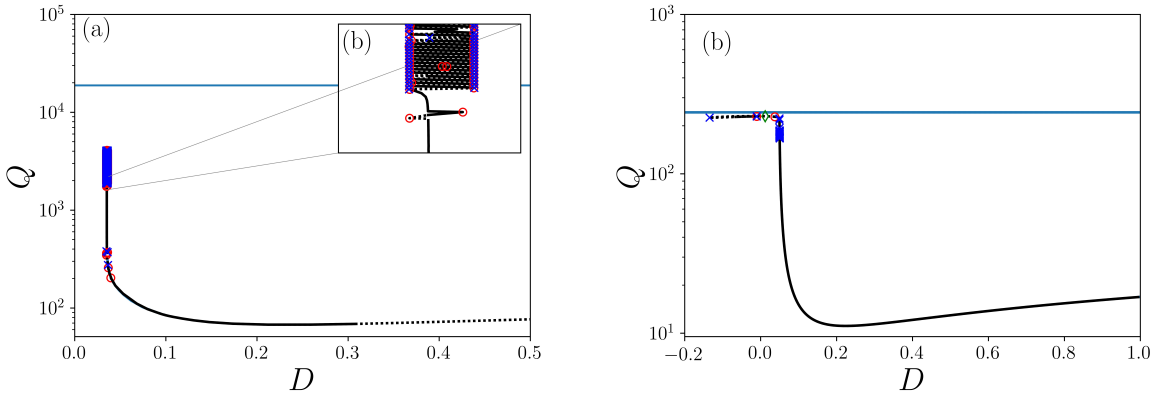

(a) parameters: $\delta = -0.1$, $\beta = 0.08$, $\mu = -0.002$, $\nu = -0.001$ and $\varepsilon = 1$

(b) parameters: $\delta = -0.1$, $\beta = 0.08$, $\mu = -0.1$, $\nu = -0.1$ and $\varepsilon = 0.66$

Figure 55: Bifurcation diagram of the soliton resonance in the anomalous dispersion regime. a) System parameters: $\delta = -0.1$, $\beta = 0.08$, $\mu = -0.002$, $\nu = -0.001$ and $\varepsilon = 1$. b) System parameters: $\delta = -0.1$, $\beta = 0.08$, $\mu = -0.1$, $\nu = -0.1$ and $\varepsilon = 0.66$.

In figure 55a the bifurcation diagram of 24b was replicated using numerical continuation. Here the results are as well as before strongly depending on the number of eigenvalues used so that the right destabilizing boundary at about 0.3 is not accurate. The general height of the stable soliton regime seems to fit the results of figure 24b with the baseline being on the same energy level at under 100. Though the maximum energy value of a soliton is slightly higher in this bifurcation diagram which is maybe due to numerical problems in the direct numerics because the solution just jumps to the cw branch as in 48 or might be due to an insufficient number of eigenvalues used in the continuation. Nevertheless, the branch ends in a vast amount of stability changing pitchfork bifurcation and fold point as it can be seen in the zoomed-in subfigure b). The branch is not calculated to the end due to numerical problems. The last regime with partially even stable solutions seems inaccurate due to a constant stability change without bifurcations. Because the stability can not be verified by direct numerics this is probably a numerical error. An explanation for this error might be that the in this case unstable eigenvalue is at some evaluation steps within the 500 analyzed eigenvalues and in others not. This might cause a constant stability change without bifurcation. The whole soliton branch is at much lower values than the continuous wave branch is calculated to be. A connection is still expected due to the simulation stopping because

of numerical dependencies.
The figure 55b shows a more familiar behaviour, like in figure 52 in the normal dispersion regime only that it occurs at lower energies.
To sum up, the soliton resonance occurs in both the normal and the anomalous dispersion regime even if the maximum energy of the anomalous one is not as high as in the normal regime.

6 Conclusion and outlook

In this work, the dynamics of localized states in the complex quintic-cubic Ginzburg-Landau equation were analyzed using numerical methods namely the arclength continuation method implemented in pde2path and a direct numerical analysis using a Fourier approach and the Runge-Kutta method. The goal was to create bifurcation diagrams to further investigate the connection of various localized solutions like the composite and the moving soliton and the energy increase within the soliton resonance. The purpose of this section is to provide a final summary of what has been achieved while highlighting the most important points and giving an outlook on further aspects.

The starting point of the analysis was to find a parameter regime with a stationary and stable solution to start the continuation process. The time evolution of a stationary solution can be seen in figure 31. Because the exploding solitons were already analyzed in [12], a parameter space corresponding to pulsating solitons namely $D = 1.0$, $\beta = 0.08$, $\mu = -0.1$, $\nu = -0.1$ and $\varepsilon = 0.66$ with δ as primary continuation parameter as in [7] was used. To draw a bifurcation diagram a solution measure must be chosen. The initial idea was to take the maximum intensity $|A|^2_{\text{max}}$ (see equation 106) of the soliton as the measure but due to shrinking spirals as in figure 32, it was hard to display all the information at once without zooming in multiple times. Therefore the total intensity divided by the domain length $|A|^2_{\text{int}}$ (see equation 107) was used in the following bifurcation diagrams. With this measure, it was possible to highlight different aspects like the Maxwell line or the hopf instabilities in the positive δ regime even though the division by the domain length was obstructive in the soliton resonance case mostly because of the different measure of other results for example as [16] or [18]. Thus it was omitted in that context and the energy Q was used as a measure. It is in principle possible to adjust the measure to Q in the first case as well, but the logarithmic scale makes it more unintuitive to understand.

Next up, an appropriate domain size for the numerical analysis was chosen. In general, the quality of a numerical simulation, in this case, depends on the step size, the number of calculated eigenvalues, the tolerance of excepting a solution, and the quality of the initial function. One recurring problem is that the output Matrix can be singular to working precision due to small structures for example within the snaking area which can limit the numerical analysis. This can be seen for the simulation with a domain length of $L = [-20, 20]$ in figure 33. Here the numerical simulation ends without finding the end of the branch. To circumvent that problem a smaller domain length was needed, but not too small because then it might impact the physical behaviour of the soliton which can be seen in figure 34d and 43d. A continuation with the domain length as the primary continuation parameter might give further insight into that topic. In the end, a domain length of $[-6\pi, 6\pi]$ was used for the rest of the analysis. The π periodicity seems to have no impact on the soliton branch which can be seen by comparing figure 34b and 36.

With the outside factors set it was finally possible to draw a bifurcation diagram of the full soliton branch. This can be seen in figure 37 where the black soliton branch and three secondary pitchfork bifurcation branches are depicted in zooms. Several positions are marked with light blue stars within the diagram to show the solution profile at that point. With those profiles, it is possible to

connect parts of the soliton branch to different localized solution types. Using this the plain pulse, the composite pulse, pulsating solitons, and moving solitons were found within the diagram. The creeping soliton solution was theorised to be emerging from the hopf bifurcation on the moving pulse branch. To verify their stability the solution were exported and put in as the initial solution for the direct numerical method. Besides the stability, this also shows possible time behaviour of the solutions as for the moving soliton in figure 38. Taking a look at the results of the numerical derivation of the eigenfunctions and eigenvalues were done rudimentary but a more in-depth analysis might give further insight. The pulsating soliton branch was not numerically simulated due to the time dependant nature of the hopf bifurcation. This would result in significantly longer and more complicated continuations but to get the full bifurcations diagram it is needed for completion. In the bifurcations diagram a snaking process where the composite pulse growths in energy due to an increasing width can be seen. Here, the real part of the solution consists of a periodic sequence of maxima and minima the number of which is increasing until no more peaks can be built because the maximum width, namely the domain length, is achieved. The δ value where the snaking process occurs is called Maxwell-point and the growth of the composite soliton follows along the Maxwell-line. A few ideas of the calculation of the Maxwell-point were discussed but the idea depicted in a paper by Knobloch and Kao [51] seems to be the best approach. For this approximation, two conserved symmetries for localized solutions need to be calculated for the complex cubic-quintic Ginzburg-Landau equation. This seems hard to do because of the more general terms within the equation but should be possible due to Noether's theorem. An in-depth calculation of the Maxwell point is useful because it corresponds to higher energy soliton solutions as it can be seen in the bifurcation diagram 37. It can also be connected to the soliton resonance as discussed in the so-called section.

The next point was the possible connection of the soliton branch to other branches at both ending points. It was expected that the soliton branch emerges from the homogeneous zero with a subcritical pitchfork bifurcation, but especially the ending connection of the fold point was of interest. To find the other branch a transition to the constant absolute value solution was theorized due to the increase of the soliton width until it was nearly as wide as the domain length. An ansatz for a continuous wave solution (equation 112) was used to calculate the cw branch in theory and gain an ansatz for the initial solution function which is given by $A_0^2 = -\frac{\mu}{\varepsilon}$. The resulting bifurcation diagram was shown with periodic (figure 39) and with Neumann boundary conditions (figure 40) due to a changing number of occurring bifurcation points. The branch stays stable until it is destabilized by a lot of pitchfork bifurcations. Their secondary branches are reconnecting onto the cw branch after a fold point. After that fold point, a series of stabilizing hopf bifurcations with destabilizing pitchfork bifurcations occur until just one eigenvalue is unstable and the branch ends in a fold point, where it possibly reconnects to the homogeneous zero solution branch. The secondary pitchfork bifurcation branches have a periodic sinusoidal solution profile with a changing periodicity corresponding to a certain amount of maxima existing within the domain size. This number is connected to the order in which the bifurcations occur and looks a lot like the solution profile at the ending fold point of the soliton branch. To gain a deeper

understanding of the cw branch and its bifurcations a continuation of the secondary branches within the Neumann boundary conditions or the hopf bifurcations can be useful. This might show more connections or similarities to the soliton branch or a completely new stable branch.
To finally determine the connection between the cw and the soliton branch both are shown together in a bifurcation diagram (see figure 42). There a zoom into both ends of the soliton branch is shown and for both points, a connection can be seen: The starting fold point of the soliton branch equals a pitchfork bifurcation point of the cw branch. For the ending point, it is a pitchfork bifurcation on the secondary cw branch with eleven maxima. This connection is verified in both cases by calculating the branch emerging from the pitchfork bifurcation. If they are indeed connected than the branch should be the soliton branch which was the case.
Those two connections seem to be rather random, especially the eleventh bifurcation branch. This opens several questions like why the connection appears at that branch and not any other one, how the connection changes with other parameters, and if the beginning connection stays the same under those parameter changes. Those questions were tried to be answered by numerically calculating bifurcation diagrams for different parameter changes. First of all, the domain size was changed and the results were shown in figure 43. It was seen that the number of maxima at the ending connection point is correlated to the domain size and the bifurcation point number on the continuous wave branch: For $L = [-6\pi, 6\pi]$ and $[-20, 20]$ the connection occurred at the eleventh bifurcation point and for $L = [-15, 15]$ it was the ninth. A few more domain sizes were analyzed and all seem to be odd numbers, which seems to be a coincidence of the analyzed domain sizes, but the same occurred while changing ε. Using this small sample it was not possible to predict the connecting cw branch, but it might correlate to the length of the snaking regime. To understand that connection a more in-depth analysis is needed. Nevertheless, diagram 43d shows why there is no connection between both branches for $L = [-10, 10]$, because there are no bifurcation points on the branch before the destabilizing fold point which means that no reconnection between the two pitchfork bifurcation points occurs. Therefore there can not be a connection between the cw and the soliton branch in that way. This raises the question of why this is the case and how exactly it depends on the domain size. Here again, a continuation in the domain size or a fold continuation of the ending fold point of the soliton branch with the domain size as the continuation parameter might be a good tool for further analysis.
The impact of the other parameter changes was analyzed using fold continuation diagrams. For ε the results are shown in figure 44). It can be seen that the diagram is shifted to the right side when decreasing ε and the other way around. Here occurs an endpoint because at about $\varepsilon = 1.17$ the line ends which means that the structure of the soliton branch changes so much that the fold point disappears. The same can be seen for the higher numbered fold points because they vanish, some by colliding with other ones, at roughly the same ε value. What this means for the bifurcation diagram, is depicted in figure 45. The branch is completely unstable for positive δ and higher values of ε the pulsating soliton hopf bifurcation disappears, the same happens for the snaking bifurcations and in the end as well for the fold point corresponding to stable plain pulses. It would be useful to see the transitions in a more detailed way, so more steps in between are needed to get

a full picture. Then those bifurcation diagrams can be used to estimate the region of existence of different types of solitons like they did in [7] for example (figure 46. The rest of the parameter changes were shown in figure 47. All fold continuation diagrams have in common that the higher fold points all vanish and some bifurcations collide as it can be seen clearly for 47c and the line corresponding to fold points three and four. To see changes in the stability of branches and the appearance of bifurcations a more in-depth analysis is needed. In general, the fold continuation is inaccurate due to the low tolerance of 10^{-6} and it often occurs that the continuation jumps between two branches, especially for higher fold points. A lot of branches within the bifurcation diagrams could be followed along further if an even lower tolerance is excepted. This changing of parameters might have the most potential for further analysis because a lot of variations and different analysis techniques can be used.

Lastly, the soliton resonance phenomenon was analyzed. It started by recreating the soliton resonance results with direct numerics. There (see figure 48 and 49) it can be seen that a resonance and high energies about 10000 dimensionless units occur. The simulation ends in a constant solution, the continuous wave branch. Only the branch of $\varepsilon = 3$ is not shown within both diagrams, because there was no stable plain pulse. A continuation in ε (see figure 54) shows a bifurcation at about $\varepsilon = 2.9$ which explains the instability. This can still agree with the other results in figure 21 and 23 because a different domain length was used. The results of the continuation are shown in figure 50. At first glance it can be seen that the results are inaccurate, because of existing stability changes without a detection of a bifurcation, this is likely due to a too low number of calculated eigenvalues even if a relatively high amount of 500 and more was already used. This is true for all following bifurcation diagrams and is one point to improve upon. In general, the profile on the soliton branch follows along the direct numerics results but at the end of the branch, the branch undergoes again some kind of snaking only that here the plain pulse increases in width. The cw branch can not be evaluated by continuation because of the lack of D dependence (see equation 119), therefore it is calculated and added by hand. The same is done for the estimate of the resonance equation 26 by [16]. In figure 52 it can be seen that the cw branch seems to be a threshold to the soliton energy and that the prediction of the resonance is good for $\varepsilon = 1$ and deviating a lot more for $\varepsilon = 2$. In the anomalous dispersion regime the resonance was capped at a lower energy (see figure 55). Finally, the domain size was changed to see the dependence of the maximum energy of a stable soliton on it and if it is possible to increase the soliton energy indefinitely by increasing the domain size. A connection between the maximum energy and the domain size was shown (figure 53), but the infinite increase was not shown nor ruled out. Further analysis with a higher domain size is needed to answer that question. Other interesting points are the change of the branch with Neumann boundary conditions instead of periodic ones and the connection between soliton and continuous wave branch in the regime of soliton resonance.

References

[1] E. V. Vanin, A. I. Korytin, A. M. Sergeev, D. Anderson, M. Lisak, and L. Vázquez. Dissipative optical solitons. *Phys. Rev. A*, 49:2806–2811, Apr 1994.

[2] Eric Picholle, Carlos Montes, Claude Leycuras, Olivier Legrand, and Jean Botineau. Observation of dissipative superluminous solitons in a brillouin fiber ring laser. *Phys. Rev. Lett.*, 66:1454–1457, Mar 1991.

[3] B.S. Kerner and V.V. Osipov. *Autosolitons: A New Approach to Problems of Self-Organization and Turbulence*. Fundamental Theories of Physics. Springer Netherlands, 1994.

[4] N. Akhmediev and A. Ankiewicz. *Dissipative Solitons: From Optics to Biology and Medicine*. Lecture Notes in Physics. Springer Berlin Heidelberg, 2008.

[5] Philippe Grelu and Nail Akhmediev. Dissipative solitons for mode-locked lasers. *Nature Photonics*, 6(2):84–92, 2012.

[6] Shihua Chen. Theory of dissipative solitons in complex ginzburg-landau systems. *Physical review. E, Statistical, nonlinear, and soft matter physics*, 2008 Aug.

[7] N. Akhmediev, J. M. Soto-Crespo, and G. Town. Pulsating solitons, chaotic solitons, period doubling, and pulse coexistence in mode-locked lasers: Complex ginzburg-landau equation approach. *Phys. Rev. E*, 63:056602, Apr 2001.

[8] V. V. Afanasjev, N. Akhmediev, and J. M. Soto-Crespo. Three forms of localized solutions of the quintic complex ginzburg-landau equation. *Phys. Rev. E*, 53:1931–1939, Feb 1996.

[9] Wonkeun Chang, Adrian Ankiewicz, Nail Akhmediev, and J. M. Soto-Crespo. Creeping solitons in dissipative systems and their bifurcations. *Phys. Rev. E*, 76:016607, Jul 2007.

[10] J.M. Soto-Crespo and Nail Akhmediev. Exploding soliton and front solutions of the complex cubic–quintic ginzburg–landau equation. *Mathematics and Computers in Simulation*, 69(5):526–536, 2005. Nonlinear Waves: Computation and Theory IV.

[11] Nail Akhmediev and J. M. Soto-Crespo. Strongly asymmetric soliton explosions. *Phys. Rev. E*, 70:036613, Sep 2004.

[12] S. V. Gurevich, C. Schelte, and J. Javaloyes. Impact of high-order effects on soliton explosions in the complex cubic-quintic ginzburg-landau equation. *Phys. Rev. A*, 99:061803, Jun 2019.

[13] Sofia C. V. Latas and Mário F. S. Ferreira. Soliton explosion control by higher-order effects. *Opt. Lett.*, 35(11):1771–1773, Jun 2010.

[14] Steven T. Cundiff, J. M. Soto-Crespo, and Nail Akhmediev. Experimental evidence for soliton explosions. *Phys. Rev. Lett.*, 88:073903, Feb 2002.

[15] N. Akhmediev, J.M. Soto-Crespo, and Ph. Grelu. Roadmap to ultra-short record high-energy pulses out of laser oscillators. *Physics Letters A*, 372(17):3124–3128, 2008.

[16] W. Chang, A. Ankiewicz, J. M. Soto-Crespo, and N. Akhmediev. Dissipative soliton resonances. *Phys. Rev. A*, 78:023830, Aug 2008.

[17] Edwin Ding, Philippe Grelu, and J. Nathan Kutz. Dissipative soliton resonance in a passively mode-locked fiber laser. *Opt. Lett.*, 36(7):1146–1148, Apr 2011.

[18] W. Chang, J. M. Soto-Crespo, A. Ankiewicz, and N. Akhmediev. Dissipative soliton resonances in the anomalous dispersion regime. *Phys. Rev. A*, 79:033840, Mar 2009.

[19] Hannes Uecker, Daniel Wetzel, and Jens D. M. Rademacher. pde2path - a matlab package for continuation and bifurcation in 2d elliptic systems. *Numerical Mathematics: Theory, Methods and Applications*, 7(1):58–106, 2014.

[20] M. Basler, P.A. Tipler, R. Dohmen, G. Mosca, C. Heinisch, A. Schleitzer, M. Zillgitt, J. Wagner, and C. Kommer. *Physik: für Wissenschaftler und Ingenieure*. Springer Berlin Heidelberg, 2014.

[21] S.H. Strogatz. *Nonlinear Dynamics and Chaos: With Applications to Physics, Biology, Chemistry, and Engineering*. Chapman & Hall book. CRC Press, 2019.

[22] C. Gerthsen and D. Meschede. *Gerthsen Physik*. Springer-Lehrbuch. Springer Berlin Heidelberg, 2010.

[23] Equilibrium (http://www.scholarpedia.org/article/Equilibrium from 29.11.2021 at 5:50 p.m.). *Scholarpedia, the peer-reviewed open-access encyclopedia*.

[24] Hopf bifurcation (https://en.wikipedia.org/wiki/Hopf_bifurcation from 29.11.2021 at 2:14 a.m.). *Wikipedia, The Free Encyclopedia*.

[25] Akhmediev N. and Ankiewicz A. Dissipative solitons in the complex ginzburg-landau and swift-hohenberg equations. *In: Akhmediev N., Ankiewicz A. (eds) Dissipative Solitons. Lecture Notes in Physics, vol 661. Springer, Berlin, Heidelberg. https://doi.org/10.1007/10928028_ 1*.

[26] Eric Picholle, Carlos Montes, Claude Leycuras, Olivier Legrand, and Jean Botineau. Observation of dissipative superluminous solitons in a brillouin fiber ring laser. *Phys. Rev. Lett.*, 66:1454–1457, Mar 1991.

[27] E. V. Vanin, A. I. Korytin, A. M. Sergeev, D. Anderson, M. Lisak, and L. Vázquez. Dissipative optical solitons. *Phys. Rev. A*, 49:2806–2811, Apr 1994.

[28] HA Haus. A theory of fast saturable absorber modelocking. *J. Appl. Phys*, 46(75):3049–3058, 1975.

[29] Hermann A Haus, James G Fujimoto, and Erich P Ippen. Structures for additive pulse mode locking. *JOSA B*, 8(10):2068–2076, 1991.

[30] Wim van Saarloos and P.C. Hohenberg. Fronts, pulses, sources and sinks in generalized complex ginzburg-landau equations. *Physica D: Nonlinear Phenomena*, 56(4):303–367, 1992.

[31] A Komarov, H Leblond, and F Sanchez. Quintic complex ginzburg-landau model for ring fiber lasers. *Physical Review E*, 72(2):025604, 2005.

[32] Edwin Ding and J Nathan Kutz. Operating regimes, split-step modeling, and the haus master mode-locking model. *JOSA B*, 26(12):2290–2300, 2009.

[33] Alexandr Zaviyalov, Rumen Iliew, Oleg Egorov, and Falk Lederer. Lumped versus distributed description of mode-locked fiber lasers. *JOSA B*, 27(11):2313–2321, 2010.

[34] A. Maimistov. Evolution of solitary waves which are approximately solitons of a nonlinear schrödinger equation. *Journal of Experimental and Theoretical Physics - J EXP THEOR PHYS*, 77:727–731, 01 1993.

[35] Euler's method (https://teaching.smp.uq.edu.au/scims/Appl_analysis/Eulers_method.html from 16.11.2021 at 9:58 p.m.). *Applied Mathematical Analysis, University of Queensland.*

[36] K. Atkinson, W. Han, and D.E. Stewart. *Numerical Solution of Ordinary Differential Equations.* Pure and Applied Mathematics: A Wiley Series of Texts, Monographs and Tracts. Wiley, 2011.

[37] J.C. Butcher. A history of runge-kutta methods. *Applied Numerical Mathematics*, 20(3):247–260, 1996.

[38] C. Runge. Über die numerische auflösung von differentialgleichungen. *Math, Ann 46*, pages 167–178, 1895.

[39] J.C. Butcher. *Numerical Methods for Ordinary Differential Equations.* Wiley, 2016.

[40] Runge-Kutta-Verfahren (https://de.wikipedia.org/wiki/Runge-Kutta-Verfahren from 19.11.2021 at 3:19 p.m.). *Wikipedia, The Free Encyclopedia.*

[41] P.G. Ciarlet. *The Finite Element Method for Elliptic Problems.* Classics in Applied Mathematics. Society for Industrial and Applied Mathematics (SIAM, 3600 Market Street, Floor 6, Philadelphia, PA 19104), 2002.

[42] W. Arendt and K. Urban. *Partielle Differenzialgleichungen: Eine Einführung in analytische und numerische Methoden.* Spektrum Akademischer Verlag, 2010.

[43] D. Langemann and C. Reisch. *So einfach ist Mathematik – Partielle Differenzialgleichungen für Anwender.* Springer Berlin Heidelberg, 2018.

[44] E. Giné, D.M. Mason, J.A. Wellner, and J.A. Wellner. *High Dimensional Probability II: 2.* Progress in Probability. Birkhäuser Boston, 2000.

[45] H. Uecker D. Wetzel T. Dohnal, J. Rademacher. *pde2path 2.0: multi-parameter continuation and periodic domains*, volume Proceedings of 8th European Nonlinear Dynamics Conference, ISBN: 978-3-200-03433-4. Horst Ecker, Alois Steindl, Stefan Jakubek, eds, ENOC 2014.

[46] S. Engelnkemper, S. Gurevich, H. Uecker, D. Wetzel, and U. Thiele. Continuation for thin film hydrodynamics and related scalar problems. 2018.

[47] W.J.F. Govaerts. *Numerical Methods for Bifurcations of Dynamical Equilibria.* Other Titles in Applied Mathematics. Society for Industrial and Applied Mathematics, 2000.

[48] E.L. Allgower and K. Georg. *Numerical Continuation Methods: An Introduction.* Springer Series in Computational Mathematics. Springer Berlin Heidelberg, 2011.

[49] Prof. Dr. Uwe Thiele. *Folien zum Vortrag mit dem Thema: Numerical Continuation - A step by step introduction Prelude to Münsteranian Tutorials at https://www.uni-muenster.de/-CeNoS/Lehre/Tutorials/continuation.html.* Universität Münster, November 2018.

[50] A.F. Izmailov and M.V. Solodov. *Newton-Type Methods for Optimization and Variational Problems.* Springer Series in Operations Research and Financial Engineering. Springer International Publishing, 2014.

[51] Hsien-Ching Kao and Edgar Knobloch. Weakly subcritical stationary patterns: Eckhaus instability and homoclinic snaking. *Physical review. E, Statistical, nonlinear, and soft matter physics*, 85:026211, 02 2012.

[52] Arjen Doelman and Wiktor Eckhaus. Periodic and quasi-periodic solutions of degenerate modulation equations. *Physica D: Nonlinear Phenomena*, 53(2):249–266, 1991.

[53] Nail Akhmediev, Adrian Ankiewicz, and José M. Soto-Crespo. Multisoliton solutions of the complex ginzburg-landau equation. *Physical Review Letters*, 79:4047–4051, 1997.